Universitat Autònoma de Barcelona

Calorimetric study of vapour deposited glasses: beyond conventional stability and temperature limits

Cristian Rodríguez Tinoco

Universitat Autònoma
de Barcelona

Calorimetric study of vapour deposited glasses: beyond conventional stability and temperature limits

Doctoral Thesis submitted by
Cristian Rodríguez Tinoco
to apply for the degree of Doctor in Physics

Supervised by
Prof. Javier Rodríguez Viejo
and
Dr. Marta Gonzalez Silveira

Nanomaterials and Microsystems Group
Physics Department
Bellaterra, April 2016

INDEX

1. MOTIVATION AND OBJECTIVES

"What is the nature of the glassy state? Where and why does liquid end and glass begin?"

This was one of the questions brought up in the *Science* special edition on their 125th anniversary[1]. This question goes further from the very concept of glass, as expressed by James Langer in Physics Today[2]: "If glasses demand unconventional physics, then so must an enormous number of other important systems. How can we hope to understand the mechanical and thermodynamic behaviour of biological substances if, after decades of intense investigation, we still can't understand the properties of simple amorphous materials?".

Glass transition and supercooled liquid dynamics are one example of the main unresolved problems in the condensed matter physics community. This fact appears to be striking when one considers the importance and impact of glasses in our daily life. Glasses are present in almost every moment of our lives: TV or smartphones screens, metallic pieces of aeronautical equipment, the windows of our houses, containing and decorative objects all around us, in medicines we take, etc. How can something be so broadly used and mysterious at the same time?

Glass science is a very active field of research. There are many theories trying to explain the origin of the molecular slowdown close to the glass transition or the physical processes behind the transition, but none of them has been completely successful. Recently, the emergence of a new methodology to produce glasses transformed the scenario. The process consists on growing the glass from the vapour phase but at particular deposition conditions. In that manner, glasses with characteristics typical of ambers, aged for millions of years, can be produced in just few minutes. Let me provide two reasons why this finding is so appealing. First, because it permits to study very stable glasses, systems that were not accessible until the moment, offering a new benchmark to test and elaborate new theories. Second, because these glasses present a series of properties that makes them exciting from the perspective of future applications, for instance: high thermal stability, special molecular arrangement and tuneable orientation, higher resistance towards crystallization, better mechanical and magnetic properties or higher resistance to corrosion.

This work aims to extend the research performed on organic molecular glasses by introducing the use of quasi-adiabatic fast-scanning nanocalorimetry, one of the most prominent membrane-based calorimetric techniques, to study vapour deposited thin film glasses. The possibility to tune the properties of the glass by changing the deposition conditions allows us to analyse the different

facets of the glass transition for a broad range of glass stabilities. We present results on the different transformation mechanisms into the supercooled liquid, and how glass stability plays a significant role. By using fast-scanning nanocalorimetry we also explore the dynamics of the glass at temperatures unachieved to the date. This extended range of data allows us to infer a relation between the dynamics of the glass and that of the supercooled liquid. The application of pressure on a specially designed calorimeter has been the key to preliminary extend the study to the influence of pressure on the dynamics of glasses.

Finally, given the importance of molecular organic glasses in the pharmaceutical industry, we focus part of this work on crystallization and water absorption, two main concerns regarding the large scale use of pharmaceuticals in the glassy form. The results presented in this work show that in ultrastable thin film glasses surface crystallization is slowed down and resistance to water absorption in enhanced.

2. THEORETICAL INTRODUCTION

Glasses represent a fundamental part of technology development and are ubiquitous in our daily life. The best-known example of an engineered glass is probably the window glass, constituted mainly from silica. Besides, we find glasses in many industries: decoration, packaging, structural functions, pharmacy, electronics, optics, telecommunications and renewable energies, to name a few. Glasses are crucial in the processing of food[3]. Optical fibres, of increasing importance in the new era of communications, are made of very pure silica glass. Metallic glasses are used in several aeronautical applications[4]. Glasses are also present in the plastic industry, where most engineering plastics are amorphous. The multi-disciplinary nature of glasses is remarkable. The combination of the microscopic disordered structure of a glass with the macroscopic mechanical properties of a solid is at the core of the long-standing importance of glasses in industry.

A clear example are pharmaceutical products, which are typically formed by crystalline drugs that are poorly water-soluble and show limited bioavailability[5]. On the contrary, amorphous forms show improved solubility[6]. The further development of glass science and technology will permit the overcoming of current drawbacks and will result in the implementation of glasses as main format in pharmaceutical products, minimizing the necessary dose and, therefore, the toxicity and cost of these products. Another important industry, which may strongly benefit from the large-scale use of glasses and its development, is metallurgy. The metal industry represents one of the largest technical sectors in the European Union, accounting for 46% of all EU manufacturing value and 11% of total GDP[7]. The attractiveness of metallic glasses is grounded on their fascinating properties[4,8,9]. The low glass transition temperature and excellent glass forming ability enable easy shaping into complex patterns. The high elastic moduli –similar to human bone-, high elasticity, strength and resistance to corrosion and abrasion make them ideal materials for medical applications. Their excellent magneto-caloric effect permits the fabrication of efficient refrigerators. Their soft magnetism and tuneable magnetic properties are interesting for the development of magnetic devices. Interestingly, the electronic industry also benefits from the appearance and development of glasses[10,11]. The growth of electronic industry, dragged by the massive use of portable personal devices, demands for effective and inexpensive processes to produce the different components. The use of glass technology permits to highly decrease the production cost of these devices and improving their quality.

Unfortunately, in spite of its high impact in society and industry, there is a lack of a satisfactory understanding of the nature of glasses[2,12–14]. For instance, it is not clear at all, if a glass is a distinct state of matter, thermodynamically different from the supercooled liquid or it is just a super-

viscous liquid that appears to be a solid in experimentally accessible timescales. The existence of an underlying thermodynamic transition hidden by the appearance of the glass transition is therefore a subject of strong debate and research in the condensed matter community[13,15–17]. There is also an ongoing discussion on which relevant factors govern the dramatic slowdown of the dynamics of viscous liquids on approaching the glassy state[2,12–14,16,17]. In spite of an intense effort of the scientific community for the last 50 years, there are not commonly accepted theories that provide explanation of this intriguing dynamic behaviour. A complete understanding of the nature of glasses and their supercooled liquids is fundamental to overcome the limitations that exist nowadays and that preclude a wider use in current applications.

2.1 What is a glass? Some Basic concepts

Glasses are generally produced by cooling a liquid at a pace fast enough to avoid the crystallization of the material. The timescale of the dynamical properties of a supercooled liquid increases abruptly when the temperature is reduced. Below a critical point known as the glass transition temperature, T_g, the relaxation time overpasses the experimental laboratory timescale and the liquid becomes a glass. From this transition point, all molecular motion ceases, except for thermal vibrations.

It is important to remark the difference between an amorphous solid and a glass, since these two terms are often used interchangeably in the literature. While the term "amorphous" refers generally to the physical disorder of the system, i.e. lack of structural, configurational or magnetic periodicity, the term glass is often reserved for materials cooled from the melt to rigidity without crystallization. Glasses can also be defined as a disordered system that transforms into a metastable liquid state at a certain temperature below the thermodynamic melting temperature of the crystalline phase. The concept of glass implies, therefore, the consideration of a glass transition from the out-of-equilibrium glass state towards that of the equilibrium supercooled liquid phase, or vice versa. Alternatively, the glass transition is considered as a transition from an ergodic (the supercooled liquid) to a non-ergodic state (the glass). In the liquid state, the forming elements (either atoms or molecules) can explore the entire configurational space during the observation time. In contrast, in the glassy state, the constituents of the system are trapped in a single minimum with insufficient kinetic energy to surmount any activation barrier at the experimental timescale.

In parallel to the slowdown of the dynamics of the system upon cooling, the specific volume, the enthalpy and the entropy of the system decrease. The variation of volume with temperature is known as the expansion coefficient,

$$\alpha_{SCL} = \frac{1}{T}\left(\frac{dV}{dT}\right)_P \quad (1)$$

and the variation of enthalpy with temperature is known as the heat capacity,

$$C_p = \frac{dH}{dT} \quad (2)$$

Once the system falls out of equilibrium, enthalpy and volume evolve at a different pace upon further cooling (Figure 1) and therefore there is a change in the expansion coefficient and the heat capacity.

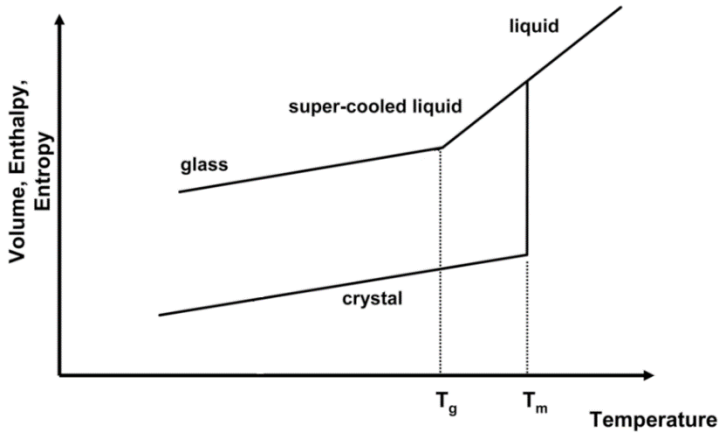

Figure 1 Diagram of volume, entropy and entropy of a supercooled liquid as a function of temperature. Once the supercooled liquid reaches the glass transition on cooling, the variation rate of all of these magnitudes changes, what implies a change on thermal expansion coefficient and heat capacity.

2.1.1 Relaxation time

Glasses and glass-forming liquids are notorious for their extremely complex relaxation dynamics, ranging from picosecond-scale atomic vibrations to thousands/millions of years, in some cases, for aging and densification. The concept of relaxation time of a non-equilibrium system is fundamental in glass science[18]. The relaxation time is considered as the characteristic time associated to the rearrangement of a system once it has been externally altered and moved out from equilibrium. For example, when reducing the temperature of a liquid, its volume does not change immediately, but the process requires a certain amount of time. The relaxation time, which is temperature dependent, governs the dynamics of such a change. In an equivalent manner, the evolution of a glass, which by definition is out of equilibrium, is also controlled by its relaxation time. Some properties of the system, such as viscosity, glass transition temperature, mechanical properties, diffusivity and tendency towards crystallization are strongly influenced by the structural relaxation time of the glass. Dielectric spectroscopy is an extremely useful

characterization technique to measure the relaxation time of liquids, and it is widely used in the scientific community[19]. This technique measures the dielectric properties of the sample as a function of the frequency of an externally applied electric field. The interaction is mediated by the permittivity of the material. The relaxation of the molecules, acting as electric dipoles, gives information concerning the several relaxation processes that may take place in the liquid or in the glassy state.

One of the main characteristics that defines a supercooled liquid approaching the glass transition is the emergence of a two-step relaxation process[12,20], a characteristic that is retained in the glassy state. At high temperatures, correlations among particles decay in time following a stretched exponential function (Figure 2, left). However, at lower temperatures, close to the glass transition, a fast initial decay is observed. This decay is followed by a plateau and a final decay characterized again by a stretched exponential function. Although different relaxation processes are present in supercooled liquids and glasses[12,18,21,22], these two relaxation processes, alpha and beta, are the most relevant. The faster beta relaxation process corresponds to the vibration of the elements around a matrix of more or less rigid atoms (called "cage"). The slower alpha relaxation corresponds to actual rearrangement of particles seeking for thermodynamic equilibrium. In a liquid, the system completely relaxes at a certain moment, while in the case of glasses, the particles remain permanently trapped inside the cage. These processes are named after its position in a typical dielectric spectroscopy diagram (alpha at lower frequencies, beta at higher frequencies, as seen in Figure 2, right).While beta relaxation is responsible for most of the observed phenomena in the glass state[8], the alpha relaxation is directly related to viscous flow and glass transition. In dielectric spectroscopy experiments, it is generally accepted that the system behaves as a glass when the alpha relaxation time exceeds 100 seconds[13,23]. In calorimetry, this is the relaxation time assigned to the system at the glass transition when cooling/heating at 10-20 K/min[24].

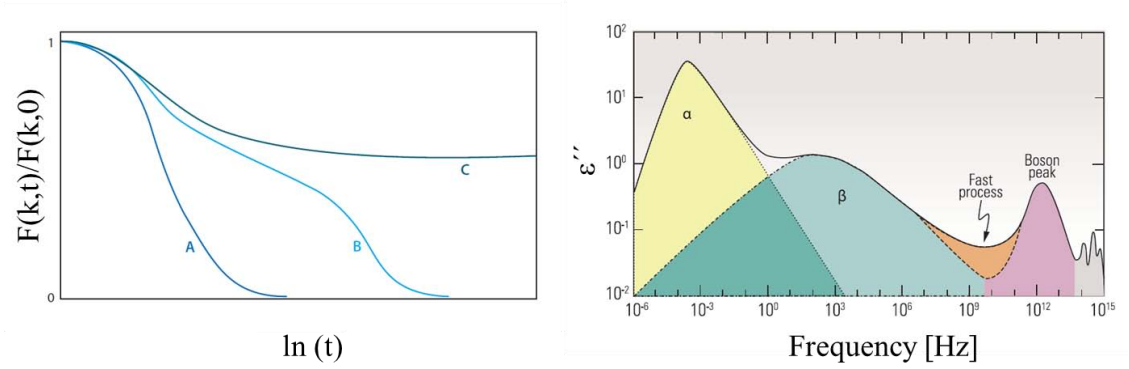

Figure 2 Relaxation processes in supercooled liquids and glasses. a) Typical temporal evolution of the intermediate scattering function[25], associated with dynamic correlations between particles, of a supercooled liquid and a glass at three different situations: A corresponds to a supercooled liquid at high temperature, where the system relaxes and lose the dynamical correlations following a stretched exponential function. This is the alpha relaxation. Curve B represent the temporal decay of the correlation at temperatures close to the glass transition. Before the exponential decay (as observed in A) there is a fast process, the beta relaxation, followed by a plateau. In the case of the glass (C), in the laboratory time scale, no structural relaxation can be observed, only beta relaxation can be measured. b) Typical dielectric spectroscopy spectrum, with different relaxation peaks. At lower frequencies, alpha relaxation dominates, while at higher frequencies, the dominating process is beta. Figures adapted from refs[8,25] respectively.

2.1.2 Fragility index

Fragility is intimately related to the concept of structural relaxation of a supercooled liquid. When plotting the logarithm of the viscosity of a liquid, which is closely related to the alpha relaxation time[12], as a function of T_g/T, different behaviours arise depending on the characteristics of the system (figure 3). This representation permits to classify liquids according to its strong or fragile nature. Strong liquids follow an Arrhenius dependence on temperature. Fragile liquids show non-Arrhenius exponential behaviour. The parameter that is conventionally used to quantify this categorization is the fragility index[12,26,27],

$$m = \frac{d\ log(\eta)}{d\left(\frac{Tg}{T}\right)}\Bigg]_{T=T_g} \tag{3}$$

where η is the viscosity of the liquid. The larger is m, the more fragile is the system. While strong liquids tend to have three-dimensional network structures with strong directional covalent bonds which resist temperature-induced structural changes, fragile liquids are characterized by less directional non-covalent interactions. As a consequence, strong liquids present small or undetectable changes in the heat capacity when crossing the glass transition point[23].

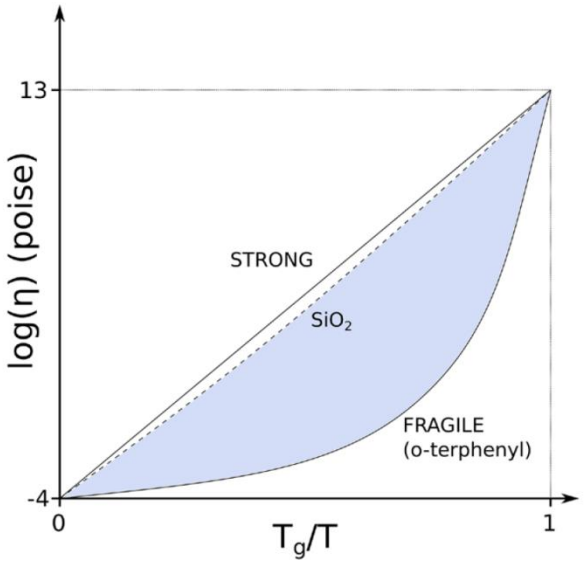

Figure 3: Plot of the logarithm of viscosity as a function of the normalized inverse of temperature for two model materials. Strong materials, such as silica dioxide, follow an Arrhenius expression, while fragile glass formers, such as o-therpenyl, follow a super Arrhenius expression. Figure adapted from ref[23].

2.1.3 Dynamic heterogeneity and breakdown of Stokes-Einstein relationship

A consequence of the two-step relaxation process can be found in the dynamic heterogeneity of glasses and supercooled liquids. The movement of particles trapped into a cage (which corresponds to the particles that are in the correlation plateau) is slow, while those that have left it move very fast. This phenomenon describes a heterogeneous dynamic structure in the glass: zones with dynamically arrested particles, with a strong correlation with the neighbouring particles, and zones where "free" particles diffuse very fast. It should be remarked that this is a dynamical heterogeneity. From a structural point of view, the liquid is nearly invariant with temperature (same as glass)[12] in contrast to the abrupt dynamic change close to the transition temperature. Dynamic heterogeneity is also believed to be the reason for the failure of the Stokes-Einstein relationship (SE). According to this relationship, above the melting temperature of a material viscosity, η, and diffusion coefficient, D, are related,

$$D \sim \frac{T}{\eta} \sim \frac{T}{\tau} \tag{4}$$

where T is the temperature and τ the relaxation time. The violation of SE represents another fundamental characteristic of glasses and supercooled liquids at low temperatures. While diffusion would be mainly influenced by the fastest regions, structural relaxation, and hence, viscosity, is dominated by the slowest areas. When mobility fluctuations become relevant, diffusion and viscosity decouple, violating the SE relation.

2.1.4 The Kauzmann paradox

Although it may seem that the glass transition is a pure kinetic transition, some authors suggest the existence of an underlying second order phase transition, hidden by the dramatic slowdown of the dynamics of the system[13,15–17]. In 1948 Kauzmann showed that the entropy deduced from a specific heat measurement in a high-temperature glass-forming material appears to extrapolate down to a value comparable to the entropy of the corresponding crystalline state at a thermodynamic transition temperature[28]. At this temperature, the excess entropy, defined as the difference in total entropy between liquid and crystal states, vanishes (figure 4). That temperature is currently known as the Kauzmann temperature, T_K. The counterintuitive idea that the entropy of a metastable state such as a supercooled liquid has the same entropy, or even less if further cooling, than the ordered crystalline structure gave rise to the Kauzmann paradox. There are several theories regarding how to avoid this paradox. In particular, some authors have suggested the existence of a second order transition at a temperature between T_g and T_K towards an 'ideal' glass state to avoid the entropy crisis. [12,29].

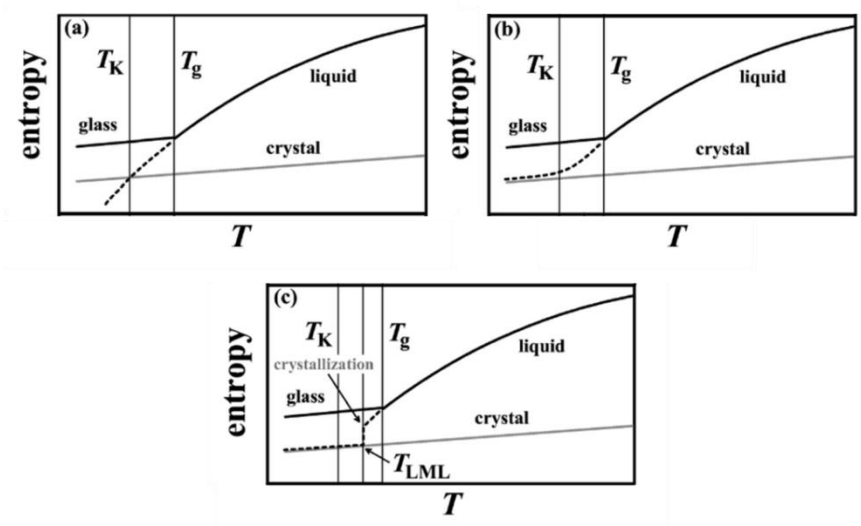

Figure 4 Representation of the Kauzmann entropy crisis. As shown in panel a, the entropy of the supercooled liquid decreases faster than that of the crystal. At T_K, the entropy of liquid and crystal equal. However, the appearance of the glass transition precludes its experimental observation. Panel b shows one possible way to avoid the paradox: close to T_K the entropy of the liquid decreases slower, reaching asymptotically the enthalpy of the crystal. Crystallization may also be a way to avoid the entropy crisis, as observed in panel c. Figure adapted from ref[29].

2.2 Theoretical and phenomenological and phenomenological approaches to the glass transition

Several imaginative and sensible, but often contradictory, ideas have been proposed in an effort to solve the glass transition enigma. Many of them are still alive today, all of them with their own advocates and detractors[12,14,23]. Some of these theories are briefly summarized. Although some of them mainly deal with the supercooled liquid state, rather than the glass, the understanding of the dynamical behaviour of supercooled liquids is fundamental to understand the glass transition.

2.2.1 The Vogel-Fulcher-Tamman (VFT) phenomenological approach

In spite of the many unknowns accompanying the glass transition, some aspects are clear. The relaxation time of the supercooled liquid grows abruptly close to the glass transition, although this dynamical change is not associated to a structural variation. From experimental results, it was found that the relaxation time of supercooled liquids follows a super-Arrhenius expression. Particularly,

$$\tau_R = \tau_0 \exp\left(\frac{DT_0}{T-T_0}\right) \quad (5)$$

This phenomenological expression fits reasonably well a large amount of systems. Its exponential nature agrees quite well with the physical idea that thermally activated processes are responsible for the dynamics at low temperature, in the supercooled region. The parameter T_0 in the denominator of the exponent depends on the fragile or strong nature of the system, taking values from 0 (ideal strong system) to higher values. The parameter D, called strength parameter, is related to the fragility of the system, i.e. larger values of D are typically correlated to more fragile systems. At $T = T_0$, the relaxation time diverges. It is notable the experimentally observed similarity between the parameters T_0 and T_K[27], although some exceptions exist[30]. This similarity is physically reasonable. At T_K the configurational entropy of the real system and that of the crystal are the same and therefore, there is no reason for the system to continue evolving. Still, the coincidence is surprising given the phenomenological nature of this approach.

2.2.2 Adam-Gibbs-DiMarzio (AGM) description

The dynamics of supercooled liquids at low temperature are dominated by thermally activated events. Understanding the behaviour of the relaxation time of these systems means, therefore, understanding the evolution of the potential energy barriers. In particular, for fragile systems,

there is an increase of the height of the potential barriers when decreasing the temperature. The critical point of this interpretation is to identify the physical mechanism behind the evolution of these barriers.

Relaxation of a supercooled liquid or a glass implies rearrangement of molecules. Considering the short range interaction between molecules the process must be local in space, i.e. a certain amount of molecules has to locally rearrange to achieve equilibrium, to relax. This is already considered in the Potential Energy Landscape approach (PEL)[23]. The rearrangement process needs certain amount of energy and, therefore, energy barriers arise. The larger the size of the molecular domain of rearranging particles, ξ, the larger the energy of the barrier. In this way, the problem of the evolution of energy barriers with temperature is analysed through the evolution of these regions with temperature. From critical phenomena, it is known that the relaxation time scale as $\tau_R \sim \xi^z$, being z a real number. In supercooled liquids, where activation processes are responsible for the evolution of its relaxation time, we can approximate $\tau_R \sim \exp\left(\frac{\Delta}{k_B T}\right)$, where Δ is the activation energy, $\Delta = \xi^{\psi}$, being ψ a given real number[12].

The key idea of Adam and Gibbs (AG) is that, at low temperatures, relaxation proceeds through the rearrangement of larger and larger regions of correlated particles, which they called Cooperative Rearranging Regions (CRR) and are defined as the smallest regions that can be rearranged independently of their surroundings. The configurations that each CRR can adopt are very limited, since all its constituents are strongly dependent. According to AG, the number of these configurations, Ω, is constant with respect to the size of the CRR and to temperature. From mechanical statistics considerations, this number can be related to the configurational entropy of the system, S_C. In particular, in AG formalism, the number of particles inside each CRR, n(T), can be expressed as $\mathrm{n(T)} = \frac{log\Omega}{S_C(T)}$. Given the analogy between n and ξ one can finally express the relaxation time of the system as a function of its configurational entropy,

$$\tau_R \sim \exp\left(\frac{B}{TS_C(T)}\right) \tag{6}$$

where B is a constant that depends on the material. The precise behaviour of the configurational entropy at each temperature is system dependent and can be related to the difference in specific heat of the system between the liquid and crystal state, assuming that the configurational and excess entropy are approximately equal[12]. According to this model, the configurational entropy of the system is assumed to vanish at the Kauzmann temperature. In that manner, one can write $S_C(T) = \int_{T_K}^{T} \frac{\Delta c_p}{T} dt$. In AG formalism, the difference in heat capacity of liquid and crystal, Δc_p, is assumed to be temperature independent and hence, $S_C(T) = \Delta c_p \log\left(\frac{T}{T_K}\right) \sim \Delta c_p \left(\frac{T-T_K}{T_K}\right)$.

Finally, the relaxation time of the system can be expressed as $\tau_R \sim \exp\left(\frac{T_K}{\Delta c_p T(T-T_K)}\right)$. When T is far from 0 and close to T_K, the final expression of the relaxation time of the system is obtained[12],

$$\tau_R \sim \exp\left(\frac{A}{T-T_K}\right) \quad (7)$$

where A contains all constant terms. This expression is analogous to the empirical VFT expression, where T_K is used instead of T_0. Given that it has been experimentally verified that for most systems the parameter T_0 remarkably coincides with T_K[27], the AG formalism could be considered as the theoretical frame for the VFT expression. In spite of its elegance, this approach has certain limitations due to the various approximations made. The most important is the assumption of a constant number of configurations that a single CRR can adopt, regardless of its size[12].

An important assumption in the AG formulation is that structural equilibrium is maintained at all temperatures, which precludes the use of equation 7 in the glassy state. However, a generalization of AG formalism is possible by considering $S_C(T)$ a function of fictive temperature, which is an indicator of the stability of the glass, as commented in next section. Following this approach, the Adam-Gibbs-Vogel (AGV) equation is derived,

$$\tau_R(T, T_f) \sim \exp\left(\frac{A}{T\left(1-\frac{T_K}{T_f}\right)}\right) \quad (8)$$

For the supercooled liquid $T = T_f$, and equations 8 and 7 are equivalent. Although this generalization has been used with some success to describe relaxation processes in glasses, such as aging experiments[31], it is not as recognized as the conventional AG formalism[32].

2.3 Glass stability

The non-equilibrium nature of glasses is at the core of the difficulties encountered for their widespread use in many industrial applications. The equilibrium phase below the melting temperature is the crystal; therefore, any external perturbation may induce the more or less fast crystallization of the system. Moreover, a glass constantly evolves towards a more stable configuration, trying to reach the metastable supercooled liquid phase. This process is called aging. Aging processes are very complex and are a subject of intense investigation[21,22]. In any case, a variation of the properties of glasses with time is undesirable for their commercialization, since knowledge of the very exact properties of the product is strongly required.

Glasses are traditionally produced by cooling a material from its supercooled liquid state. The dynamics of the liquid become progressively slower upon cooling, and the relaxation time

increases. Above certain value of the relaxation time, the equilibration time, i.e. the time that the system requires to explore the whole configurational space, is larger than the experimental time. When this happens, the system is, from the point of view of the experimentalist, no longer ergodic and only particular positions in the phase space are accessible when measuring any of its properties. A glass has then been formed. The arbitrary nature of the definition is noted. Conventionally, when the relaxation time of the system is larger than 100 s, it is considered that the apparent ergodicity is broken and the temperature at which that occurs is considered as the glass transition temperature.

From the above consideration it is obvious that the laboratory time scale is crucial to determine the value of the glass transition temperature. Indeed, T_g is influenced by the cooling rate (figure 5), at a level that is determined by the behaviour of the dynamics of the supercooled liquid, i.e. its fragility. When the system is rapidly cooled, the provided time is very limited and hence the system will become a glass at relatively high temperatures. On the other hand, if the cooling rate is slow, the ergodicity condition is fulfilled up to lower temperatures and the glass transition will be delayed. The entropy of the liquid is reduced upon cooling and consequently a glass formed by cooling slower will reach a lower position in the energy landscape and will therefore be more stable. Unfortunately, the rapid increase of the relaxation time of the supercooled liquid, especially in the most fragile liquids, constraints the production of highly stable glasses directly from the liquid state.

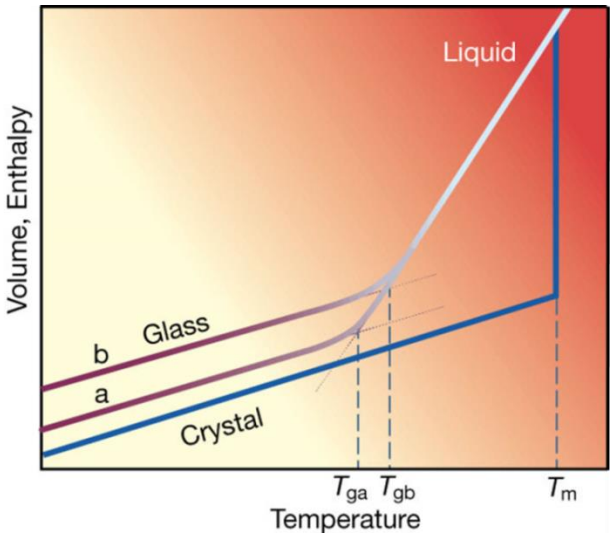

Figure 5 Volume and enthalpy of glasses cooled at a different cooling rate. Glass "a" has been formed by cooling the liquid slower than glass "b". For glass "a", the equilibration of the system is maintained up to lower temperatures... In this case, glass transition temperature and limiting fictive temperature are equal (see section 2.3.1)Figure extracted from ref[13].

As considered previously, the fact that glasses are out of equilibrium implies that the system will slowly rearrange to reach the stability of the metastable supercooled liquid state. However, this process is hindered by the extremely long times required for rearrangements of the local structure. Furthermore, after the system has made certain progress in stabilization, higher potential barriers appear and longer times are required for further stabilization. The process is, therefore, extremely inefficient. One clear example of an aged glass can be found in ambers, which are glasses that have been naturally aged during millions of years, attaining very high stabilities.

2.3.1 Limiting fictive temperature

When dealing with glass stability, the concept of fictive temperature is of paramount importance. While liquids, as *equilibrium* system, can be fully described by temperature and pressure, the properties of a glass also depend on their thermal history. In 1932, Tool and Eichlin proposed to describe the glass as equivalent to a liquid state at a different temperature, which was initially called "equilibrium temperature". Later on this terminology evolved to the actual one "fictive temperature"[33,34]. As noted by Gardon and Narayanaswamy, the fictive temperature depends on the thermodynamic temperature of the system[33,35]. In the liquid (SCL) state, both temperatures coincide. During vitrification, the fictive temperature slowly deviates from the thermodynamic temperature and finally converges towards a constant value dubbed limiting fictive temperature, T_f'.

Although the fictive temperature was defined initially from a structural point of view, in general different physical observables have different limiting fictive temperatures[36]. When the glass is above its limiting fictive temperature, it will recover the characteristics of the liquid, in particular its dynamics, in a process known as physical rejuvenation or annealing (figure 6). Below T_f', the glass will age, increasing its stability with time, eventually reaching the dynamics of the liquid state.

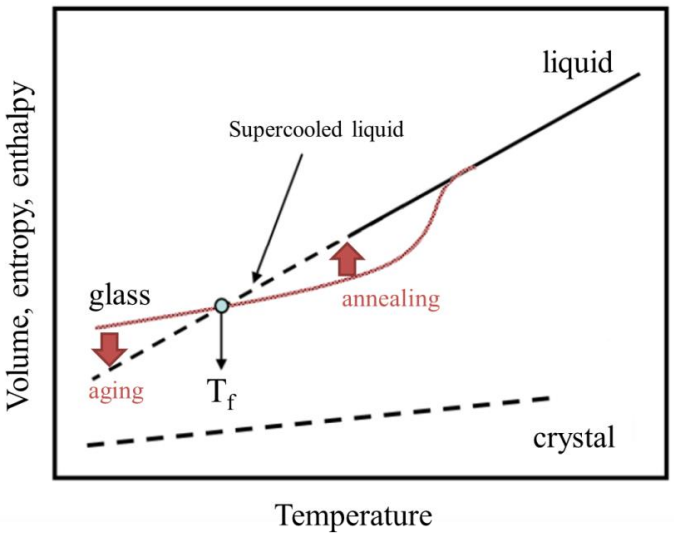

Figure 6 At the limiting fictive temperature, the measurement of a given magnitude yields the same value for the glass and the supercooled liquid, i.e. at the enthalpic T'_f the glass and the liquid have the same enthalpy. Below this temperature, the glass will age increasing its stability with time. Above T_f', the glass will rejuvenate into the liquid state.

2.4 Glasses obtained by physical vapour deposition

Recently, a new procedure to obtain very stable glasses has been discovered. This process consists on growing thin film glasses from the vapour phase at specific deposition conditions[37]. Following this methodology, glasses with unusual high stability can be prepared in short time scales, as represented in Figure 7. These glasses compare in stability to ambers aged in nature for hundreds of millions of years. These glasses are typically called "ultrastable glasses", as opposed to conventional glasses, produced from the liquid phase. The mechanism responsible for the enhanced stability of vapour-deposited glasses is believed to be the high mobility of the particles at the free surfaces, which can be as high as 10^7 times[38] their mobility in the interior of the glass, from now on called bulk. Thus, when the molecules arrive to the substrate, they have enough mobility to explore the whole configurational space and find the most favourable positions. The stability of the prepared layers depend on the deposition rate[39,40]. If the rate is set sufficiently low, the particles have enough time to find a favourable position before being buried by the incoming particles. Once buried, their mobility is no longer enhanced and dramatically slows down. This enhancement takes place also at low temperatures, much below the glass transition temperature. In other words, during deposition the particles at the surface of the glass are fast enough to reach the metastable equilibrium state, even at temperatures at which the equilibration time (structural relaxation time) is extremely high. However, when substrate temperature is too low the particles are not able to reach equilibrium for two reasons i) equilibration time is too high at these

temperatures and ii) the kinetic energy of the incoming particles is strongly reduced due to the low temperatures of the substrate. In fact, incoming particles get stuck into a non-favourable energetic position, giving, as a result, a less stable glass than those obtained at intermediate temperatures. It is an empirical evidence that most vapour-deposited glasses attain the maximum stability at deposition temperatures in the vicinity of $0.85T_g$. A convenient concept which is used when discussing about vapour deposited glasses is that of "equivalent cooling rate". This rate is defined as the cooling rate that would have to be imposed in order to produce a glass with the same stability.

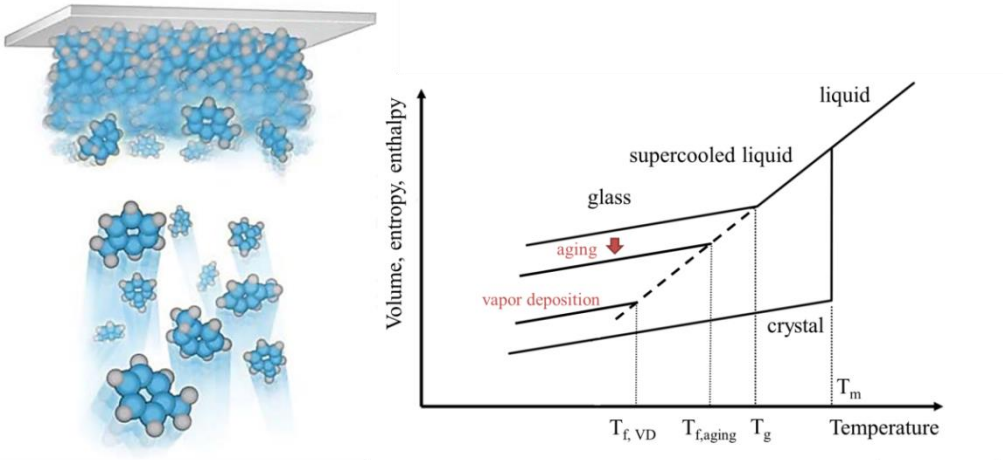

Figure 7 During physical vapour deposition, the molecules arrive to the substrate at a very slow rate, letting the surface molecules equilibrate before being buried by the incoming particles. These glasses possess a much lower enthalpy than ordinary glasses, even after being submitted to an aging treatment. Therefore, their limiting fictive temperature, $T'_{f,VD}$, is much lower. Figure adapted from ref[41].

Physical vapour deposited glasses present a series of particular and striking properties that have never been observed before in other systems. Ultrastable glasses, those deposited around $0.85T_g$, exhibit transformation times 10^4-10^5 times higher than conventional glasses, which have been cooled at -10 K/min from the liquid state. Moreover, ultrastable glasses exhibit other properties which are of special interest from an industrial and commercial point of view but also from a theoretical perspective, as these systems represent a new benchmark to test and develop glass transition theories:

- The density of a glass is correlated with its stability. Vapour deposited glasses can be up to 1.5% denser than conventional glasses[42].

- The enthalpy and the specific heat of highly stable glasses are lower than that of conventional glasses[43].

- Glasses with high stability present higher sound velocity and higher moduli than conventional glasses[44–46]. Their thermal expansion coefficient is also lower[42].

- One of the most striking characteristics of vapour deposited glasses is that, depending on the evaporation conditions (temperature and rate), they can exhibit molecular anisotropy, which is expressed with a pre-peak in a typical X-ray diffraction pattern[47–50]. They also present optical birefringence, associated with a preferred molecular orientation[42,49]. It should be noted that these characteristics are, in principle, independent of the stability of the glass.

- The efficient packing arrangement of vapour deposited glasses, especially of the most stable ones, is the cause for the change in the transformation mechanism from glass to liquid. Conventional glasses transform via a homogenous process that takes place simultaneously in the whole volume of the glass. In vapour deposited stable glasses the transformation starts at the surfaces and interfaces and propagates into the bulk as a transformation front[43,51,52].

- Two level systems, considered to be a universal feature of glasses at very low temperatures (around 1 K), are not observed in ultrastable glasses[53]. The special packing arrangement of these materials is thought to be at the core of this observation.

Many of these characteristics are under intense investigation. In particular, this work will discuss on some of these striking properties.

2.5 Heat capacity signature of glasses

Heat capacity is one of the most widely used magnitudes to study the glass transition. *If you are allowed to measure only one property of a material, make sure it's the heat capacity*, said Albert Einstein. And with good reason, since this physical magnitude gives valuable information about the properties of the glass. In fact, it is difficult to conceive a comprehensive study of any glassy system in which a calorimetric analysis is not present.

Heat capacity is, by definition, the amount of heat that must be added to a system in order to change its temperature by one Kelvin. Temperature takes account for the mid kinetic energy of the particles of a system with respect to its centre of mass. Heat, on the other hand, refers to the transfer of energy from one system to another without exerting any work. Heat changes temperature. Depending on the physical configuration of the system, the effect of heat on temperature is different. The physical magnitude that regulates this change is heat capacity. In particular, heat capacity depends on several factors. As an extensive magnitude, heat capacity depends on the mass. However, after proper normalization, it only depends on intensive properties such as the degrees of freedom of the constituents (translational, rotational or vibrational). Heat

capacity is also related to other physical properties, such as thermal conductivity, electromagnetic interaction among constituent particles.... During a second order phase transformation there is a step change of the heat capacity Although glass transition is generally not considered to be a true thermodynamic phase transition, rather a kinetic change, it also shows a step in heat capacity.

Heat capacity can give us an important amount of information regarding the physico-chemical properties of the system, in particular of glasses. The change in heat capacity during the glass transition is a clear signature, easy to observe, which gives us information regarding the kinetic and thermodynamic stability of the glass. The shape of the heat capacity curve during the transition provides also information about how the glass is transforming. From the integration of the heat capacity curves with respect to temperature we obtain information about the change of enthalpy, which, at the end, indicates the thermodynamic stability of the glass and permits the comparison between the glass and the crystalline phase.

The signature of the glass transition when measured by calorimetry consists on a jump in the heat capacity measurement (figure 8, left panel). The heat capacity of the glass is lower due to the limited number of accessible states in the glass in comparison to the liquid, which can freely explore the entire configurational space.

The measurement of the heat capacity is typically performed on heating experiments. The transition from the glassy to the liquid state is identified from the onset of devitrification, T_{on} (figure 8, right), which depends on the heating rate. The lower the heating rate the lower the onset of devitrification, since the system has more time to relax at any temperature. Glass transition temperature and onset of devitrification can only coincide if the cooling rate imposed in the preparation of the glass, or if the equivalent cooling rate in vapour deposited glasses, is equal to the heating rate imposed during the measurement. In the case of ultrastable glasses, since the equivalent cooling rate is extremely low, the access to the calorimetric T_g is practically unfeasible and $T_g << T_{on}$.

The onset temperature of devitrification is associated to the kinetic stability of the glass. Glasses with high kinetic stability present, for the same heating rate, high values of the onset temperature. Also, a shift of the calorimetric peak is generally associated to an increase of the enthalpy of excess during the transition, as can be observed in figure 8. Instead, the limiting fictive temperature is used in order to determine the thermodynamic stability of the sample. Integration of heat capacity data yields the enthalpy of glass and liquid. The enthalpic limiting fictive temperature is defined as the temperature at which the enthalpy of the glass and liquid coincide.

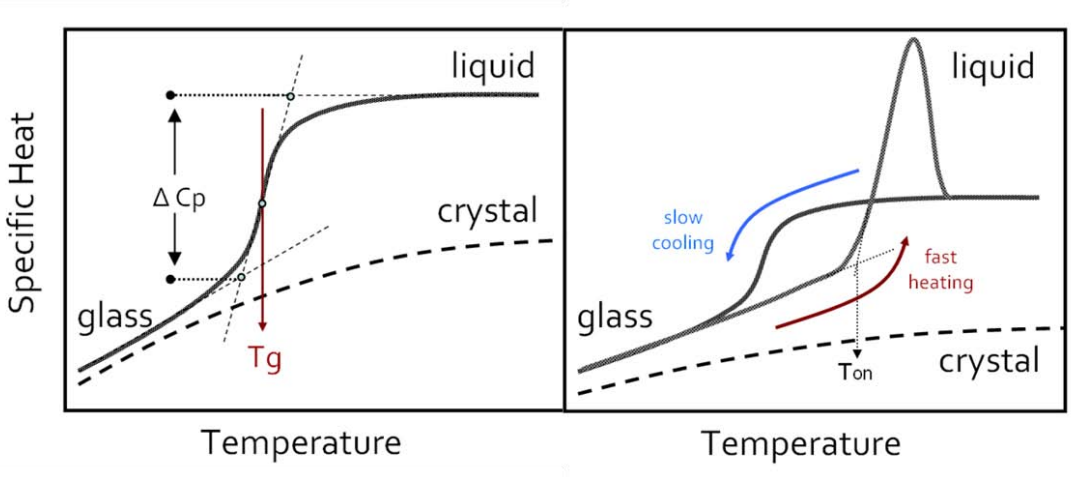

Figure 8 Heat capacity of a system during the glass transition. The left panel shows the typical heat capacity jump. The heat capacity of a glass is lower given the reduced number of states that the system explores during the provided timeframe. The right panel shows the influence of the heating rate on the glass transition. When the heating rate imposed during the heat capacity measurement is different than the cooling rate, devitrification takes place at different temperatures. The transition temperature on heating is called "onset temperature". In this case, T_{on} and T_f' are not equivalent. Figure adapted from ref[54].

3. EXPERIMENTAL METHODS

3.1 Chapter introduction

Physical vapour deposition (PVD) describes a variety of vacuum deposition methods which can be used to produce thin films. PVD relies on a physical process (such as heating or sputtering) to produce vapour from the target material, which is then deposited on a substrate. PVD is used in several industries and for a broad variety of applications, such as thin film solar cells, protective coatings, integrated circuits, etc. Moreover, as commented in chapter 2, it has proven to be a powerful technique to prepare, in short time scale, glasses with unusual thermal stability and striking properties. PVD processes require vacuum environment. Vacuum, by definition, is space empty of matter. The word stems from the Latin adjective “vacuus” for "vacant" or "void". However, this simple concept hides an extended and complex technology. Depending on the developed process, particular levels of vacuum are needed, what requires the use of specific equipment. The contaminating elements, such as water, also play an important role, especially during the deposition of organic molecules. Special hardware, such as cold traps, is of vital importance in this case.

The advanced characterization of PVD glassy samples requires a combination of conventional and newer techniques together with an accurate data analysis. Conventional calorimetry is a particularly relevant characterization technique, but membrane-based calorimetry techniques are better adapted to access properties of thin-film glasses, from molecular to metallic, with unprecedented sensitivity in a broad temperature range, never attained before. Among them, one of the most promising techniques is quasi-adiabatic fast-scanning nanocalorimetry, which permits the measurement of nanometer thick layers with an extraordinary resolution level by imposing ultra-fast heating rates of the order of 10^5 K/s.

3.2 The physical vapour deposition process

Deposition techniques can be broadly divided in two categories: chemical or physical deposition, depending on the nature of the process.

In chemical depositions, a precursor fluid material in the vapour phase undergoes a chemical change on the surface of the substrate, producing a solid layer as a result. In physical depositions, on the other hand, instead of chemical reactions, thin films are produced by means of mechanical,

electromechanical or thermodynamic processes. Generally, physical deposition is achieved by evaporation of a precursor material which is subsequently deposited onto a substrate. For that reason, physical deposition is generally referred as physical vapour deposition (PVD). There are different ways of producing the vapour, for instance heating a filament or bombarding the surface of the precursor with accelerated electrons or ions. A substrate is placed at a certain distance from the vapour source. Its surface is at favourable energetic conditions, so that the impinging molecules lose their energy and land onto it, forming a thin layer. Evaporated molecules can only travel if a vacuum environment is guaranteed and the properties of the layer will depend on the quality and composition of the vacuum environment.

Slow deposition rates and adequate substrate conditions are the requirements for the the formation of stable glasses with unprecedented stability[37]. In this work, we have produced glasses of two crystalline pharmaceutical products with relatively low melting temperature (around 430 K) and high vapour pressure near the melting point. Thermal evaporation is, therefore, the most suitable technique.

3.2.1 Vacuum generation and measurement

One of the main components of an evaporation chamber is the vacuum setup. In this work we use a turbomolecular pump attached to a dry scroll pump in order to generate a vacuum level of around $3 \cdot 10^{-8}$ mbar. While turbomolecular pumps are very efficient removing molecules of a considerable size, smaller molecules, such as hydrogen or water are more difficult to remove. In fact, the base pressure of a system pumped by a turbomolecular pump is mainly determined by water and, especially, by hydrogen atoms. While the latter are extremely difficult to remove, it is possible to avoid the residual water molecules to circulate across the chamber, contaminating the produced sample and contributing to the base pressure of the system. To do that, one can take advantage of the condensation of water at low pressure, which takes place at 180 K, and use cold traps. In this work, we use a specially designed cold trap, which consists on a copper recipient connected to one of the ports of the evaporation chamber (Figure 9). When the recipient is filled with liquid nitrogen, the copper is refrigerated down to 77 K and the residual water molecules get stacked on the surface of the trap. The speed of adsorption of water molecules on the trap is proportional to its surface. Therefore, in order to further increase the equivalent pumping speed of the cold trap, several copper disks are attached to the container.

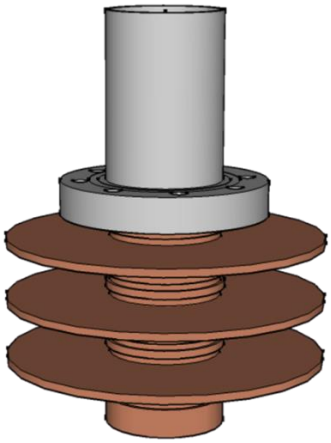

Figure 9. Sketch of the nitrogen cold-trap used in this work.

In order to measure the pressure of the system we have installed a Bayard-Alpert hot filament ionization gauge. This vacuum gauge is one of the most used vacuum measuring devices, able to work in the range from 10^{-4} to 10^{-10} mbar.

3.2.2 Thermal evaporation

As commented in Chapter 2, the key features for the formation of ultrastable glasses are a slow evaporation rate and the adequate substrate temperature. In order to reach a deposition rate of around 1 Å/s at the surface of the substrate the material is heated up to a temperature slightly above the melting point. In this work we use an effusion cell that permits an accurate control of the vapour pressure inside the cell so we can easily tune the deposition rate. The evaporation source (Figure 10) consists on a crucible, made of stainless steel, containing the raw material. The loaded crucible is heated by radiation from a tantalum filament at the set temperature. The vapour pressure of the precursor material increases inside the cell and starts to evaporate at a rate determined by the Hertz-Knudsen law for effusion cells,

$$\frac{dN_e}{dt} = A_e(2\pi m k_B T)^{-\frac{1}{2}}(P' - P) \tag{9}$$

where N_e is the number of evaporated particles, m is the particle mass, A_e is the area of the crucible mouth, k_B is the Boltzmann constant, T is the temperature, P' is the partial pressure of the evaporated material inside the cell and P is the base pressure of the chamber. Depending on the distance between cell and substrate, a given deposition rate will be achieved, according to the cosine law of evaporation,

$$\frac{dM_c}{dA_c} = \frac{M_e}{\pi r^2} cos\varphi cos\psi \tag{10}$$

where M_c and A_c refer to the condensed mass and area respectively, M_e refers to the evaporated mass, and r, φ and ψ are depicted in Figure 11. In particular, if A_c defines the surface of a sphere of radius r_0, then $= cos\psi = \frac{r}{2r_0}$, and a constant evaporation rate will be achieved.

$$\frac{dM_c}{dA_c} = \frac{M_e}{4\pi r_0^2} \tag{11}$$

The uniformity of the temperature profile in these cells is excellent, what guarantees that all the material inside the crucible is at the same temperature and the evaporation rate is kept constant, even for large material loads. The construction material of the crucible limits the maximum temperature that it can reach.

In order to control the evaporation rate and be able to fix it to an adequate value, we have used a quartz crystal microbalance. In this work, we typically use an evaporation rate of 0.1 nm/s.

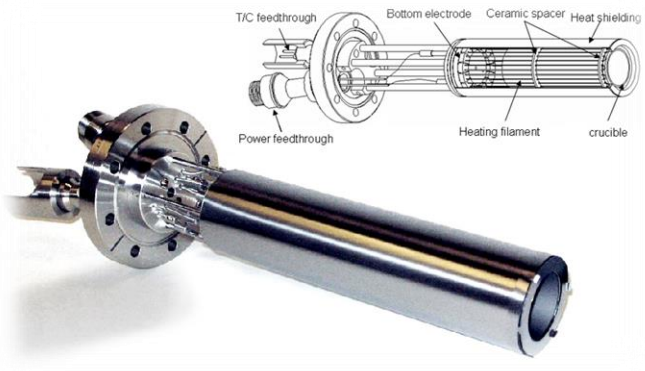

Figure 10. Image of the effusion cell used in this work. In the inset, a drawing of the different parts of the cell.

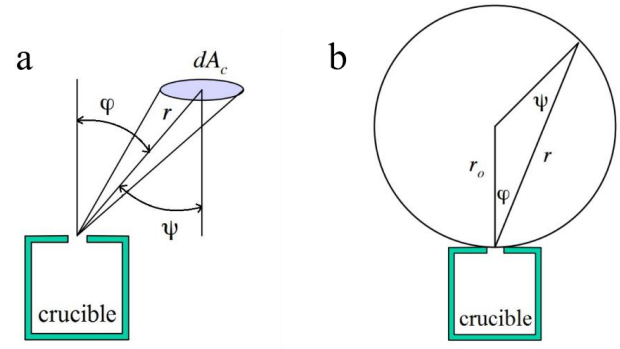

Figure 11. a) Representation of the position of an area element A_c, where the deposition rate follows the Cosine law of evaporation. b) If dA_c defines a sphere the evaporation rate is constant for all the surface.

3.3 Characterization techniques

Different characterization techniques have been used to analyse the peculiar behaviour of vapour deposited glasses. For example, the study of the structure of ultrastable glasses of different organic materials by means of wide angle x-ray scattering, WAXS, have shown that these glasses present structural anisotropy[47–49]. The study of their optical properties by ellipsometry has confirmed the existence of birefringence[42,55]. The use of Brillouin light scattering has shown how the bulk, elastic and Young moduli of ultrastable glasses are higher than those of the conventional counterpart[45].

One of the most widely used magnitudes to study glass transition and the properties of glasses is heat capacity. The measurement of heat capacity basically consists on adding heat to the studied system and measuring the effect on its temperature. Obviously, various complications appear, the most important of which is the heat exchange between the analysed sample and its environment, i.e. the non-adiabaticity of the process. Also, the sensitivity of the technique is a critical factor, of special relevance after the boost of nanotechnology and the work on thin-films and other nanomaterials. In order to solve these and other drawbacks of the measurement, different analytical techniques have been developed throughout history, progressively gaining sophistication. One of the oldest and still more used calorimetric techniques is differential scanning calorimetry (DSC). This technique was developed in 1962 and commercially implemented in 1964. Since then it has been a preferred choice to carry out thermal experiments. The information that can be extracted from DSC data goes beyond the measurement of heat capacity, which is a tedious procedure. For example, it permits the analysis of the energy involved in a variety of reactions, including phase formation, crystallization, glass transition, or even relaxation processes, especially during isothermal experiments.

in the last 20 years, a powerful family of techniques that permit the calorimetric analysis of minute amounts of mass (in the ng range or even lower) emerged into the scene. They are dubbed with the generic name of membrane-based nanocalorimetric techniques. Fast-scanning quasi-adiabatic nanocalorimetry, a prominent member of this family, is probably the champion in sensitivity since it can access heat capacity of single monolayers grown on a very thin membrane.

3.3.1 Differential scanning calorimetry (DSC)

Differential scanning calorimetry relies on the monitoring of heat flux and temperature of two almost identical cells, sample and reference. There are two modalities of this technique: heat-flux and power compensation DSC, as schematically represented in Figure 12. In the heat-flow

modality, the two cells are heated in a common oven, being the heat flux equal in both cells. The temperature is monitored continuously during a heating ramp or an isotherm. The difference in temperature between both cells gives information about the heat capacity of the sample, including any reaction. Similar to the heat-flow DSC, the Differential Thermal Analysis (DTA) also records the difference in temperature between two quasi-identical cells under the same heat flow injection. However, while heat-flow DSC permits the extraction of data concerning specific heat of a given process, DTA only yields information about characteristic temperatures. In the power compensation scheme of DSC, both cells are heated independently in different furnaces, in order to keep them at the same temperature during a certain heating ramp or isotherm. Different power will be injected to each cell depending on the heat capacity of the sample and the reference cells in order to maintain both at the same temperature. For the present work, a power compensation DSC from Perkin Elmer DSC7 has been used to perform the DSC experiments described in the following chapters.

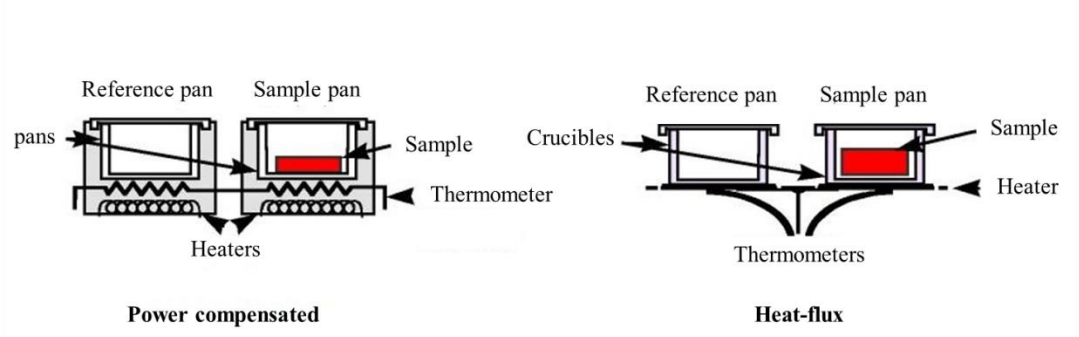

Figure 12. Schema for the operation principle of the two DSC modalities. While in heat-flux DSC both cells are heated in the same oven and the supplied power is the same, in power-compensated DSC, each of the cells are heated independently, receiving different amounts of heat, in order to keep them at the target temperature.

In DSC experiments, the condition of adiabaticity is not fulfilled. In fact, it is physically impossible to avoid heat transfer in any process. However, the use of two similar cells and almost identical aluminium sample pans and the consideration that heat losses for both of them are equivalent, permits the evaluation of the heat capacity of the sample. Temperature programs are effectively performed thanks to the short conduction paths between sample and heater elements and the small mass of the cells. The accessible heating and cooling rates when using conventional DSC techniques are limited. Typically, the heating/cooling rates imposed in calorimetry experiments range from 0.1 K/min up to 50 K/min. A wider rate interval is accessible depending on the sophistication of the system, in particular its ability to follow fast heating/cooling ramps while guaranteeing proper temperature homogeneity across the sample.

In order to obtain reliable values of temperature, energy and heat capacity, a proper calibration procedure should be carried out. Temperature and energy calibration are performed by measuring reference materials with known temperature and latent heat of a specific reaction. For this work, the melting temperature and the heat of fusion of a known mass of indium have been used for that purpose. The calibration factor depends on the heating rate and, therefore, a new calibration must be performed when setting different heating rates in the measurements. Concerning the calibration for heat capacity measurements, a more tedious produce must be performed. In that case, it is necessary to use a material with well-known heat capacity, conventionally synthetic sapphire. Also, the measurement of the baseline, i.e. the DSC measurement performed on empty cells, is necessary to obtain the heat capacity of the sample. Due to the lack of reproducibility of the baseline of the DSC employed in this work, an alternative method has been used to determine the heat capacity of the samples. For each specific mass and after baseline subtraction, the well documented specific heats of the glass and the liquid[56,57] have been imposed to the measured calorimetric signal, converting it to specific heat. The approach yields curves in excellent agreement with those obtained using standard procedures, which become essential when the specific heats are not well-known.

3.3.2 High-pressure differential thermal analysis (HP-DTA)

In this thesis, a home-made DTA calorimeter designed and constructed at the Group of Characterization of Materials (GCM) of the Universitat Politècnica de Catalunya was used to perform calorimetric measurements on ultrastable and conventional glasses at variable pressure. As a DTA, the principle of operation is based on the differential temperature measurement of two almost identical cells heated in the same oven. In this case, however, the external pressure applied to the sample cell can be tuned. The design of this device is similar to previous reported models[58]. The sample is introduced in a tin crucible. An inert perfluorinated liquid is introduced in the crucible together with the sample to guarantee a proper pressure transmission before hermetically sealing the cell. The temperature of the cells is measured through a type-K thermocouple in close contact with the sample. The pressure into the calorimetric block is transmitted by compressing a cryogenic liquid and is measured by calibrated Bourdon gauges with accuracy better than 5 bar. More details about this experimental setup can be found elsewhere[59].

In this kind of setup, the imposed heating rates are limited. In order to reliably guarantee the proper thermalization of the sample during the heating ramp without altering the pressure reading, a maximum heating rate of 2 K/min is imposed. On the other hand, the sensitivity of this home-made setup is more limited than in the case of a commercial conventional DTA and therefore,

some features of the calorimetric signal such as peak shape or area are not completely reproducible and should be carefully considered.

3.3.3 Quasi-adiabatic fast-scanning nanocalorimetry

Conventional calorimeters face two main disadvantages. First, the heating rates that can be imposed during calorimetric measurements are limited across a restricted range, determined by the thermal conduction between the cell and the sample. Apart from the limitations in controlling and monitoring a fast heating rate, the presence of temperature gradients in the sample during the scan would yield inaccurate results. Another disadvantage of conventional DSC systems is the resolution of the device. Although the differential measurement excludes from the final calorimetric signal the information coming from the surrounding of the sample, the resolution of the signal is hindered by the large mass of the addenda.

Thanks to the last advances in micro and nanofabrication, it has been possible to fabricate micro devices capable of integrating several circuits developing multiple functions with a much reduced mass. This fact has induced the emergence of a new family of calorimetric techniques: membrane-based calorimeters. The new methodologies and associated instrumentation rely on the use of very thin dielectric free-standing membranes (less than few hundred of nanometers thick), generally made of silicon or silicon nitride, on top of which different elements are integrated, generally thermal sensors and heaters. The membrane itself acts as a substrate. The advantages of this construction are remarkable. In differential configuration permits the measurement of samples with a mass much lower than the one of the membrane itself. In other words, the sensitivity of these calorimetric techniques is dramatically increased, up to picojoules per Kelvin[60] at room temperature Also, the thermal link between heater, sensor and sample is almost ideal, which lets a very fast heat transfer and, therefore, the possibility to study ultra-fast dynamics on the sample.

Specifically, fast-scanning quasi-adiabatic nanocalorimetry relies on the use of very fast heating rates, up to 10^6 K/s, induced by the injection of intensity micropulses[60]. The use of high heating rates for measuring the heat capacity of a sample has several advantages, among them: i) it reduces the noise in the calorimetric signal and, therefore, permits the measurement of samples with lower mass, ii) it avoids that the heat injected into the sample diffuses to the surroundings, fulfilling in this way adiabatic conditions, iii) high heating rates guarantee a good temperature homogeneity in the sensor and precise measurements of heat capacity, since in vacuum conditions heat is not able to propagate beyond the sample. The small masses involved in the measurement process also

permit the generation of very fast passive cooling rates in high vacuum, around 500 K/s, or much faster if a gas partially fills the vacuum chamber, which allow the production of fast cooled (FC) glasses.

Denlinger et al. were the first to report the realization of a membrane-based calorimetry. It consisted on an amorphous silicon nitride 180 nm membrane with integrated thin metallic films, exhibiting a total addenda of $4 \cdot 10^{-6}$ J/K at room temperature, 100 times lower than previous cells and with higher sensibility[61]. Fast-scanning nanocalorimetry was developed, on the other hand, by Allen and co-workers[62] in 1995, combining the membrane-based technology with the pulse heating technique developed previously by Worthing on thin wires[63].

3.3.3.1 Device description and microfabrication process

The devices used for fast-scanning quasi-adiabatic nanocalorimetry consist on microfabricated silicon chips, shown in Figure 13. A silicon nitride free-standing membrane with a thickness of around 180 nm is held by a silicon frame. On one side of this membrane, a thin-film platinum serpentine circuit of around 100 nm thick is deposited, which acts both as temperature sensor and heater. Four contacts of platinum permit the external connection to the control devices (intensity source and voltage acquisition system). The area that is occupied by the metal serpentine is referred as the sensing area, defining the area of the membrane which will be heated.

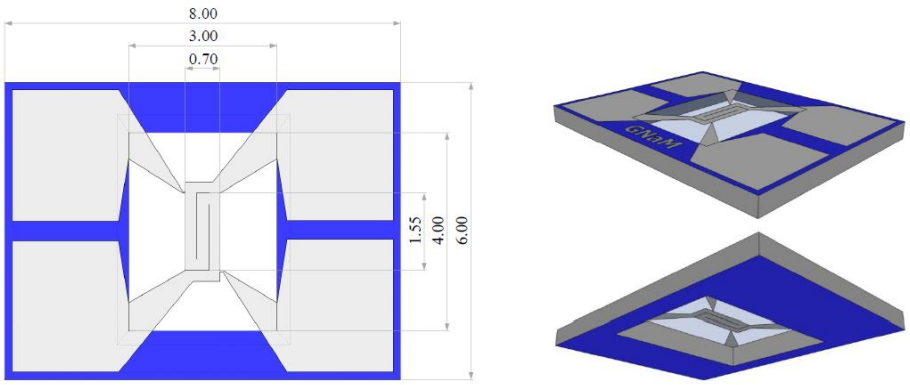

Figure 13. Sketch of the nanocalorimetry device, with the more significant sizes in mm and viewed from different angles.

The microfabrication process is succinctly illustrated in Figure 14. Basically, a silicon wafer is coated with a silicon dioxide and a silicon nitride thin layer (b). After opening a small window on these surface layers on one side of the wafer (c) and depositing the necessary metallic elements on top of the opposite side (d), the silicon is partially etched from the window aperture, generating a free standing membrane layer with the metallic components (e). More details can be found elsewhere[64].

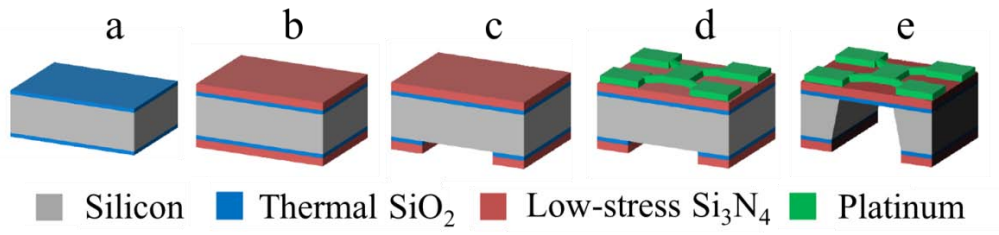

Figure 14. Microfabrication steps performed in order to build a calorimetric cell. A) Thermal oxidation of the silicon wafer. B) Growth of low-stress silicon nitride layers. C) Opening of a window in the silicon nitride and silicon oxide layers. D) Growth of metallic components. E) Etching of silicon and release of silicon nitride membrane.

3.3.3.2 Principle of operation

The operation of the nanocalorimetric device is based on the simultaneous injection of intensity into the metallic heater and the measurement of the produced voltage drop. The injection of current in the platinum serpentine produces an increase of the temperature due to the Joule effect. In order to measure the voltage drop from one extreme to the other of the metallic serpentine, two extra contacts are used, defining a 4-probe measurement scheme: two contacts to inject current into the serpentine and two contacts to measure the voltage drop across the sensing area of the device. These two magnitudes – injected current and voltage drop – define the fundamental quantities from which the heat capacity measurement is derived. In particular, from these two magnitudes, the injected power to the calorimetric cell is defined as $P = V \cdot I$, and the resistance of the metallic serpentine in the sensing area is $R = \frac{V}{I}$. From the resistance of the serpentine, the temperature of the sensing area can be inferred using a calibration curve (see section 3.3.3.4).

The fundamental peculiarity of fast-scanning quasi-adiabatic nanocalorimetry is the injection of relatively high intensity pulses during a time lapse of the order of the millisecond (typically 40 mA and 4 milliseconds in this work). This will induce a linear increase of the temperature and, therefore, constant heating rates in the sensing area of the calorimetric cell of around $5 \cdot 10^4$ K/s.

These fast heating rates, together with the low thermal conductance of the cell membrane will avoid the conduction of heat from the sensing area to its surroundings (rest of membrane and silicon frame) during the timeframe of the measurement. On the other hand, if the temperatures reached during the scan are relatively low (not higher than 500 K) thermal losses by thermal radiation are minor. Considering that the nanocalorimetry measurements are performed in ultra-high vacuum conditions, we can assume that the experiments are performed under adiabatic conditions, which is the basis of the subsequent data analysis for this technique.

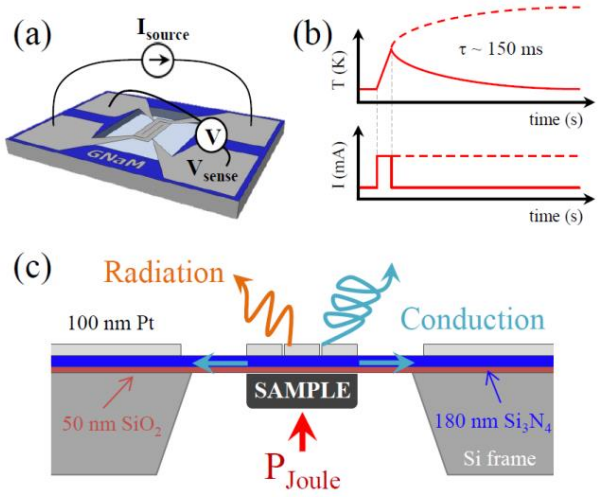

Figure 15. Sketch of the principle of operation of the calorimetric cell. A) Basically, the measurement process consists on the injection of intensity and the subsequent measurement of the induced voltage drop. B) Typical temperature temporal profile induced by the square intensity pulse. During the initial stage of the pulse (few milliseconds) a linear heating rate is induced. After that time, the temperature temporal profile is no longer linear. Therefore, long pulses are avoided. Once the pulse is ended, the calorimetric cell is passively cooled down. C) Possible heat losses that may occur in the cell. Both radiation and conduction are avoided due to the experimental conditions of the measurement process.

The temperature homogeneity of the sensing area during the calorimetric scan is also an important issue. At each time, a unique value of temperature is assigned to the sensing area. If the temperature profile is not sufficiently uniform, incorrect temperature values may be wrongly assigned to a specific thermal process. The use of fast heating rates permits also the generation of more homogeneous temperature profiles (Figure 16). At isothermal conditions temperature profiles are considerably large. During a scan at typical heating rates, around 10^5 K/s, the low lateral heat diffusion of the silicon nitride membrane avoids the power dissipation and, therefore, the temperature gradient is considerably smaller, although certain gradient is always present. In order to further homogenize the temperature profile, it is necessary to grow a thermal plate on top of the membrane, even at expenses of increasing the specific heat of the device and, therefore,

reducing the sensitivity. In figure 17, a comparison between the temperature profile of two cells, one with a 200 nm plate of aluminium and one with a 20 nm plate is shown. As can be seen in the same figure, the existence of a particular temperature gradient clearly affects the shape of the calorimetric transition and the onset temperature of a given reaction.

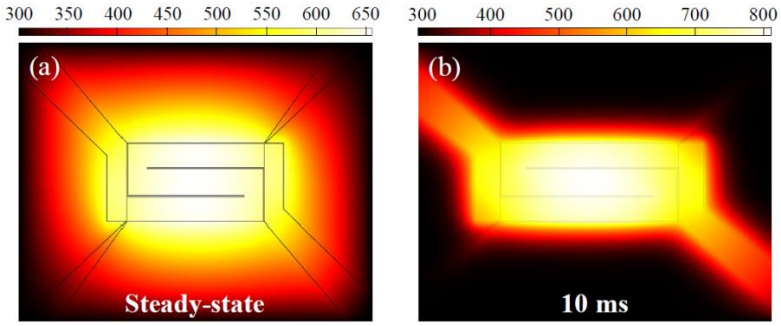

Figure 16. COMSOL© simulation of a temperature profile in a calorimetric cell in a) steady-state conditions and b) after a 10 millisecond pulse[65].

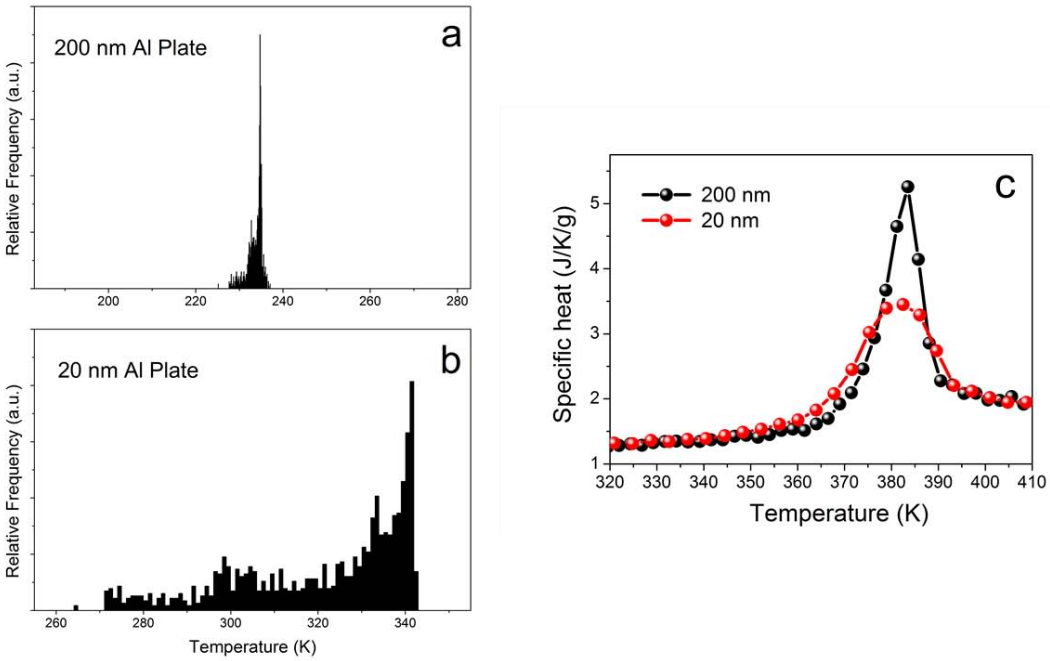

Figure 17 Comparison between two temperature profiles measured in two calorimetric cells, one with a 200 nm aluminium plate and one cell with a 20 nm plate. a) and b) show the histograms of temperature distribution during a micro pulse of 35 mA for 2 milliseconds, as reproduced by a COMSOL simulation. Relative frequency refers to the number of small areas, in which the whole area is divided, that have a particular value of temperature. c) Specific heat curves obtained for the same sample but using different plates.

Measuring using a differential configuration allows the enhancement of the sensitivity. The use of a couple of twin calorimetric cells (ideally with the same heat capacity and temperature-resistance relationship) permits, basically, to amplify the calorimetric signal generated by the sample, excluding from the amplification the information coming from the surroundings. While a measurement performed on a single device could be amplified by a factor of around 3 without saturating the acquisition card (maximum acquisition voltage of 10 V), the differential signal can be amplified up to 500 times.

New commercial setups based on fast-scanning calorimetry on membrane-based microchips have been recently developed. However, the versatility and superior sensitivity of our home-made calorimetric systems permit us to focus on a variety of studies that cannot be covered yet by the commercial systems.

3.3.3.4 Calibration procedure

As commented previously, the platinum serpentine acts both as a heater and as a thermometer. When the current pulse is injected into the platinum serpentine, it will be heated and its temperature will rise, approximately at a linear pace. By measuring the voltage drop at the serpentine at each moment, the resistance and therefore the temperature of the sensing area can be calculated. With that objective, it is necessary to know the exact relationship between the resistance of the metallic layer and its temperature. The choice of platinum as heater/sensor material responds to that requirement. The dependence of its resistance with temperature is, across a very wide temperature range, almost linear. Only small quadratic deviances are produced in an extended high temperature range. In particular, in this work we consider that the dependence is quadratic, $R = R_0(1 + AT + BT^2)$, which is strictly valid only in the temperature range from 0 to 800ºC.

In order to evaluate this specific relationship, it is necessary to measure, for different temperatures, the resistance of the calorimetric cells. There are two basic procedures to reliably measure the temperature-resistance relationship of the calorimetric cells: dynamic and static methods. The dynamic mode consists on the calorimetric measurement of given reactions, whose onset temperatures are perfectly known. By assigning the resulting value of the device resistance to the temperature of the process, the relationship can be built. One of the drawbacks of this method is the need of different samples that present a well-known reaction in the temperature range of interest. Most of these reactions depend on the size of the sample. Furthermore, the heating rate influences on the temperature profile of the calorimeter, as previously commented, which oblige to perform the calibration measurement at the same exact conditions that the final

measurement, which turns to be considerably unpractical. Also, it is a requirement that the calibrating substance could be removed after the calibration process. These difficulties prevent the use of this methodology in this work. Static calibration, on the other hand, is performed by setting a particular temperature on the temperature stage, where the calorimeters are located. The resistances of both devices, sample and reference, are measured at each temperature, in a range from 200 K to 400 K, in steps of approximately 20 K. The measurement of the resistance is not trivial, since the self-heating of the thin platinum sensor must be avoided. Taking advantage of the calorimetric device, low intensity pulses (5 mA) of long duration (5 ms) are performed on the calorimetric cells at a certain number of imposed temperatures. Several consecutives scans are averaged in order to increase the resolution. During the course of the pulse, the device is slightly heated. Therefore, an extrapolation of the voltage data must be done to obtain the value corresponding to t = 0 s, when no self-heating is produced. This voltage value is used to calculate the resistance of the device at each temperature, since the value of the injected current is perfectly known. We note that the thermal degradation of the devices induces changes in the physical morphology of the platinum sensor and heater, which implies a change in the temperature-resistance relationship. This fact imposes the systematic recalibration of the devices after certain work load.

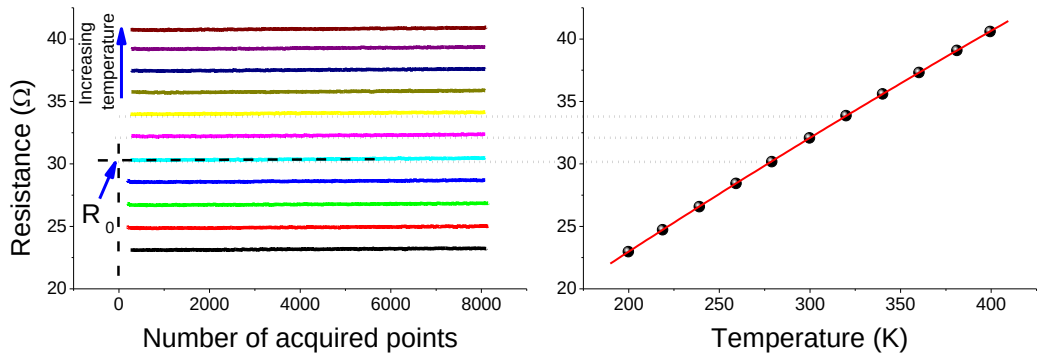

Figure 18. a) Resistance of the device during the current pulse at different temperatures. Resistance values are obtained performing several 5 mA current pulses of 5 ms each. From the averaged measurement of the resistance, an extrapolation to t = 0 s is performed in order to find the value of resistance when no self-heating has been produced. b) This methodology is repeated at different temperatures, which are set using the measurement socket. The R-T curve is calculated by a quadratic fitting of the measured values of resistance vs temperature.

3.3.3.5 Derivation of heat capacity

The output data from a nanocalorimetry measurement is the voltage drop across each of the calorimetric devices, induced after the injection of a short pulse. Under adiabatic conditions, the relationship between input power, $P = V \cdot I$, and heat capacity is given by

$$C_p(T)dT = V(t)I(t)dt = P(t)dt \tag{12}$$

For each of the calorimetric cells, the heat capacity can be expressed as a function of the measured parameters V and I

$$C_p\big(T(t)\big) = \frac{V(t)I(t)}{\beta(t)} \tag{13}$$

where $\beta(t) = \frac{dT(R)}{dt}$, being T(R) the T-R relationship previously found by calibration.

In a non-differential measurement, i.e. the measurement performed with single calorimetric cells, the derivation of the heat capacity of the sample is basically the subtraction of the heat capacity of the empty calorimeter to that of the calorimeter plus the sample deposited on it,

$$C_{p,sample}\big(T(t)\big) = \frac{V(t)I(t)}{\beta(t)} - \frac{V_0(t)I_0(t)}{\beta_0(t)} \tag{14}$$

where the symbols with the subscript 0 refer to the measurement of an empty cell.

As commented previously, the calorimetric signal coming from one single calorimeter is too big to be amplified and subsequently acquired by an acquisition card. Therefore, the heat capacity of the sample obtained following this method is remarkably noisy and it is only useful when considering samples with large mass (i.e. large thicknesses). A differential method is preferred when dealing with small samples, given the possibility to enormously amplify the signal corresponding to the difference in voltage drop between two almost-identical calorimetric cells, rather than the signal corresponding to a single cell.

The difference in heat capacity between both cells (sample and reference) can be expressed as

$$\Delta C_p\big(T(t)\big) = \frac{V_S(t)I(t)}{\beta_S(t)} - \frac{V_R(t)I(t)}{\beta_R(t)} = \frac{V_R(t)I(t)}{\beta_R(t)}\left[\frac{\beta_R(t)}{\beta_S(t)}\left(\frac{\Delta V(t)}{V_R(t)} + 1\right) - 1\right] \tag{15}$$

This expression, although including the term $\Delta V(t)$, which can be heavily amplified, results in a noisy signal. The reason for that is the term $\frac{\beta_R(t)}{\beta_S(t)}$ in the expression.

Therefore, a strategy to obtain reliable signal with low noise levels consists on substituting the term $\frac{\beta_R(t)}{\beta_S(t)}$ for an indirect calculation, using measured parameters. More details on this approach

can be found elsewhere[65]. Basically, it consists on developing the term $\frac{d\Delta V}{dt}$ in order to obtain an alternative expression for $\frac{\beta_R(t)}{\beta_S(t)}$,

$$\frac{d\Delta V}{dt} = \frac{dV_S}{dT_S}\beta_S - \frac{dV_R}{dT_R}\beta_R \rightarrow \frac{\beta_S}{\beta_R} = \frac{\left(\frac{d\Delta V}{dt}\right)_t}{\beta_R\left(\frac{dV_S}{dT_S}\right)_t} + \frac{\left(\frac{dV_R}{dT_R}\right)_t}{\left(\frac{dV_S}{dT_S}\right)_t} \tag{16}$$

This new term, much less noisy since it does not contain the heating rate in the numerator, can be calculated from information obtained during the calorimetric measurement. Introducing it in the equation of $\Delta C_p(T(t))$, the following expression is obtained.

$$\Delta C_p(T(t)) = \frac{I_S \Delta V}{\beta_S} + \frac{V_R I_S}{\beta_S}\left[1 - \frac{I_R}{I_S}\left(\frac{\left(\frac{d\Delta V}{dt}\right)_t}{\beta_R\left(\frac{dV_S}{dT_S}\right)_t} + \frac{\left(\frac{dV_R}{dT_R}\right)_t}{\left(\frac{dV_S}{dT_S}\right)_t}\right)\right] \tag{17}$$

This is a general calculation, developed without any assumption or simplification. In the case of this work, some assumptions can be safely made. First, since the current intensity injected in both calorimeters is constant, then the terms $\frac{dV}{dT}$ can be rewritten as $I\frac{dR}{dT}$, which can be directly calculated from the calibration curve. Second, if both calorimeters are fed in series, then $I_S = I_R$. With these particularities, the difference between both heat capacities is expressed as,

$$\Delta C_p(T(t)) = \frac{I\Delta V}{\beta_S} + \frac{V_R}{\beta_S\beta_R}\left[\frac{\left(\frac{d\Delta V}{dt}\right)_t}{\left(\frac{dR_S}{dT_S}\right)_t}\right] + \frac{V_R I}{\beta_S}\left[1 - \frac{\left(\frac{dR_R}{dT_R}\right)_t}{\left(\frac{dR_S}{dT_S}\right)_t}\right] \tag{18}$$

All these expressions for $\Delta C_p(T(t))$ refer to the difference in heat capacity between the loaded calorimetric cell and the reference cell, which equals the heat capacity of the sample only if the heat capacity of both cells are exactly the same. Although the calorimetric cells are previously selected in order to be very similar, it is highly improbable that this requirement is fulfilled. Therefore, a previous measurement, with both cells empty, must be performed in order to subtract from the subsequent measurement (with sample cell loaded) the variation corresponding to the difference in the heat capacity of the cells. This is called "baseline correction". When subtracting the difference in heat capacity with the loaded calorimetric cell, $\Delta C_p(T(t))$, to that of the empty cells, $\Delta C_p^0(T(t))$, the information coming from the sample cell at a given time does not correspond to the same temperature in both measurements, given the difference in mass and, therefore, in heating rate between the loaded and the empty experiments. Using the temperature evolution of the reference calorimetric cell, which is not affected by changes in mass, as a reference, the difference in heat capacity originated by the different heating rates between loaded and empty experiments can be calculated. The heat capacity of the sample, whatever the followed approach is, can be expressed as

$$C_{p,sample}(T) = \Delta C_p(T(t)) - \Delta C_p^0\big(T(t)\big) - \Delta C_p^{beta}(T(t)) \quad (19)$$

In the case of a reversible process, such as the baseline measurement or reversible processes, multiple scans can be performed and subsequently averaged, in order to further reduce the noise level by the square root of the number of measurements

In order to calculate the specific heat of the sample, we need to determine first the value of its mass. Along this thesis the mass of the sample is obtained by dividing the heat capacity measured above the glass transition by the reported value of the specific heat of the supercooled liquid[56,57]. It is important to take into account that, once the sample is in the liquid state, evaporation of the sample can start to influence the measured heat capacity. The chosen heat capacity range used to obtain the mass of the sample must not contain any contribution from evaporation.

3.3.4 Non-adiabatic scanning nanocalorimetry

The use of nanocalorimetry techniques at variable heating rates is interesting given the high resolution and the possibility of performing in-situ measurements, even though the measurement is not always in adiabatic conditions. In those cases, we can only extract information about temperatures of reaction (onset and peak maximum). The exact heat capacity of the sample cannot be extracted without specific methodologies which are out of the reach of this work.

The measurement protocol, in these cases, consists on feeding the device with a current (or power) that responds to a particular profile with respect to time (Figure 19). In this way, an almost constant heating rate is achieved even during considerably long times (up to few seconds). The induced heating rate can be tuned by varying the magnitude of the intensity and the duration of the current profile. The same power profile can be imposed during the cooling down of the sample, in order to obtain particular cooling rates, which will determine the stability of the produced glass.

In the case of non-adiabatic nanocalorimetry measurements, the mathematical derivation of apparent heat capacity from the raw data is analogous to that of the quasi-adiabatic configuration. Given the non-constancy of the feeding intensity, some applied assumptions are no longer valid and, therefore, equation 14 must be used instead of 18. In any case, since the obtained data does not correspond to the real heat capacity of the sample, it is not possible, without the use of complex models, to obtain data concerning thermodynamic stability of the glass or the mass of the sample.

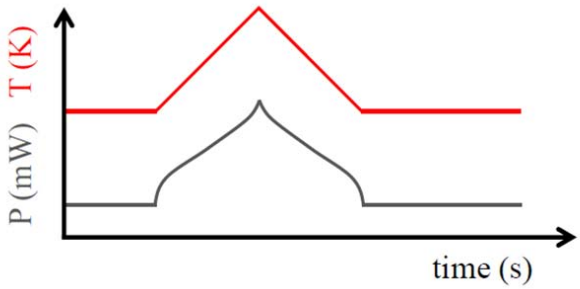

Figure 19. Temporal profile of power (grey) and induced temperature (red). Constant heating rates can be achieved using Saw-Tooth nanocalorimetry[64,65] even during relatively long times (up to few seconds) thanks to the particular shape of the power input.

3.4 Experimental setup

In Figure 20 a scheme of the experimental setup is shown. Although most of the elements are fixed, the particular choice of the distribution of some elements depends on the process that must be carried out and the subsequent type of characterization. The elements that will determine the specific configuration of the systems are i) the size of the sample (thickness and area) and ii) the type of characterization technique to be performed (in-situ or ex-situ).

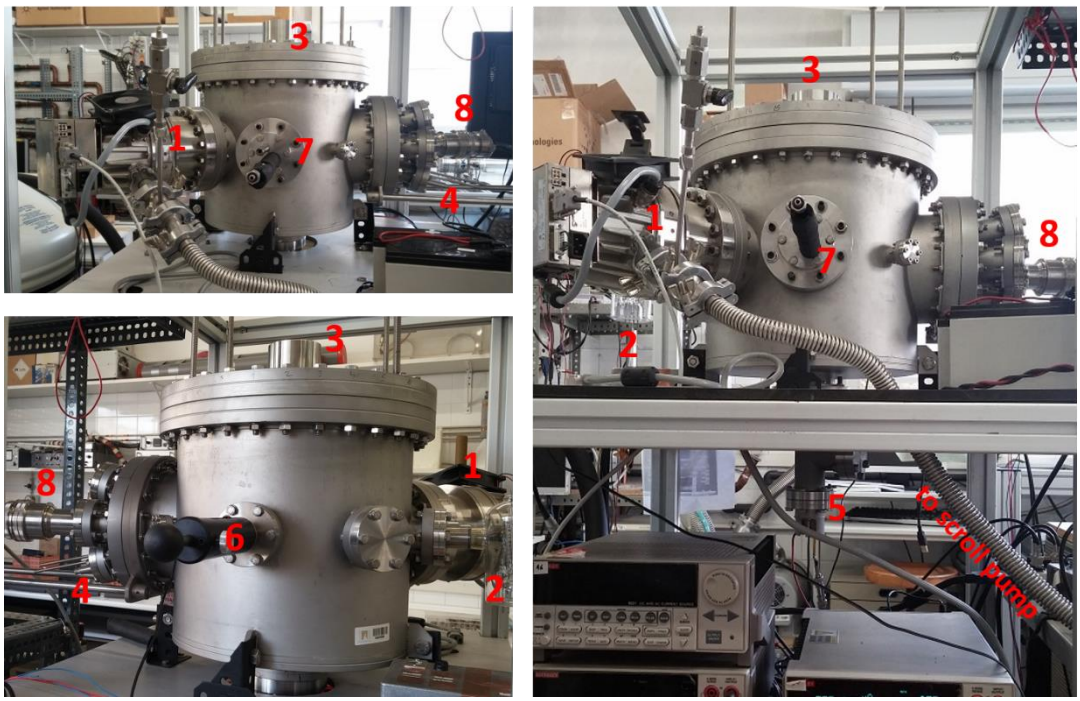

Figure 20. Photographs of the experimental vacuum chamber, where the growth and some characterization processes are performed. 1) Turbomolecular pump. 2) Vacuum gauge. 3) Nitrogen cold-trap. 4) Rate monitor feedthrough. 5) Effusion cell. 6) Shutter feedthrough. 7) Sample holder arm. 8) Electrical feedthrough.

A Varian Turbo-V 301 Navigator turbomolecular pump (number 1 in Figure 20) is directly connected to a side port of the chamber, with a protective shield in its inlet, in order to avoid the possible collision with a big element. The turbo pump is connected, from its outlet, to a dry scroll pump Varian SX110 (not shown). The Bayard-Alpert vacuum sensor (2) is connected to the port next to the turbo pump. A nitrogen cold trap is installed in the upper port of the chamber (3).

From another lateral port, there is SYCON quartz-crystal thickness microbalance installed (Figure 20, number 4). Two thin liquid feedthroughs are used as mechanical support for the sensor head, where the crystal is placed. No refrigeration of the monitor head is required, as the working temperatures are relatively low. The head is placed close to the sample socket and at approximately the same height. However, even being the sensor close to the sample, a proper calibration must be performed, since the position of the sensor strongly influences the registered value for the evaporation rate. With that aim, a sample of a given thickness is grown and its thickness is externally measured by means of a conventional profilometer. An electrical feedthrough is used to connect the head of the sensor with the outside, where it is connected to an oscillator and a controller. The controller is then connected to a computer, where Labview software is used to obtain the final rate reading.

Below the chamber, we have installed a CREATEC low temperature effusion cell with a stainless steel crucible with a maximum load capacity of 35 cc (5). The position of the mouth of the cell will determine, for a given effusion cell temperature, the evaporation rate. When thick layers need to be produced, the cell is placed closer to the substrate, in order to save material. In order to adjust the vertical position of the effusion cell we use adaptors with different lengths. A power source Agilent E3642A feeds the thermal heater of the cell, giving a maximum of 5 amps and/or 8 V. A K-type thermocouple is used to measure the temperature of the cell.

Through another port we have installed a linear movement feedthrough (6). To the extreme of its shaft, a shutter blade is attached. The shutter blade moves at a height level just below the socket. The aim of the shutter is to protect the sample while the evaporation rate stabilizes. The longitudinal maximum walk of the feedthrough is 5 cm. This is, therefore, the maximum length that the shutter can cover. If longer substrates are used, part of it will remain either permanently hidden or permanently exposed. Therefore, in this later situation, the shutter blade is positioned so as to cover the evaporation source, instead of hiding the substrate. Unfortunately, in this case no material will arrive to the substrate, but neither to the quartz microbalance and, therefore, the evaporation rate cannot be checked before exposing the substrate to the evaporation source.

A holder-arm is introduced through a lateral port of the chamber (7). This piece consists on a liquid feedthrough, with a copper block attached to the extreme (figure 21). The arm acts both as a physical holder, places the sample in the centre of the chamber, as well as cooling system. A

base temperature can be set by making liquid nitrogen or refrigerant liquid circulate into the circuit and inside the copper block. The election of a specific base temperature depends on the material under study and the process to be carried out. Different sample sockets can be attached to the copper block, depending on the characterization technique to be used. All electrical connection to the outside of the chamber are stablished through an electrical feedthrough (8).

It is important to recall that the thermal contact between the copper block and any socket attached to it depends on the working temperature and on the source of refrigeration. If the thermal contact is too strong, and the base temperature is too low (for example, when using liquid nitrogen) a high power must be used in order to set a particular working temperature. For example, when performing nanocalorimetry measurements, the working temperature is set to 200 K. In this case, the base temperature of the copper block is 76 K (temperature of liquid nitrogen at ambient pressure). A strong thermal link between copper block and socket will not let the measurement socket to be heated enough. The contact between copper block and measurement socket is generally established by two nuts placed at each extreme of the socket.

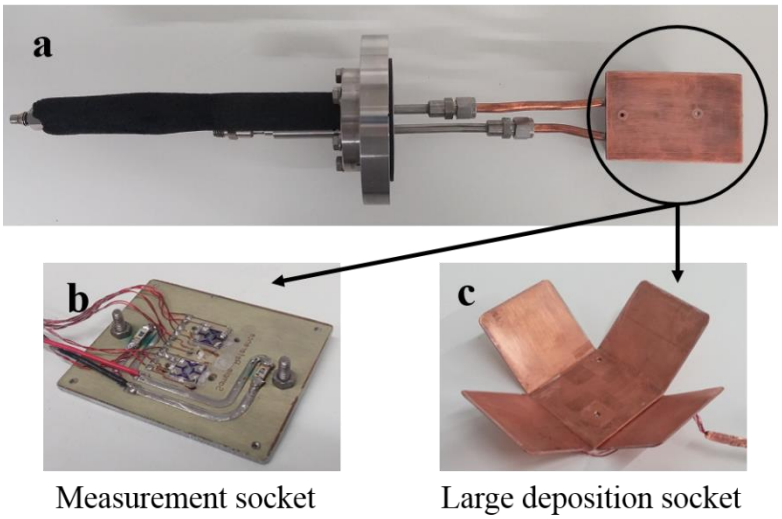

Figure 21. Image of the substrate holder arm, a, together with the attachable accessories designed to perform different experiments. In the case of nanocalorimetry measures or deposition of small samples, the measurement socket, b, is attached to the copper block of the holder arm. In the case of multiple substrate evaporation, the large deposition socket, c, is attached to the copper block, in order to obtain homogeneous samples across a larger area.

3.4.1 Setup for nanocalorimetric measurement

The two calorimetric cells are placed on a measuring socket and inside the vacuum chamber, occupying the position of the substrate. The socket is fabricated from a thermal clad plate. The

plate consists of three layers: a thick aluminium plate (around 1.8 mm), an intermediate insulator layer and a copper thin layer. When acquired, the copper layer is covered with photo-resist. By means of conventional photolithography techniques, the electric motives are translated and etched into the copper layer. Once fabricated, the socket is equipped, apart from the calorimetric cells, with two heaters and a PT100 thermal resistance sensor, according to the distribution shown in figure 22. The evaporated molecules will arrive to the surface of the cell through a hole made in the socket just below the cell. The heater resistances, 100 ohms each and connected in parallel, will permit the setting of a base temperature. The PT100 sensor, connected in a 4-point probe configuration, permits the measurement of the temperature of the socket at every moment.

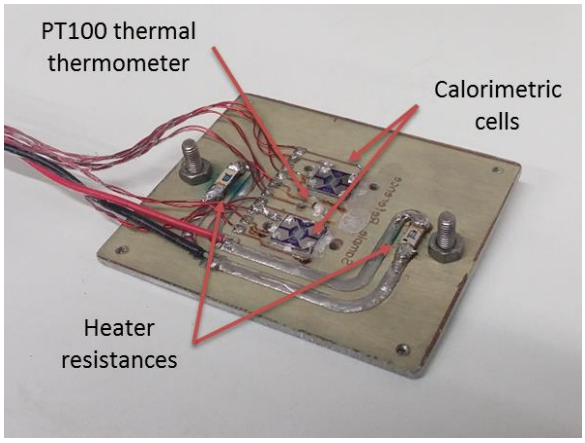

Figure 22 Image of the measurement socket. The socket itself is made from a thermal clad plate, on which the necessary circuits have been built by means of photolithography techniques. On that socket, two almost identical calorimetric cells are installed with the deposition side looking downwards. Under the sample calorimetric cell, a hole is made in order to permit the sample deposition. Apart from the cells, a couple of heating resistances and a PT100 thermal resistor are installed, in order to register the base temperature of the socket at each moment. The socket is attached to the sample holder arm by means of two steel screws (Figure 21).

The two calorimeter cells are, on one hand, connected in series to a power supply Keithley 2400, able to produce very short current pulses with a constant intensity (typically 40 mA). On the other hand, the devices are connected (via 4-point probe configuration) to an operational box, with an INA110 amplifier device and a variable resistance set to conveniently tune the amplification factor and, afterwards, to an acquisition card. Home-made Labview software controls the power supply and acquisition card, in order to obtain the raw data (voltage) from each measurement. The sketch of the instrumentation setup is represented in Figure 23.

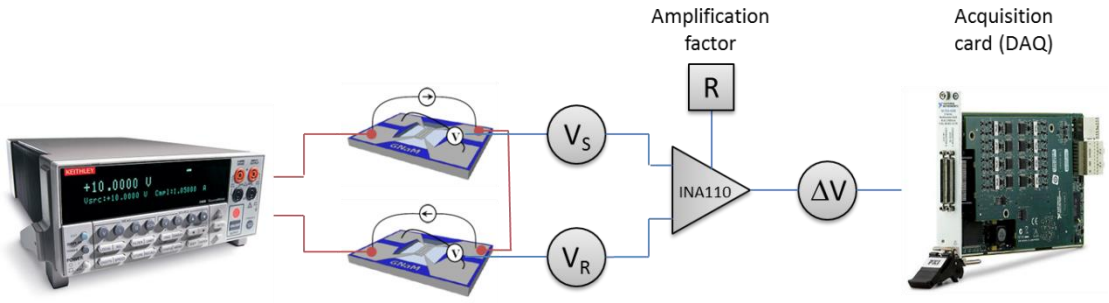

Figure 23. Sketch of the instrumentation setup, as indicated in the text. Basically, a 2400 Keithley power source feeds the two almost-identical cells by means of very short micro-pulses (typically 40 mA, 4 ms). The response of the devices is measured by means of the voltage drop on each of them, which is amplified (up to 500x, depending on the set amplification factor) and acquired by the DAQ.

3.4.2 Setup for ex-situ experiments

If ex-situ measurements are performed, the substrate is placed on the same socket used to perform nanocalorimetry in-situ measurements. If DSC or other ex-situ calorimetry measurements have to be performed, the sample is deposited onto an aluminium foil attached to the measurement socket. In the case of other characterization techniques, conventional silicon substrates are used.

When many samples must be produced at the same evaporation conditions, a special nearly-spherical substrate holder is attached to the copper block at the end of the holder-arm (figure 23a). The socket has been designed to guarantee the maximum homogeneity of all deposited samples, according to the cosine law of evaporation (see section 3.2.2).

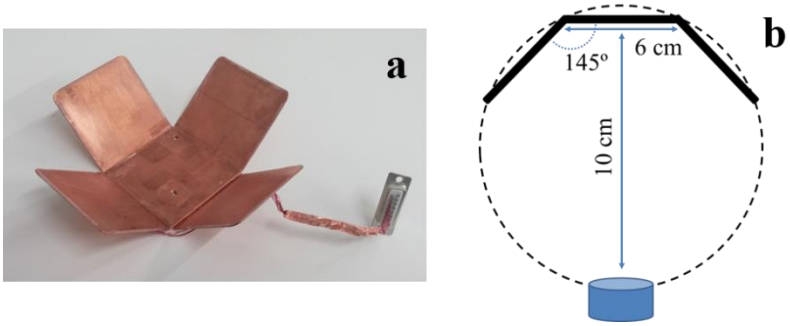

Figure 24. a) Sample holder used in case of multiple-substrate evaporations, which is attached to the holder arm shown in Figure 21a. It is equipped with a PT100 resistance sensor in order to read the temperature of the piece. b) Schema of the design of the sample holder shown in a. In order to produce more homogeneous samples, the surface of the holder should fall on the surface of the Knudsen sphere defined by the distance between evaporation source and substrate surface.

3.6 Materials

Three different organic materials have been used in this work. Most of the experiments have been performed with Indomethacin, an organic compound used and commercialized as an anti-inflammatory drug. It was acquired in the crystalline phase from Sigma-Aldrich with purity higher than 99%, and was used without further treatment. Its melting point is located around 430 K. The second organic material used in this work is Celecoxib, also an anti-inflammatory drug widely used by the pharmaceutical industry. It has a melting point around 420 K. It was obtained from Haihang Industry in China with a purity of 98 % and was used without further treatment. Some reported experiments were carried out with Toluene, a highly used organic dissolvent. It was acquired in the liquid phase from Sigma-Aldrich with purity higher than 99%. Details concerning the experimental details of toluene glass preparation can be found elsewhere[66,67]. Figure 25 shows the molecule scheme of the three compounds used in this work.

Thin film samples have been prepared by physical vapour deposition at a base pressure of $3 \cdot 10^{-8}$ The films have been grown at a deposition rate of 0.1-0.2 nm/s and substrate temperatures between $0.65T_g$ and $0.95T_g$, being T_g the glass transition temperature of a conventional glass of each type of material ($T_{g,IMC}$ = 315 K; $T_{g,CXIB}$=326 K; $T_{g,TOL}$= 117 K). Different substrates have been used depending on the experiments to be performed after the deposition. For nanocalorimetry measurements the films have been deposited directly on the nanocalorimeter membrane. An aluminium foil has been used as a substrate for conventional DSC measurements. In the case of high-pressure calorimetry, we have used small pieces of a monocrystalline silicon wafer.

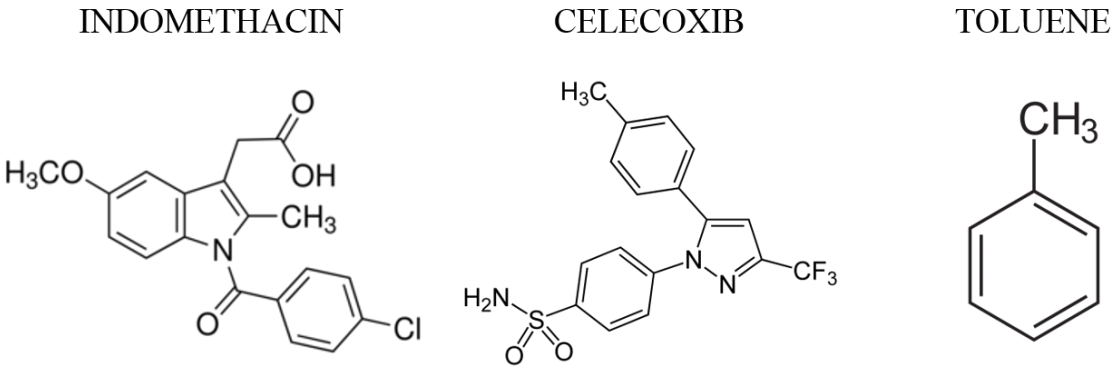

Figure 25. Representation of the chemical structure of the molecules studied in this work: Indomethacin (IMC), celecoxib (CXIB) and toluene (TOL).

4. TRANSFORMATION MECHANISM OF VAPOUR DEPOSITED GLASSES

Part of this Chapter appears published in The Journal of Physical Chemistry B. 2014, 118 (36), pp. 10795-10801 and in Phys. Chem. Chem. Phys., 2015, 17, 31195-31201.

4.1 Chapter introduction

Traditionally, very stable glasses are obtained either by reducing the cooling rate, though this methodology is limited by the crystallization, or by aging the glass at temperatures below the glass transition temperature, a very slow kinetical process. In addition, crystallization can be activated if Johari-Goldstein relaxation mechanisms, a particular beta relaxation process[68], are active at the aging temperature[69]. As thoroughly explained in Chapter 2, very recently, a new methodology to prepare highly stable glasses has emerged and now it is well consolidated within the scientific community[37,70] This methodology employs physical vapour deposition at deposition temperatures slightly below the conventional glass transition temperature, $T_{dep} = 0.8 – 0.9T_g$, as a route to obtain thin film glasses with a remarkable enhancement of their kinetic and thermodynamic stability. Glasses grown at these conditions rival in stability with natural ambers aged during millions of years[71]. This behaviour was initially observed for 1,3-bis-(1-naphthyl)-5-(2-naphthyl)benzene (TNB)[37] and indomethacin[70], but later on it has been corroborated for many other organic molecules such as toluene and ethylbenzene[66], N,N′-bis(3-methylphenyl)-N,N′-diphenylbenzidine (TPD)[72] or even mixtures of cis/trans-Decalin[73], in what seems to be a general trend for organic molecules[74]. This methodology has been successfully extended to produce highly stable polymers[75] and metallic glasses[76,77].

Besides the enhancement of thermodynamic and kinetic stability, vapour-deposited ultrastable glasses exhibit other remarkable properties when compared to the conventional glass, such as higher density, lower thermal expansion coefficient, a growth front transformation mechanism into the liquid that initiates at free surfaces or the existence of molecular anisotropy that produces a low-q extra peak in X-ray diffraction patterns and birefringence in ellipsometry experiments[42,47–50,55].

Experiments and glass theories have always led to conclude that conventional glasses transform into de supercooled liquid state by a homogenous process that occurs throughout the volume of the sample[12,78]. On the other hand, in the case of ultrastable glasses, the increased density and

tight molecular packing have been proposed as the causes for the transformation to start at regions where the mobility is higher, i.e., surface and interfaces. A propagation front has been directly identified by secondary ion mass spectrometry[52,79] and indirectly by dielectric relaxation[51], AC nanocalorimetry[43] and ellipsometry[72,80]. These experiments demonstrated the existence of growth fronts parallel to the surface and were able to determine the temperature dependence of the growth front velocity in a reduced temperature range. In highly stable glasses of IMC, bulk transformation dominates the conversion into the liquid for thicknesses above 1 micrometre, whereas the heterogeneous surface-initiated mechanism dominates at smaller thicknesses[43], as depicted in Figure 26. These data are consistent with several models and theories that have been developed to explain this striking behaviour. In the framework of the first order transition theory (RFOT)[81], the transformation of a glass into a liquid can be governed by homogeneous and heterogeneous mechanisms in agreement with experimental observations. According to this theory, the speed of the propagating front is directly related to the mobility of the supercooled liquid behind the front. Furthermore, Leonard and Harrowell used a facilitated Ising model to show, in agreement with experimental observations, that, for slightly stable films, the temperature dependence of the front propagation is mainly determined by the relaxation time of the liquid[82].

One of the advantages of physical vapour deposition is the possibility to tailor the deposition conditions to prepare glasses of very different stabilities, spanning in limiting fictive temperature by 50 K or 22 J/g in energy, values not accessible for glasses prepared from the liquid. Glasses of TPD and IMC were deposited by Dalal et al. in a multi-temperature stage and measured by ellipsometry close to ambient temperature[42,49]. These authors found that glasses of different stabilities had the same temperature dependence, at least for the analysed temperature range. Both RFOT and pinning models foresee a strong temperature dependence of the growth front velocity and a small influence of stability[83,84].

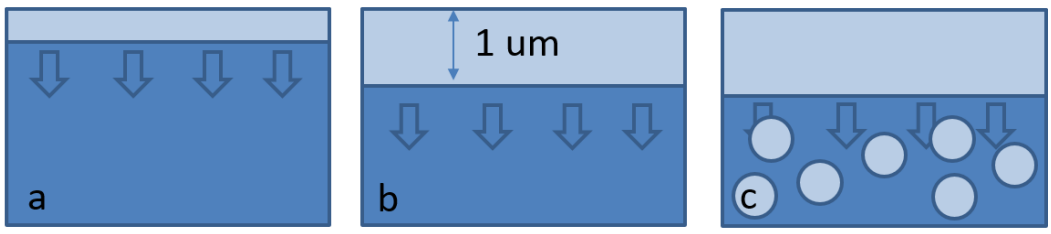

Figure 26. Schema of the transformation mechanism in stable glasses. At the beginning of the process, a front initiates from the surface (and/or interfaces) and propagates into de bulk (a). In ultrastable glasses, the front penetrates approximately 1 micrometre into the bulk (b), before the homogeneous bulk transformation is triggered and dominates from that moment the transformation process (c).

4.2 Kinetic and thermodynamic stability of vapour deposited glasses

First of all, we analyse the dependence of stability on deposition temperature by preparing samples of indomethacin at temperatures ranging from $0.63T_g$ to T_g ($T_{g,IMC}$ = 315 K). Figure 27 shows the specific heat curves of 1 to 3 µm thick glasses obtained at different substrate temperatures.

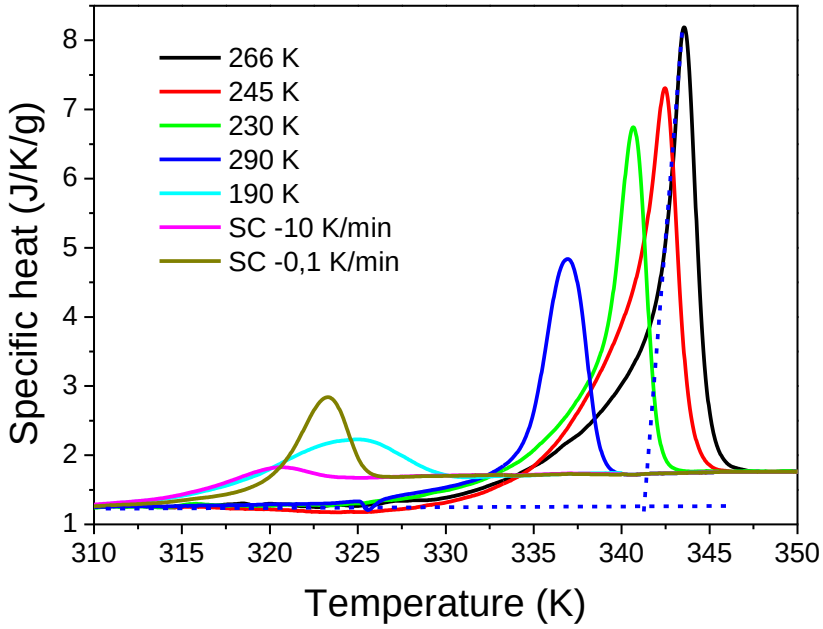

Figure 27. Specific heat curves of glasses of IMC deposited at different deposition temperatures (indicated in the legend) and slowly cooled from the liquid (at -10 K/min and at -0.1 K/min), measured by DSC. The dashed lines indicate the onset temperature of the corresponding glass transition. All measurements have been performed at a heating rate of 10 K/min.

The position and the area of the endothermic peak, corresponding to the devitrification of the glass, change as a function of the deposition temperature. The onset temperature is evaluated by extrapolation of the glass heat capacity and its intersection with the line representing the rise in specific heat, as schematically shown for the sample grown at 266 K (ultrastable) in figure 27. The onset of the devitrification temperature indicates the kinetic stability of the glass and depends not only on the deposition temperature but also on other parameters such as the heating rate or the transformation mechanism. On the other hand, the change in thermodynamic stability as a function of deposition temperature is evaluated by the change in limiting fictive temperature, T'_f. We have used the procedure described by Moynihan et al. to calculate T'_f[85]. Basically, the limiting fictive temperature is determined from the intersection between the enthalpy of the liquid and the

enthalpy of the glass, which are obtained by integrating the specific heat as a function of the temperature, as indicated in figure 6 of Chapter 2.

In Figure 28 we represent the limiting fictive temperature of glasses deposited at different substrate temperatures. As can be seen, glasses of IMC grown at temperatures around $0.85T_g$ have a minimum in T_f', and therefore a maximum in thermodynamic stability. Equivalent results have been obtained for many other organic molecules[37,67,72].

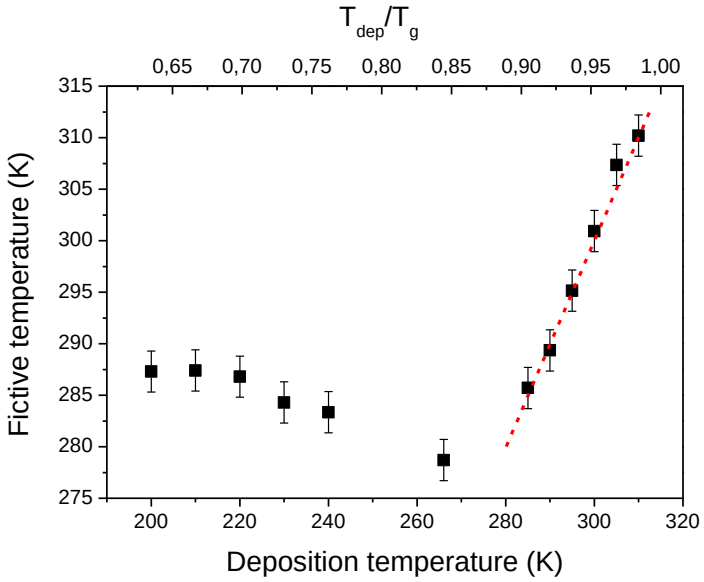

Figure 28. Limiting fictive temperatures of IMC glasses deposited at different substrate temperatures. Clearly, there is a minimum in T_f' for glasses grown around $0.85T_g$, indicating a maximum in thermodynamic stability. The red dotted line corresponds to $T_f' = T_{dep}$.

A maximum difference in limiting fictive temperature of 35 K is obtained by varying the deposition conditions from 266 K to 315 K. At temperatures above 0.9Tg, the limiting fictive temperature coincides with the deposition temperature. In this temperature range, the deposited molecules are in thermodynamic equilibrium with the liquid. The same equivalence between glass and liquid properties has been reported for the density of IMC glasses[42]. For deposition temperatures below 0.8Tg, the low substrate temperature precludes the complete relaxation of the deposited molecules, which get trapped in a particular thermodynamic stability after being buried by the upcoming molecules.

In this work we have used several calorimetric techniques, DSC, Saw-tooth and Quasi-adiabatic fast-scanning nanocalorimetry, in order to span the accessible heating rate range from 0.033K/s up to 10^5 K/s. Due to the kinetic nature of the glass transition, the high heating rates used in the nanocalorimetry scans drive the glass transition to much higher values of temperature compared to conventional DSC data measured at 10 K/min, regardless of the glass stability, as seen in Figure

29. We note that the enthalpic limiting fictive temperature obtained for glasses grown at the same conditions is independent of the imposed heating rate, as can be seen in Figure 30.

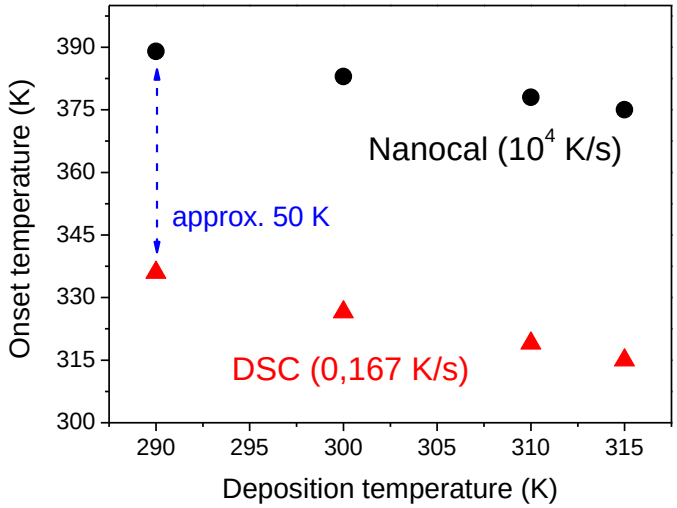

Figure 29. Onset temperature of 1 to 3 μm thick IMC glasses deposited at different temperatures and measured by nanocalorimetry, at 10^4 K/s, and by DSC, at 0.167 K/s.

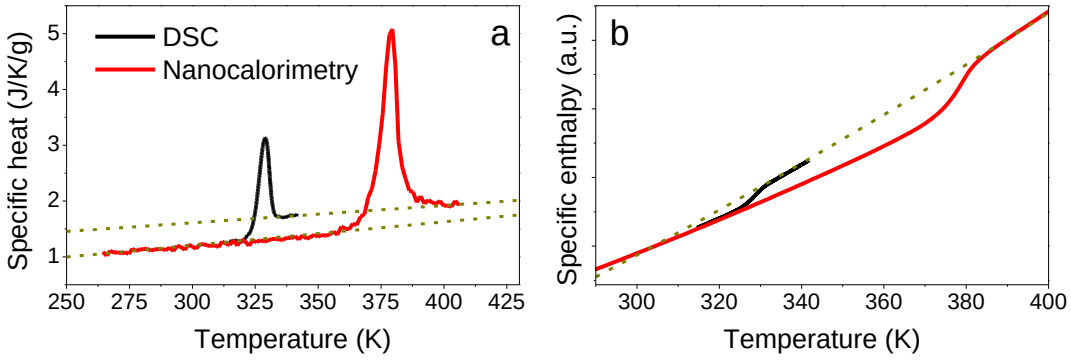

Figure 30. Comparison of limiting fictive temperature of a glass measured at two different heating rates. a) Specific heat capacity of a glass deposited at 300 K measured at 0.167 K/s (black curve) and at $3 \cdot 10^5$ K/s (red curve). Dashed lines correspond to the specific heat of the glass and the liquid. b) Enthalpy curves yielded by the integration of heat capacity shown in a. Although the devitrification temperature is lower when measured at lower heating rates, the different enthalpy of excess compensates the shift and both measurements result in the same value of limiting fictive temperature. The thickness of the sample measured by nanocalorimetry is 100 nm, while the sample measured in the DSC is 1 micrometre thick. A similar result was obtained by Simon et at.[86].

4.3 Heterogeneous transformation mechanism

4.3.1 Identification of growth fronts

The specific heat of a sample is evaluated by dividing the heat capacity curve by the total mass of the sample. Figure 31 shows specific heat curves of ultrastable glasses of indomethacin (grown at 266 K) with thicknesses ranging from 20 nm up to 4 µm. This representation of the data shows a clear shift of the onset of the devitrification temperature depending on the thickness of the film. This result seems counterintuitive, since size effects are not often observed in films of thicknesses above 200 nanometers. We note that mass normalization equally weights the whole sample and it is mainly used for reactions taking place homogeneously throughout all the volume of the sample. However, it is expected that these highly stable glasses convert into liquid via a heterogeneous transformation mechanism with a growth front that originates at the surface of the films and/or at the interface with the substrate[43,51,79]. In that case, a normalization that incorporates the area of the sample should yield a superposition of experimental data, since the fraction of the sample that transforms per unit time is proportional to the surface of the film.

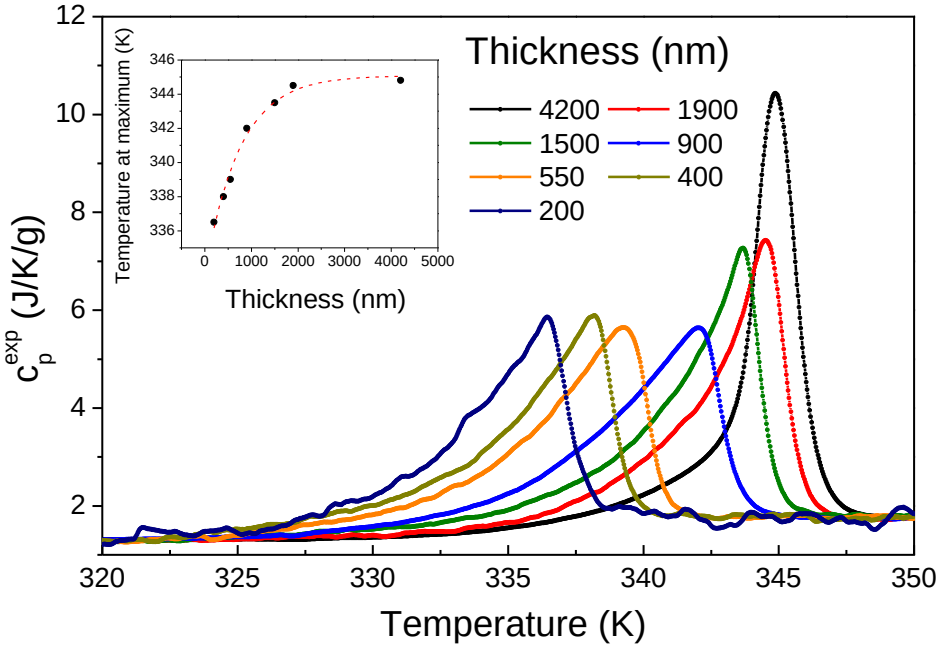

Figure 31. Specific heat of ultrastable thin film glasses of IMC (T_{dep} = 266K) of different thicknesses, obtained by normalizing the heat capacity by the mass of each sample. The inset shows the temperature of the maximum of the devitrification peak as a function of the sample thickness, approaching a constant value. The discontinuous line is a guide for the eye. The thickness of the samples is calculated from the deposited mass and considering a density of 1.32 g/cm^3 [42,45].

In order to carry out a more appropriate normalization procedure we first consider that the experimental heat capacity, $C_p^{exp}(T)$, can be decomposed into three terms: the contributions from the heat capacity of the glass and the liquid and the derivative of the enthalpy of reaction, evaluated at each temperature. Thus, $C_p^{exp}(T)$ can be written as:

$$C_p^{\exp}(T) = m_o\left(c_p^g\left(1 - x_l(T)\right) + c_p^l x_l(T) + \Delta h \frac{d\, x_l(T)}{dT} \right) \tag{20}$$

where c_{pg} and c_{pl} denote, respectively, the specific heat of the glass and the supercooled liquid, m_o is the total mass of the sample, Δh is the specific enthalpy of reaction, and x_l is the fraction of glass that has already transformed into supercooled liquid. x_l is time/temperature dependent and ranges from 0 to 1. If we consider that the transformation into the supercooled liquid occurs exclusively via a parallel growth front, we can rewrite eq. 20 substituting: (a) the total mass by the product $m_o = d_o \cdot A \cdot \rho$, where A is the surface area, ρthe density and d_o is the total thickness of the film, and (b) the transformed fraction by $x_l = d_l/d_o$, where d_l is the thickness of glass that has already transformed into liquid. In order to find a general trend for all samples, we need to remove from the right-hand side of equation 20 the parameters that are not common to all samples, i.e., A and d_o.

$$c_p^{norm}(T) = \frac{C_p^{\exp}(T)}{\rho A} - c_p^g d_o = d_l(T)\left(c_p^l - c_p^g\right) + \Delta h \frac{d\left(d_l(T)\right)}{dT} \tag{21}$$

In this equation, we have considered that the transformation rate is in principle common for all the samples, regardless of their total thickness. Figure 32 shows the calorimetric heat capacity curves after applying the parallel front normalization stated in equation 21.

Figure 32 illustrates that the onsets of the calorimetric traces of the various samples overlap into a single curve for thicknesses below ~900 nm. This superposition confirms that the transformation rate scales with the surface of the film. The temperature variation of the end of the transformation clearly depends on the sample thickness and is compatible with a mechanism where the extent of the transformation is dominated by parallel growth fronts. Figure 32 also reveals that it is not straightforward to define an onset temperature for the glass transition when the transformation mechanism does not consist on a homogenous process.

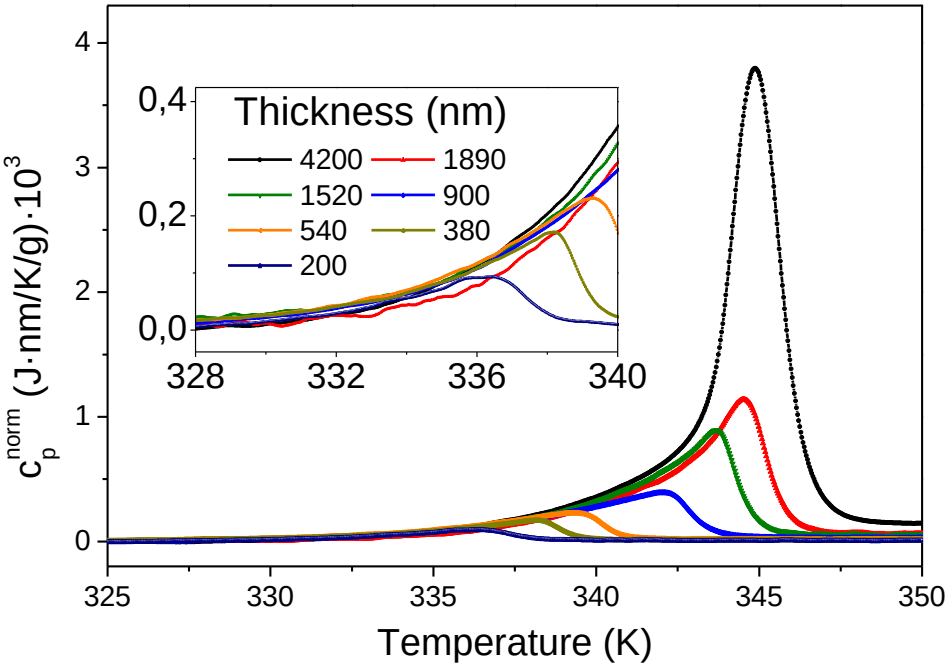

Figure 32. Surface-normalized heat capacity vs temperature highlighting the heterogeneous mechanism of transformation. We observe a superposition of all the curves, regardless of the thickness of the sample, along a certain temperature range, indicating a transformation to the liquid via a front propagation. The inset shows a close-up of the first stages of the transformation into the supercooled liquid, when the growth front dominates.

As stated above, surface normalization provides important information when the predominant transformation mechanism is via a heterogeneous process that starts at surfaces/interfaces, which, in agreement with reported results[43], occurs for thicknesses below 1 µm for ultrastable glasses of indomethacin. Above this film thickness, the bulk transformation is not negligible and the normalization procedure of equation 21 is no longer valid to study the evolution of the transformation front. Indeed, figure 32 shows that the onset of de C_p curves of samples thicker than 1 µm increases faster when the bulk starts to transform and the two mechanisms contribute to the growth of the supercooled liquid. This is due to the fact that, once the bulk transformation mechanism sets in, it dominates and the transformation rate is proportional to the volume of the sample rather than to the surface area. In the case of thicker films, where the homogeneous transformation starts to be predominant, mass normalization is easier to interpret. In these cases, the specific heat curves begin to collapse to a single one, as can be observed in Figure 31 by the asymptotic behaviour of the peak maxima as thickness increases.

We note that the end of the transformation does not stop abruptly, as we would expect in the case of a parallel front transformation. Several explanations are plausible. If the transformation front

is not completely parallel to the surface of the sample, the last stages of transformation would correspond to a variable sample area. On the other hand, a slight temperature inhomogeneity in the sample, produced by the sample preparation procedure, may originate a gradient of transformation rates. In this case, it is important to note that the slope of heat capacity at the end of the transformation is much faster than at the beginning of the peak, what permits us to discard a significant influence of temperature gradients on transformation rate.

We now focus our attention on calorimetric data obtained by quasi-adiabatic fast scanning nanocalorimetry on thinner films, between 20 and 120 nm. Figure 33 demonstrates the impact of the stability of the glass on the transformation mechanism. The mass-normalized specific heat of samples of different thicknesses grown at 0.85 T_g (UG) and obtained from the liquid (fast-cooled, FC) are plotted in parts a) and b) of Figure 33 respectively. The data of Figure 33a reproduce the behaviour observed in the DSC scans; that is, the mass normalization introduces an apparent dependence of the onset temperature on sample thickness. In contrast, normalizing by the surface area produces the collapse of all curves to a common beginning of the transformation, as seen in Figure 33c, which can be explained by a parallel growth front mechanism. In this thickness range and at these heating rates, the propagation of the growth front dominates the transformation of the entire glass into the supercooled liquid. On the other hand, FC glasses, shown in Figure 33 b and d, exhibit the opposite behaviour. Mass normalization produces the collapse of all curves into a single, master curve, irrespective of the thickness of the films, while surface normalization yields curves with different onsets. In FC glasses, the transformation takes place homogeneously in the volume of the sample and the transformed fraction per unit time is independent of the total mass/volume of the film, and therefore of its thickness/surface.

Since the area of the studied samples is a key parameter in the normalization of the heat capacity data, it is fundamental to assure the growth of continuous films. The continuity of the very thin IMC films depends strongly on the interaction with the underlying substrate. Growth on an Al surface yielded discontinuous films for nominal thicknesses below 20 nm, while those above 20 nm had almost complete coverage and are considered continuous in this work. Figure 34 displays SEM and AFM images of those films.

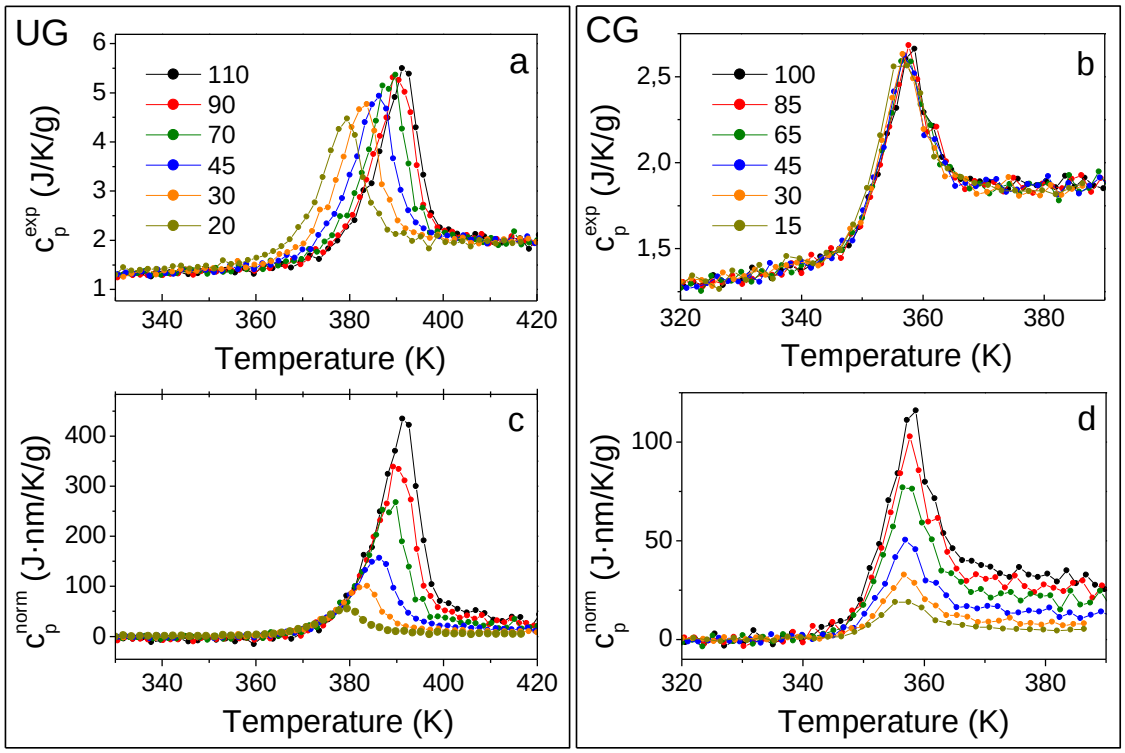

Figure 33. Heat capacity curves of IMC glasses versus temperature obtained by nanocalorimetry: (a) Mass-normalized specific heat of a) ultrastable glasses and (b) fast-cooled glasses. surface-normalized heat capacity of highly stable IMC thin film glasses. (c) Surface-normalized heat capacity for c) ultrastable glasses and d) fast-cooled glasses. The heating rate in all cases is 5 × 10^4 K/s. Legend: the thickness of the films in nm.

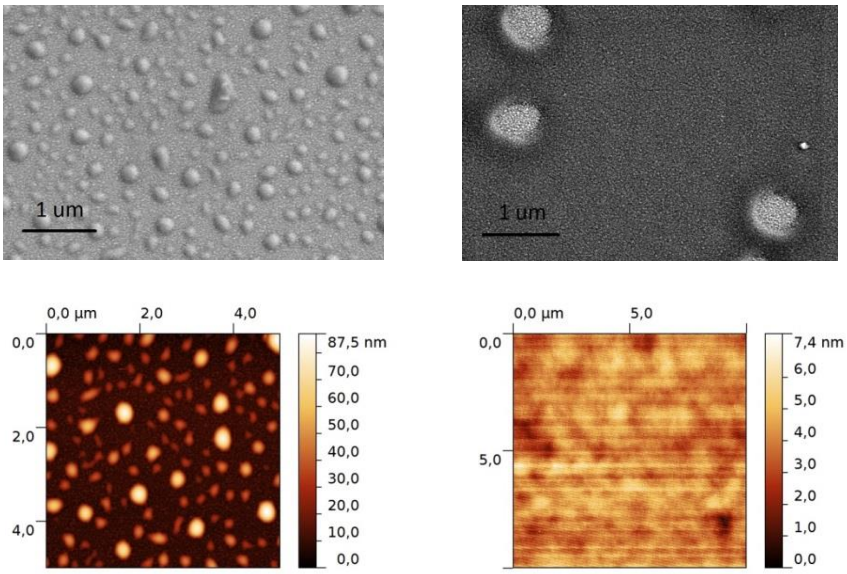

Figure 34. SEM (top) and AFM (bottom) images of IMC films with a nominal thickness of 5 nm (left) and 20 nm (right). It can be clearly appreciated how ultrathin films form isolated islands rather than continuous films, due to the weak interaction between substrate and molecule.

No size effects have been observed for the thermodynamic stability of IMC thin film glasses above 20 nm. We have calculated the limiting fictive temperature of glasses of different thicknesses prepared from the vapour and from the liquid. Figure 35 shows the values obtained for T_f' as a function of thickness for ultrastable and fast-cooled IMC films The T'_f appears to be constant for the range of film thickness under study and for glasses with very different stability (almost 50 K difference in T_f').

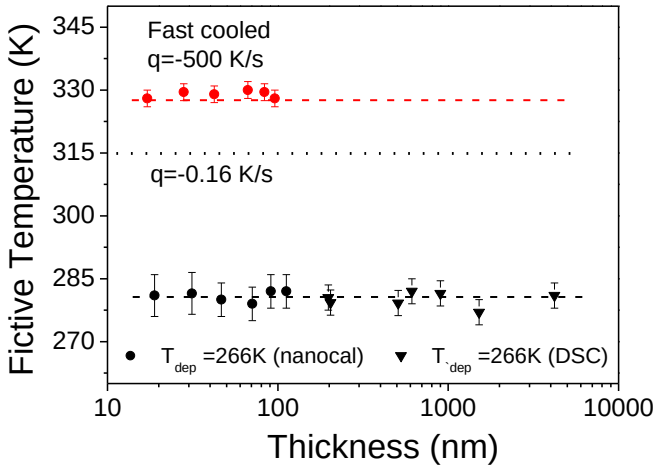

Figure 35. Limiting fictive temperature as a function of film thickness for UG (black) and FC (red) IMC glasses evaluated from nanocalorimetry (circles) and DSC (down triangles) data. As a reference, a black dotted line denotes the fictive temperature of a conventional glass, cooled at 0.16 K/s. Discontinuous lines are guides to the eye.

4.3.2 Transformation mechanism as a function of stability

Samples with intermediate stability, between that of the ultrastable glass (deposited at 266 K) and the conventional glass (deposited at 315 K or cooled from the liquid at 10 K/min) also start the transformation to the supercooled liquid via a heterogeneous process. By normalizing the heat capacity curves of these samples using equation 21 we find that they overlap along a limited temperature range, as seen in Figure 36 for glasses of different T_f'. This means that propagating front travels a certain distance before bulk transformation comes into play. We call this distance the crossover length, ξ. In general, ξ depends on the thermodynamic stability of the glass. In particular, less stable glasses present a lower ξ than ultrastable glasses. As a consequence, heat capacity curves of less stable samples of different thicknesses normalized using equation 21 overlap during a much reduced temperature range than in the case of the ultrastable glass, as seen in Figure 36g. In analogy, the shift observed in specific curves of stable samples is smaller in the case of less stable samples due to the earlier appearance of the bulk transformation.

Using equation 21, we can determine ξ for glasses with different stability from the normalized heat capacity curves. For example, ξ is roughly 5 nm for glasses with T_{dep} = 310 K, while, for glasses with T_{dep} = 266 K, ξ is around 900 nm, as we saw previously from the superposition of normalized heat capacity curves. Due to the limitations of the nanocalorimetry, layers much thicker than 100 nm cannot be properly analysed, which determines the maximum measurable crossover length using nanocalorimetry. On the other hand, water absorption precludes the analysis of vapour-deposited glasses with low stabilities by means of DSC, as we will see in chapter 7.

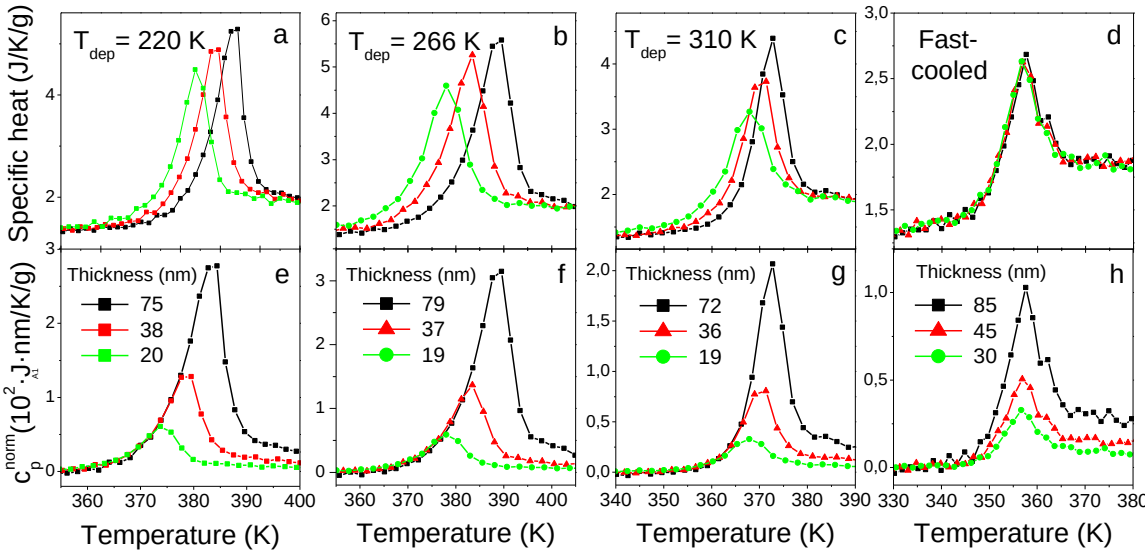

Figure 36. Specific heat curves of IMC glassy films for four different thicknesses deposited at (a) 220 K, (b) 266 K, (c) 310 K and (d) fast cooled, obtained by dividing the heat capacity curves by the corresponding mass. (e–h) correspond, respectively, to heat capacity curves of samples deposited at 220 K, 266 K, 310 K and fast cooled, normalized using equation 21.

4.4 Transformation rate

The transformation rate can be obtained from the heat capacity curves by introducing the experimental data in the left side of equation 21 and solving the differential equation. If the transformation is surface-initiated and propagates parallel to the surface, the transformation rate (or, in this case, the growth front velocity) and the derivative term of equation 21 are related by

$$v_F = \frac{d(d_l)}{dt} = \beta(t) d_0 \frac{dx_l}{dT} \tag{22}$$

where d_l is the transformed thickness, d_0 is the sample thickness, x_l is the transformed fraction and β is the time dependent heating rate during the measurement. We note that this expression is only applied in the temperature range at which the heat capacity from samples with different thickness overlaps after normalizing using equation 21.

We use a Matlab routine, with the Adams–Bashforth algorithm, to solve the differential equation, using the experimental curve as input data. In that way, we obtain the transformed fraction and the transformation rate plots as a function of temperature, as seen in Figure 37. The resulting transformation rate has baseline equal to zero and an area equal to one, keeping the same features, i.e. peak onset and maximum, of the original specific heat data. The excess enthalpy is obtained by imposing that x_l must go from 0 (glass) to 1 (supercooled liquid).

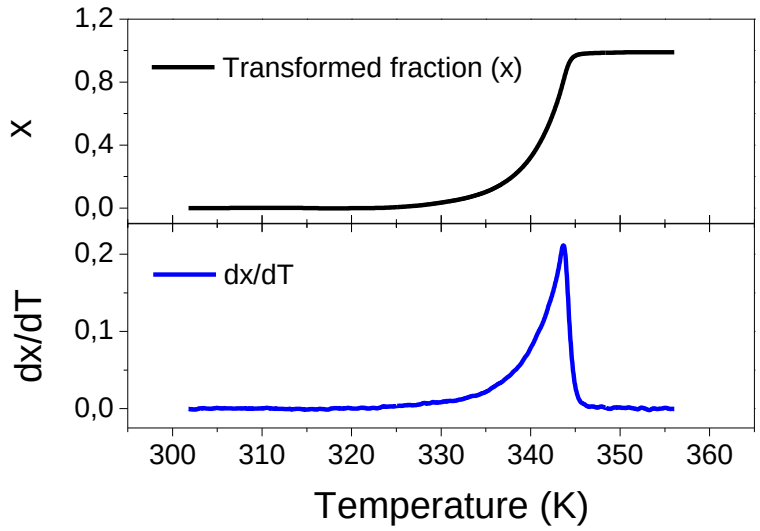

Figure 37. Solution of the differential equation 20 (black curve), using the Adams–Bashforth algorithm. Δ*h* is set considering that x must go from 0 (before the transformation starts) to 1 (when the transformation is finished). The blue curve corresponds to the transformation rate.

4.4.1 Dependence of transformation rate on temperature

The results shown in Figure 38 correspond to the growth front velocity of an ultrastable glass as a function of temperature. Since devitrification is a kinetic event with a T_g that shifts to high temperatures as the heating rate is increased, we are able to probe a much wider temperature interval than previously explored from isothermal scans. The transformation speed is derived for films with thickness from 20 nm to 50 nm, measured by nanocalorimetry at fast heating rates and

for films with thicknesses from 200 nm to 4 micrometres, measured by DSC at slower heating rates. In the case of the thicker films, we have only considered the temperature range where the transformation is dominated by a parallel growth front, i.e., the first stages of the calorimetric trace. Samples of different thicknesses collapse into a single curve in the region 325–340 K. In those measurements, we neglect the velocity values derived from the first few nm close to the surface of the films, since the DSC data is not very precise at this scale. Therefore, the represented data in the range 325–340 K correspond to front thicknesses from 20 nm up to approximately 400 nm. On the other hand, data evaluated from fast-scanning measurements collapse into a single curve in the region 365–390 K, corresponding to thicknesses from 1 nm up to 50 nm. That is, our data spans from T_g + 10 K up to T_g + 75 K, where T_g corresponds to the glass transition temperature of the conventional glass.

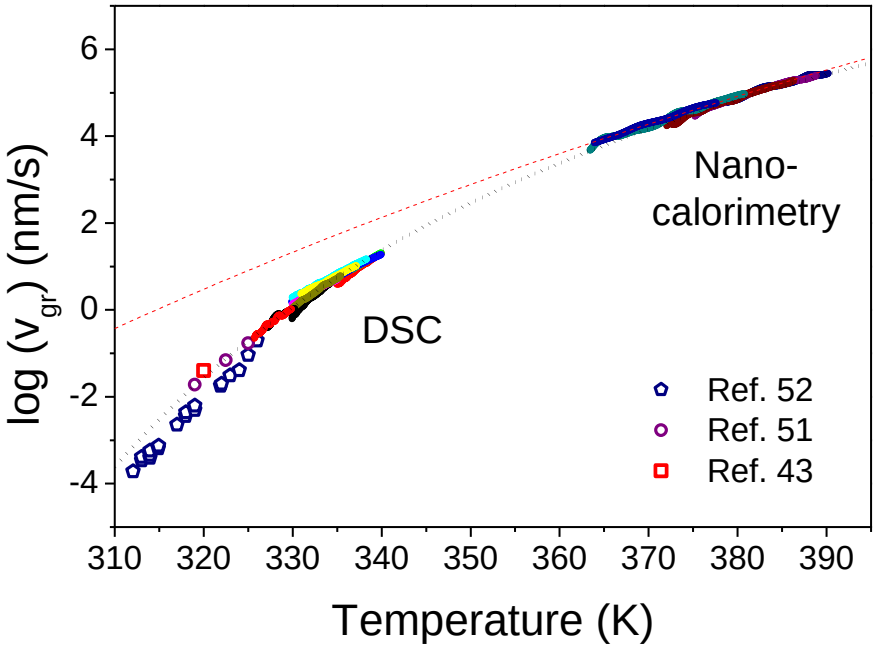

Figure 38. Logarithm of the transformation speed as a function of temperature for films with thicknesses from 20 nm to 4 µm evaluated from nanocalorimetry and DSC data using equation 22. The dotted black line corresponds to a fit of the data using the expression $v_{gr} = C\tau^{\alpha}$ where τ is the alpha relaxation time of the liquid and has been calculated using the VFT equation with values obtained by Paluch et al. for IMC[87], as explained in section 4.4.2. The dashed red line corresponds to an Arrhenius curve which is only able to fit the high temperature data.

Due to the small distance that the growth front of the less stable samples travels before the bulk transformation mechanism is triggered, it has not been possible to obtain growth front velocities at low temperatures. However, because of the high sensitivity of the nanocalorimetry technique,

we are able to extract transformation velocity values from the very beginning of the transformation, even for the less stable glasses, whose front only travels few nanometers before the bulk transformation comes into play.

In Figure 39 we plot the logarithm of the growth front velocity as a function of temperature for glasses grown at different deposition temperatures, in the range $0.63 < T_{dep} < 0.98T_g$. In contrast to previous measurements by ellipsometry, where the value of the growth front velocity for samples deposited above 290 K could not be directly evaluated[42], we resolve the growth front velocity for the whole deposition temperature interval.

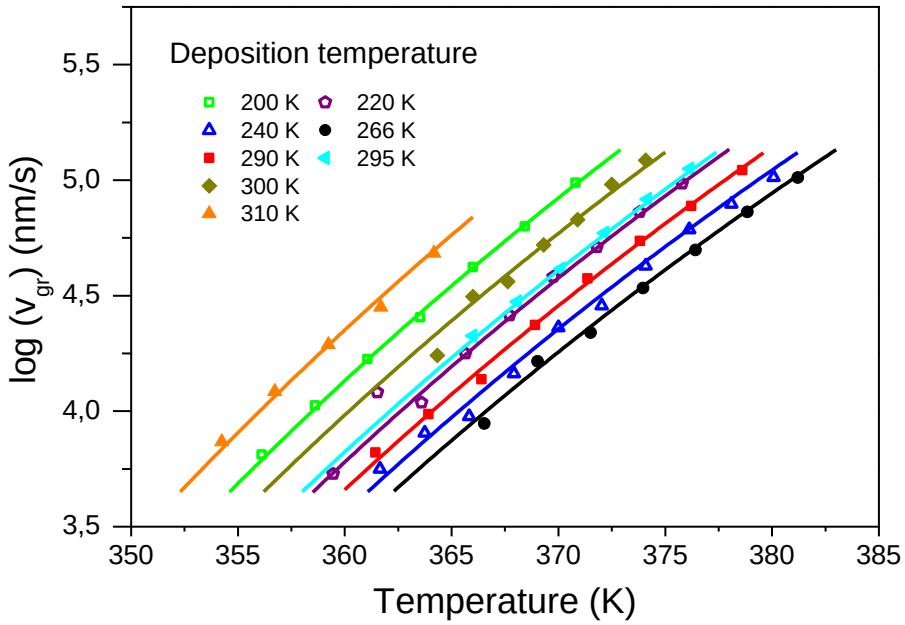

Figure 39. Logarithm of the growth front velocity as a function of temperature for IMC glasses. Continuous lines correspond to a fit of the data using the expression $v_{gr} = C\tau^{\alpha}$ where τ is the alpha relaxation time of the liquid and has been calculated using the VFT equation with values obtained by Paluch et al. for IMC[87], as explained in section 4.4.2.

A complementary representation of the data is presented in Figure 40, where the logarithm of the growth front velocity evaluated at three different temperatures is plotted as a function of substrate temperature. The slowest transformation rate corresponds to the most stable glass, deposited at $0.85T_g$ (266 K). Glasses deposited at higher or lower temperatures have faster transformation fronts. The further from $0.85T_g$ the deposition temperature, the faster the mobility of the front. We observe a 10-fold difference in the mobility of the front between the fastest and the slowest samples.

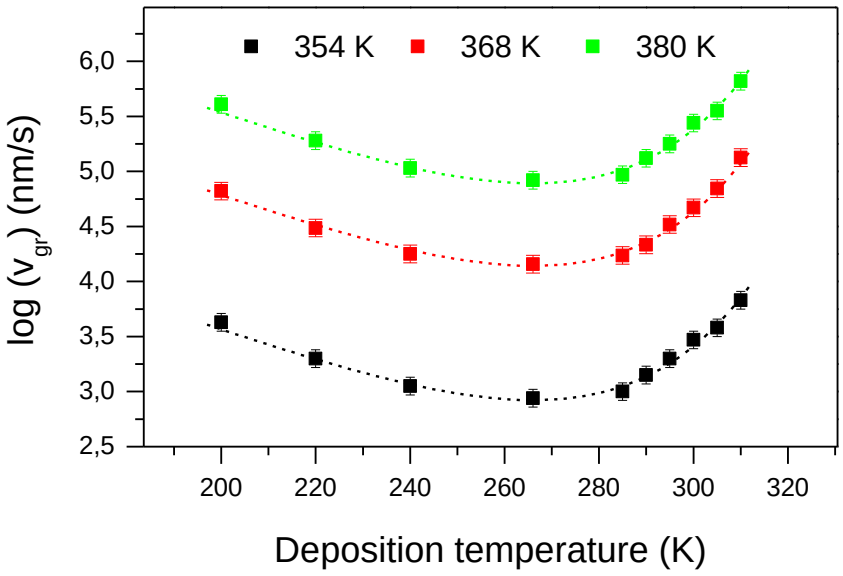

Figure 40. Logarithm of the growth front velocity at three different temperatures as a function of deposition temperature. In some cases, extrapolation of experimental data from figure 39 has been performed. Dotted lines are guides to the eye.

4.4.2 Dependence of transformation rate on structural relaxation time

Ediger and co-workers measured the front propagation velocity during the transformation of vapour deposited glasses of IMC and TPD by means of secondary ion mass spectrometry in a limited temperature range near ambient temperature[52]. They found that the front velocity could be related to the relaxation time of the corresponding supercooled liquid, described by a VFT expression (equation 5 Chapter 2). In particular,

$$v_{gr} = C\tau^{\alpha} \tag{23}$$

where C is temperature independent and α a constant. In the case of IMC, the VFT parameters are log $\tau_o = -19.36$, $T_o = 234$ K, and D = 17, deduced by Paluch et al.[87].

In this work, we have been able to measure front velocity values that expand a much larger temperature range, much more than previously reported. When we represent the logarithm of the growth front velocity as a function of $\log \tau$ we obtain a straight line not only in the low or high temperature range, but on the whole extended range, as seen in Figure 41. From a linear fit of the data, we find that the velocity of the transformation evaluated from calorimetric data scales as stated in equation 23, with $\alpha = -0.78$ and $C = 0.1$ (black dashed line in Figure 41, v_{gr} in nm/s). In spite of the uncertainty in the front speed of every line in Figure 41, the wide temperature range analysed diminishes the error on the slope compared to previous works[51,52,80]. We estimate the

error as ±0.01. Extrapolation to lower temperatures matches with front speed measurements on ultrastable IMC glasses by dielectric spectroscopy and ac nanocalorimetry measured by Ediger et al.[43]. The slope agrees within the experimental uncertainty with previous data obtained by SIMS by Ediger and co-workers ($\alpha = -0.85 \pm 0.06$)[52]. Remarkably, the evaluated exponent, around -0.8, holds for a very wide temperature range spanning almost 80 K and 12 orders of magnitude in relaxation time and it is independent of the experimental technique or the heating rate. The calorimetric signal obtained during the conversion of glass to supercooled liquid is proportional to the transformed fraction and does not directly probe the existence of one or two propagation fronts. We found a higher value of parameter C compared to SIMS data. In fact, the measured values of front velocity correspond to almost twice the front velocity measured by SIMS, which probes only the transformation of the glass surface. On the other hand, our data coincides with values measured by dielectric spectroscopy[51], which probes the whole sample simultaneously. These evidences suggest that our transformation occurs through a double front that initiates both at the free surface and at the interface with the substrate. The two-front hypothesis provides a growth front velocity that halves the one estimated in the case of just one propagation front.

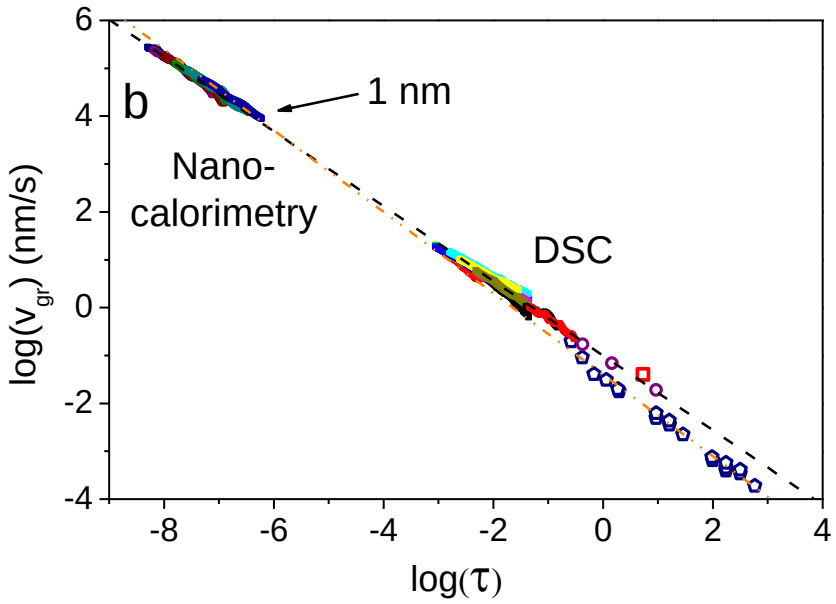

Figure 41. Log-log plot of the velocity of transformation vs. relaxation time. Continuous lines: this work. Symbols: blue circles, data from SIMS[52]; violet circles, data from dielectric spectroscopy[51]; red square, data from ac nanocalorimetry[43]. The value in the graph indicates the initial thickness (from the surface) at which the velocity of the transformation is evaluated. Thanks to the high sensitivity of nanocalorimetry, we can measure front velocities from the very beginning of the transformation, while front velocity from DSC data can only be obtained from 20 nm, as commented previously. In both graphs, the black dashed line corresponds to the function $v_{gr} = 0.1 \cdot \tau^{-0.78}$, where $\tau = \tau_0 \exp(DT_0/(T - T_0))$ is the VFT fit of the relaxation time using the bulk values for IMC[87].

The strictly linear relationship between $\log(v_{gr})$ and $\log(\tau)$ in Figure 41 in a very wide temperature (relaxation time) range emphasizes that the transformation speed is mostly driven by the mobility of the liquid, inversely proportional to its relaxation time. This observation agrees with theories based on the idea that the mobility of a region with different domains is governed by the sub-region with higher molecular mobility. That is, a very mobile region (liquid) neighbouring another region with lower mobility (glass) can induce and control the transformation from one region to the other. In this framework, our results show that the velocity of the transformation front mainly depends on the mobility of the liquid behind the liquid/glass interface.

The sensitivity of nanocalorimetry permits the evaluation of the growth front velocity, and hence the liquid mobility, from the first stages of the transformation, i.e., from the near-surface/interface regions. Therefore, our higher temperature data can be used to compare mobility at different depths, from regions near free surfaces/interfaces to the interior of the film. The curves of Figure 41 in the region 360–390 K show that the growth front velocity strictly follows the previously fit expression 23, which basically means that the mobility of the liquid region behind the liquid/glass interface remains constant irrespective of the position in the film. That is, the growth front velocity is independent of the penetration depth of the front in the film. If we consider two transformation fronts, the constancy of the front speed from the very first few nanometers of the transformation requires both fronts to start almost simultaneously, at the same temperature. Otherwise, we would observe a change in the growth front velocity, i.e., an acceleration of the transformation rate, when the second front would start the propagation. This observation is consistent with a weak interaction between the IMC molecules and the Al surface. As has been recently reported from molecular dynamics simulations[88], a weak interaction with the substrate may accelerate the dynamics in the liquid region near the substrate. This weak interaction also originates the lack of complete coverage during the first stages of the deposition, and therefore the discontinuous layers below 20 nm, as explained in section 4.3. On the basis of these premises, it is reasonable to think that both fronts initiate at approximately the same temperature.

Since surface and substrate molecules are expected to have a higher mobility, one would expect a faster growth front velocity at the very beginning of the transformation. As outlined above, the high temperature data clearly shows the growth front velocity is thickness independent from the very first nanometers of the transformation, as seen in Figure 41. This observation is compatible with two possible scenarios: (i) the existence of a liquid-like layer at the surface and interfaces of the glass or (ii) the crossing of surface diffusion and bulk diffusion in the supercooled liquid at the very high temperatures of the nanocalorimetry experiments. With respect to the first possibility, indeed, if a liquid layer with enhanced mobility exists at the surface/interfaces, as suggested in recent experiments, the first stages of the transformation observed by nanocalorimetry would involve the molecules that are already buried in the interior of the film,

i.e., beneath this liquid-like layer. Therefore, neighbouring molecules would remain identical independently of their position within the film. Mobility would always reflect a bulk property, and the transformation velocity would remain constant throughout the thickness of the layer. The second scenario relates to the comparison between surface and bulk dynamics at temperatures far above 315 K, the glass transition temperature of the conventional glass when heating at 0.16 K/s. As surface mobility has activation energies half the value of liquid mobility[38], it may well be that the nanocalorimetry measurements are actually probing the transformation of the molecules that are at the surface, but the similarity of surface and liquid diffusion at these very high temperatures leads to a thickness independent mobility. However, although we are not aware of surface mobility data in this temperature range, both RFOT and the coupling model, CM, predict a temperature crossing between surface and liquid bulk relaxation times at high temperatures[68,89]. Calculated values yield $\tau_s = \tau_b$ in the region around 460–470 K, much higher than the experimentally accessed temperatures by nanocalorimetry. That is, at 360–380 K, the surface relaxation times are still faster than the liquid by several orders of magnitude. Although not conclusive, the hypothesis of the existence of a liquid-like layer seems more feasible to account for the observed thickness independent growth front velocity. Since the calorimetric chips permit very fast stabilization times, isothermal measurements may prove useful to evaluate the impact of surface mobility.

Figure 42 shows a log–log plot of the front velocity as a function of the alpha relaxation time of the liquid for glasses deposited at different substrate temperatures. In this representation, the points corresponding to each sample can be fit by perfectly straight parallel lines. The slope, associated with the exponent α in equation 23, has a constant value of -0.78 ± 0.01 in all cases. The difference between samples comes only from the pre-factor C of the same equation, which is different depending on the deposition temperature. However, this pre-factor is completely independent of τ in the probed temperature range, showing that the temperature strongly affects the mobility of the liquid, while the mobility of the glass, associated with this pre-factor C, is much less affected by the temperature. A similar result was obtained by D. M. Walters et al. on TPD glasses[72]. A possible implication of this result is that the mobility of glasses of different stability evolves similarly with temperature.

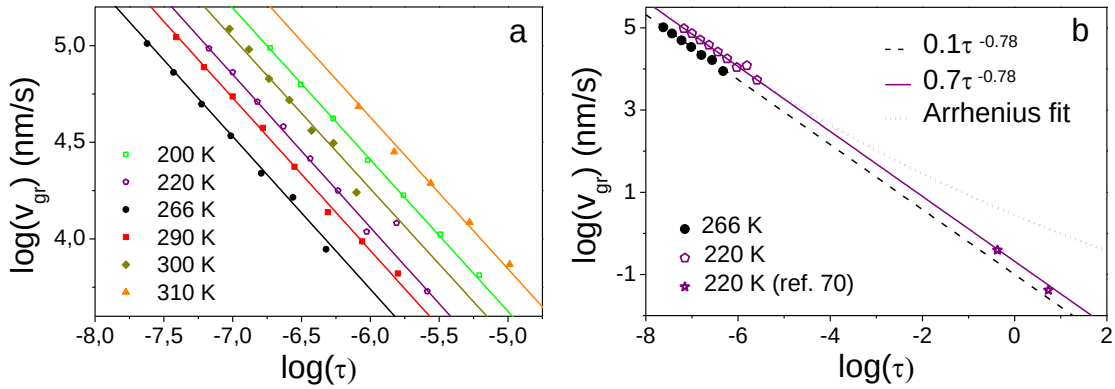

Figure 42. (a) Log–log plot of growth front velocity for samples deposited at different substrate temperatures as a function of the alpha relaxation time of the liquid. The lines correspond to a fit of the data using equation 23, where the exponent α has been kept constant at a value of 0.78 ± 0.01 and the pre-factor C depends on how the glass has been produced. (b) Extrapolation of the fit for two deposition temperatures to higher values of τ. The same function can fit the data obtained by nanocalorimetry (this work) and by ellipsometry (extracted from Dalal's work[80]) for a sample deposited at 220 K. The dashed line corresponds to a fit of the high temperature data (T_{dep} = 220 K) extended to the entire relaxation time range considering an Arrhenius dependence of the growth front velocity with temperature.

The accessible temperature range using quasi-adiabatic nanocalorimetry is rather limited, covering a maximum of 15 K for each sample. As we mentioned earlier, the width of the temperature range we analyse is critical when concluding the type of dependence between growth front velocity and temperature. In order to extend the analysed temperature range, we plot in Figure 42b results obtained by Dalal and Ediger for an IMC sample deposited at 220 K and measured by ellipsometry at 320 and 325 K[80]. Since they are able to distinguish between the front that starts at the surface and the front starting at the interface, and we are not, we have interpolated their data and we have taken the average velocity of the two fronts. Analogously to the behaviour of the ultrastable glasses, the same dependence is extended over the whole range of τ, i.e. temperature, which now covers 8 orders of magnitude in the alpha relaxation time, or equivalently, 55 K in temperature, indicating that the influence of liquid relaxation time on the glass transformation holds across a very wide dynamic range. We also present, both in figure 38 and figure 42b, an alternative fit of the high temperature data using an Arrhenius dependence of growth front velocity on temperature, extended over the whole range of temperature and relaxation times respectively. As can be clearly seen, although an Arrhenius dependence is compatible with the high temperature data, it is not possible to fit both the high and low temperature experimental points with the same function.

4.4.3 Dependence of transformation rate on glass properties

Figure 42 clearly highlights that the growth front velocity depends on the deposition temperature and we have already seen that deposition temperature determines the properties of the glass. On the other hand, it has been generally assumed that the mobility of the glass is directly related to its density or to its limiting fictive temperature[36]. We have calculated the limiting fictive temperature of all samples by integrating the specific heat curves, as explained in section 2.5. As shown in Figure 43a, glass density and T_f' display a good correlation in the case of IMC glasses deposited from the vapour phase. We are not aware that this correlation has been tested in other stable glasses; therefore, we are cautious to draw generalities on this respect. One of the main outcomes of our heat capacity analysis is Figure 43b, which represents the growth front velocity as a function of the fictive temperature of glasses deposited between 0.63–0.98T_g.

Interestingly, we observe two branches, i.e. two glasses that have the same limiting fictive temperature and have been grown at different deposition temperatures can have very different growth front velocities. In both of these branches, the transformation rate increases with T_f', which means that, generally speaking, the less stable is the glass, the faster is the front. Figure 43 corroborates previous views that a unique fictive temperature cannot be taken as a signature of the structural state of the glass in equilibrium with the liquid[33,90]. This explains why correlations between growth velocity and density cannot be accomplished simultaneously over the whole deposition interval, as shown in Figure 44. In a previous work, Dalal and Ediger showed that it was possible to correlate growth front velocity and density for samples deposited below 0.85T_g, but it was not possible to extend this correlation to samples deposited above this temperature[80]. In Figure 44 we show how, by using appropriate scaling factors, it is possible to find a correlation also for deposition temperatures above 0.85T_g.

Of course, our results stand for thin films where the main transformation mechanism occurs through heterogeneous growth fronts. Whether a similar behaviour occurs for a homogeneous transformation mechanism in bulk stable glasses it is still not known.

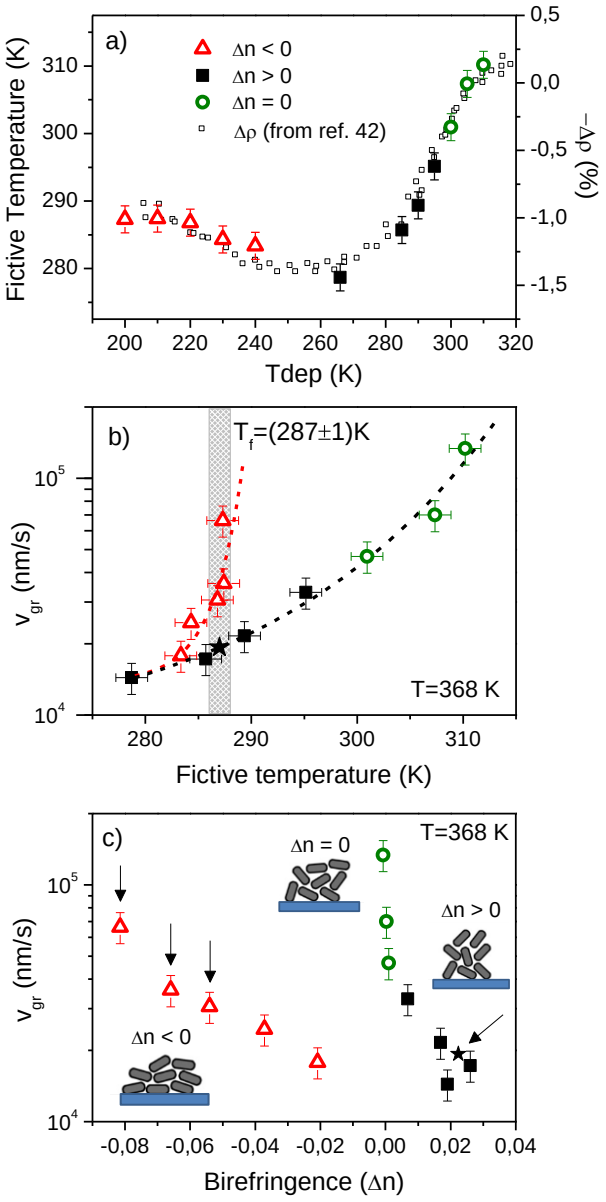

Figure 43. (a) Comparison between limiting fictive temperature and density increment as a function of deposition temperature. (b) Front velocity as a function of limiting fictive temperature. (c) Front velocity as a function of birefringence. The arrows indicate 4 samples with T_f' = (287 ± 1) K. The star symbol has been obtained by interpolating the data in order to represent a sample with T_f' = 287 K. Density and birefringence data have been extracted from ref.[42]. In all panels, symbols correspond to different deposition conditions and the corresponding birefringence: red triangles correspond to samples deposited below 250 K (0.8T_g), which have negative birefringence; black squares correspond to samples obtained between 250 K and 300 K (0.8T_g and 0.95T_g respectively), which have positive birefringence; green circles correspond to samples deposited above 300 K, with no birefringence. The cartoons (adapted from ref.[49]) represent schematically the distribution of the molecules for each type of birefringence.

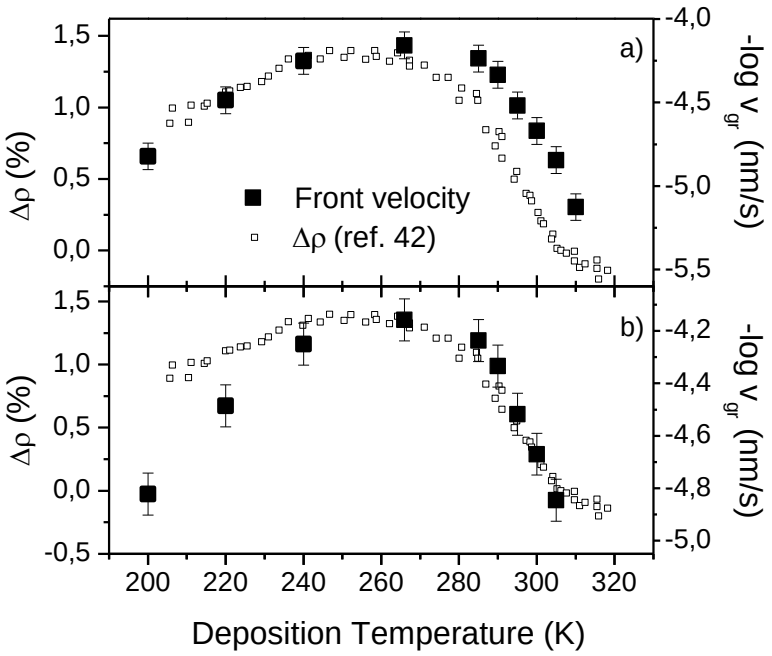

Figure 44. Comparison between density change and the logarithm of the transformation front velocity. The scales have been adjusted to coincide in the region of deposition temperature below $0.85T_g$ (a) and above $0.85T_g$ (b). Density data have been extracted from ref.[42].

Wisitsorasak and Wolynes performed numerical calculations on the growth front mobility using random first-order transition theory[83]. In that study, they calculated the velocity of the front for TNB glasses (a similar glass to IMC) with T_f' differing 10 K and found that the impact of T_f' variation was less important than the effect of temperature. The velocity of the front of stable glasses produced by random pinning by Hocky et al. also depends on stability (or density of fixed particles), although in this case there is not a direct estimation of limiting fictive temperature for their pinned samples[84]. It is worth noting that computer modelling was carried out with isotropic glasses.

But then, what controls the growth front velocity? Our data clearly demonstrate that while the liquid mobility and the limiting fictive temperature of the glass (density) play a relevant role in the mobility of the front, there is another, hidden, dependence not yet considered. To shed light on this issue we need to comment first on the birefringence measurements of Ediger and co-workers where they showed broadly three different regimes of molecular anisotropy depending on the deposition temperature[42] (Figure 45).

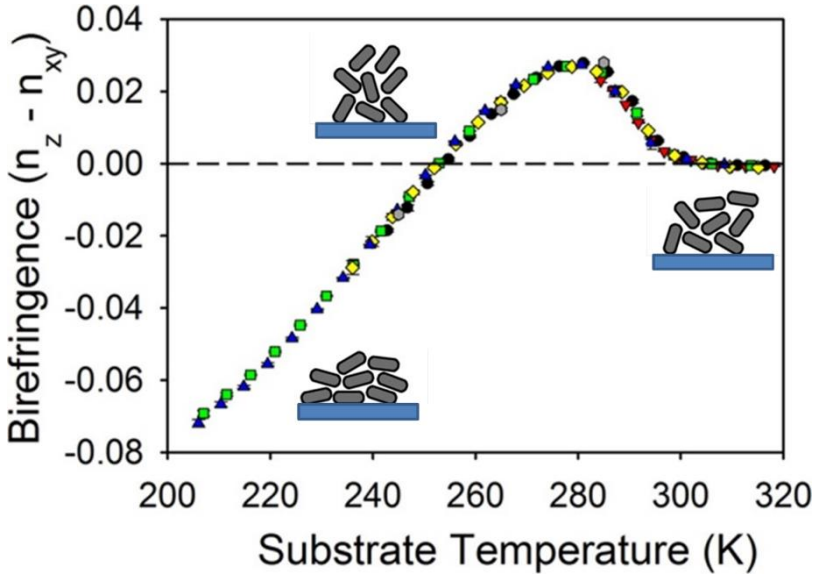

Figure 45. Birefringence of vapour-deposited indomethacin glasses as a function of substrate temperature, showing a range of molecular orientations. n_z is the index of refraction perpendicular to the substrate, and n_{xy} is the index of refraction in the plane of the substrate. The dotted line indicates the absence of birefringence. Glasses deposited from 250 K to 295 K present a slight positive birefringence, while those grown below 250 K present a negative birefringence, which increases as the deposition temperature is lowered. Further details are given in ref.[42]. Image adapted from ref reference [42].

Glasses deposited at substrate temperatures lower than 250 K show a negative birefringence factor, while those deposited between 250 and 300 K display a positive value of this parameter. Above 300 K, the birefringence turns out to be zero. The existence of birefringence is linked to molecular orientation. Below 250 K, IMC molecules are on average with their long-axis oriented parallel to the substrate surface, whereas between 250 and 300 K the molecules tend to align perpendicular to the substrate. Above 300 K the glass is mostly isotropic. The existence of two branches in Figure 43b and c could be understood from the packing anisotropy of the samples. Figure 43c shows the growth front velocity as a function of the birefringence using $\Delta n(T_{dep})$ values from Figure 45. We disentangle the role of molecular anisotropy in the growth front velocity by comparing samples with identical limiting fictive temperature, such as the ones marked with arrows in Figure 43c, for which $T_f' = (287 \pm 1)$ K. For a given T_f', the stronger the orientation of the molecules along the plane of the substrate, the faster the transformation rate. Low absolute values of birefringence give rise to slower fronts. The available data do not permit us to infer if a strong orientation of the molecules in the direction perpendicular to the surface would result in faster fronts. In spite of this shortcoming, the presented data suggest a clear dependence of the mobility of the front on the anisotropy of the glass.

4.5 Chapter summary

Physical vapour deposition of organic molecules opens the possibility to produce glasses with tuneable stability. At deposition temperatures around $0.85T_g$, glasses with an unprecedented high stability can be obtained, showing a glass transition onset temperature tens of Kelvin above its conventional value and a high thermodynamic stability. The thermal stability of these glasses is evaluated from the enthalpic limiting fictive temperature, which indicates the temperature at which glass and liquid have the same enthalpy. T_f' does not depend on the heating rate, even for a very wide heating rate range. The limiting fictive temperature of glasses grown at deposition temperatures above $0.85T_g$ coincides with the corresponding deposition temperature, indicating that, at these conditions, the produced glass is in equilibrium with the liquid, in accordance to previous results obtained from density measurements[42].

Vapour deposited glasses also show striking properties which are not observed in glasses produced by cooling the corresponding liquid, such as a different transformation mechanism. The impact of the transformation mechanism on the interpretation of specific heat curves of glasses of different thermal stability is critical. While ordinary glasses transform into the supercooled liquid via a homogeneous bulk transformation mechanism, thin films glasses of higher stability transform heterogeneously via a front propagating from the surface and/or the interfaces. Specific heat curves of vapour deposited glasses of indomethacin show an apparent change of onset temperature of devitrification with size. However, we see that the limiting fictive temperature is independent of the size of the layer and that this apparent size effect originates from the transformation mechanism. In fact, an ad-hoc surface normalization of the heat capacity yields curves which collapse into a single one in the temperature range in which the transformation takes place via a heterogeneous process. The length of this range, the crossover length, increases with stability. While ultrastable glasses transform via front propagation up to 900 nm in thickness, less stable samples, with T_f' = 310 K, show superposition of normalized heat capacity only up to 5 nm in thickness.

Furthermore, this ad-hoc surface -normalization can be used to evaluate the velocity of the growing front. Taking advantage of the ultra-fast heating rates accessible by quasi-adiabatic calorimetry techniques, previous values of growth front velocity are expanded in this work up to Tg+75 K, covering 12 orders of magnitude in relaxation time units. We find that the growth front velocity of glasses with different stability can be expressed as a function of the relaxation time of the supercooled liquid through an expression that holds in the entire temperature range. This finding agrees with some theories that claim that mobile regions control the dynamics of the transformation[78,83]. Interestingly, while one would expect a higher mobility of the topmost molecules, we find that the mobility of the supercooled liquid in the region behind the

transformation front remains constant throughout the thickness of the layer, from the very first nanometers. This finding suggest that either the topmost molecular layer is not reflected in the calorimetry measurements, since it is already a liquid, or that, in the high temperature range, the mobility of surface and bulk molecules is similar.

While the mobility of the supercooled liquid strongly affects the front velocity glasses, the thermodynamic stability of the glass only affects the transformation weakly, at least in the stability range explored in this work. Although the transformation rate changes by a factor of 10 between the most and less stable glasses, the relation between the mobility of the front and the thermodynamic stability of the glass is not uniquely defined. In particular, glasses grown above 280 K present a different dependence of the growth front velocity on fictive temperature compared to glasses grown out of equilibrium at $T_{dep} < 250$ K. These data clarify previous reports and supports the evidence that fictive temperature or density are not an absolute indicator of the properties of the glass just by themselves, at least when the structure is not completely isotropic. A possible interpretation is that the growth front velocity depends on three terms: the mobility of the liquid at a given temperature, the mobility of the glass and the arrangement of the molecules in the glass.

5. UNIFIED RELAXATION TIME DESCRIPTION OF GLASSES AND LIQUIDS

Part of this Chapter is currently under consideration and available at arXiv:1603.08829.

5.1 Chapter introduction

The relaxation time of the liquid increases exponentially during cooling, at a pace determined by its fragile or strong nature. In the laboratory time scale, around certain value of the relaxation time, the molecules do not have enough time to explore the complete configurational space and get trapped inside local energy minima, forming a glass[12,13,26]. Below this temperature, upon further cooling, the relaxation time of the glass is considered to follow a much softer Arrhenius-like expression[32]. For many years, there has been an increased interest in the time scales of physical processes occurring below the glass transition temperature due to the importance of understanding and controlling relaxation processes in the glass. On the other hand, the inherent unstable nature of glasses has prevented detailed investigations of their properties during heating at temperatures above the conventional T_g, where a glass would irreversibly relax into the equilibrium liquid state.

The relaxation time of glasses has generated certain debate in the glass science community[18,32,56]. In the case of equilibrium systems, the Adam-Gibbs (AG) formalism has provided a suggestive connection between their dynamics and thermodynamics[91]. Although not completely rigorous, this model has been able to describe the relaxation behaviour of deeply supercooled liquids remarkably well, yielding the well-known Vogel-Fulcher-Tamman equation (equation 5, Chapter 2). However, much below T_g, in the glass state, the configurational entropy of the system remains almost constant and, therefore, it is generally accepted that the dependence of the glass relaxation time with temperature responds to an Arrhenius expression[32]. However, due to the intrinsically slow relaxation times of such systems below the glass transition temperature, the access to experimental data requires enormous amounts of time, which makes measurements impractically long. On the other hand, at higher temperatures, the glass transforms irreversibly into the supercooled liquid in shorter time scales. In this temperature range, the access to relaxation time values requires both ultrafast heating and a rapid dynamic response, accessible using fast scanning nanocalorimetry[60,62,66,92]. The influence of stability on the relaxation time of the glass is also a relevant topic in the current literature[31,93]. Vapour-deposited glasses offer a convenient route to

explore the influence of stability on the melting of the glass over a much larger temperature range than ever before.

The fulfilment of density scaling relationships is also an active topic in the condensed matter physics community. It has been shown that polymers and Van der Waals' bonded liquids obey power-law density scaling relationships[94–96], which means that the average relaxation time of the liquid is a function of Tv^{γ}, where $v(T,P) = 1/\rho$ is the specific volume and γ is a material constant. The idea behind the scaling of relaxation times arises from the consideration that the local dynamics of liquids are governed by a generalised repulsive potential with spherical symmetry that scales with γ[94]. This assumption is not strictly valid for atomic interactions such as hydrogen bonds, although even in these cases the power-law scaling yields superposition of relaxation times as a function of T and v [95]. Although the scaling relation was originally formulated for supercooled liquids, we extend it to glasses with different stabilities, expressing the specific volume as a function of thermodynamic and limiting fictive temperature.

5.2 Determination of relaxation time of vapour deposited glasses

We use fast scanning calorimetry to determine the heat capacity of glasses of indomethacin and toluene deposited at different deposition temperatures and therefore embedded with different stability. We use thick films (~1-3 μm for IMC and ~1 μm for toluene) in order to guarantee that the melt takes place homogeneously throughout the sample. As an example, in the case of the most stable IMC glasses, we have to use films thicker than 900 nm. We infer values of relaxation time at the devitrification onset temperature, T_{on}, by applying the known relationship $\tau_1\beta_1 = \tau_2\beta_2$[97], as shown in Figure 46a. A reference value of $\tau_1 = 100$ s, considered as the relaxation time of the glass at T_{on} when heated at $\beta_1 = 0.167$ K/s [12,24,87], is employed, though we remark that slight variations on this value would yield equivalent conclusions. On the other hand, we also estimate the transformation time of each glass at the maximum of the transformation peak using the expression $t_{trans}(T_{max}) = \Delta T/\beta_m$, where ΔT is the width of the transformation peak and β_m the mid value of the heating rate during the transformation, as shown in Figure 46b. This method for inferring the transformation time has already been used by Busch et al.[98].

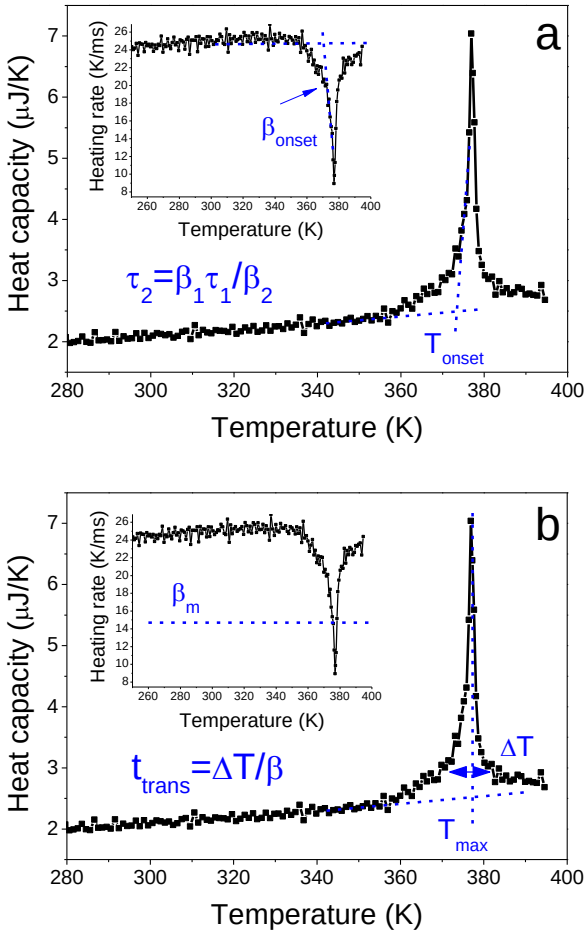

Figure 46. Calculation of relaxation and transformation times from heat capacity data. a) In the first approach, we use the expression $\tau_1\beta_1 = \tau_2\beta_2$ to obtain the value of glass relaxation time from the heating rate of the experiment, assigning this value to the onset temperature. b) In the second approach, we calculate the transformation time from the width of the transformation peak and the midpoint value of the heating rate, assigning it to the temperature at the maximum of the transformation peak.

To quantify the stability of the glass we use the enthalpic limiting fictive temperature, T_f'. We note that the measured values of limiting fictive temperature are independent of the heating rate of each calorimetric scan, as already explained in section 4.2. The choice of a convenient heating rate, in the range $0.0167 - 2 \cdot 10^4$ K/s, permits us to keep the system trapped in its initial glassy state along a variable temperature range, covering up to 75 K in temperature between the slowest and the fastest heating rates, while measuring the heat capacity during the transformation.

5.2.1 Transformation and relaxation time correspondence

In order to o confirm the validity of the two approaches, we compare the results yielded by the transformation and relaxation time expressions with the measured value of the transformation time during an isotherm at the corresponding temperature. In Figure 47a we show the calorimetric trace of the glass transition of an ultrastable glass measured at $\beta = 0.033\mathrm{K/s}$. We compare the transformation time calculated using the expression $t_{trans}(T_{max}) = \Delta T/\beta$ with the transformation time measured during an isotherm at T_{max}. The transformation times obtained from the two methods, 182 and 150 seconds respectively, are fairly comparable. On the other hand, we derive the relaxation time of the same glass at the onset of the transformation using the expression $\tau_1\beta_1 = \tau_2\beta_2$, taking as reference values $\tau_1 = 100\ s$ and $\beta_1 = 0.167\ K/s$. In particular, for this ultrastable glass we obtain $\tau_2 = 506\ s$. We can compare this value with the transformation time obtained by performing an isothermal measurement at the onset temperature. In this case the transformation time is 550 s, in fair agreement with the previous result.

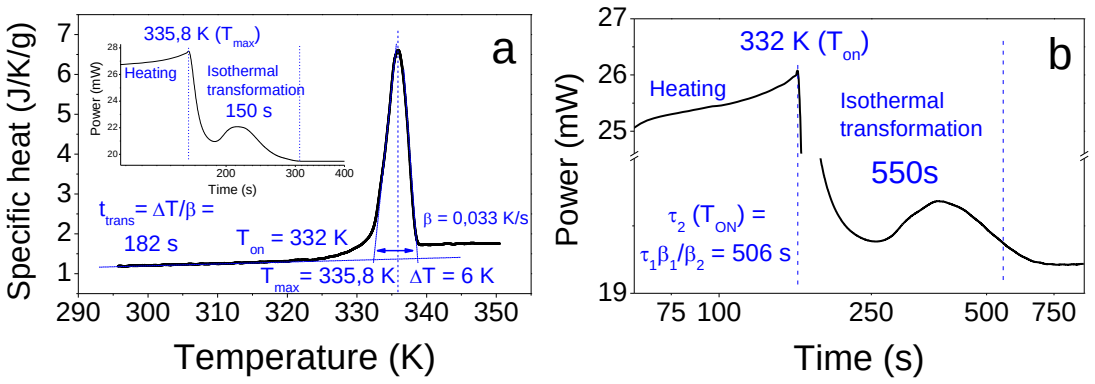

Figure 47. Comparison between procedures to determine relaxation times. a) DSC scan of an IMC glass deposited at T_{dep} = 266 K, heated at 0.033 K/s. From the width of the peak and the heating rate, the transformation time is inferred as indicated and assigned to the temperature where the maximum of the peak appears. The inset shows a DSC isotherm performed at the temperature of the maximum of the peak. The transformation time is considered to be the time elapsed from the beginning of the isotherm process to the moment at which the power output of the DSC is constant. . b) DSC isotherm performed at the onset temperature of the transformation. The transformation time is fairly equivalent to the relaxation time inferred using the expression $\tau_1\beta_1 = \tau_2\beta_2$, as explained in the text.

A hypothetical non-zero distribution of relaxation times in the sample would induce certain error in the determination of a unique value of transformation or relaxation time. Talansky et al. found that the distribution of transformation times in an ultrastable vapour-deposited glass of methyl-

m-toluate was around 25%[99]. On the other hand, we have observed that the width of our transformation peaks remains approximately constant for glasses of different stabilities when measured at a given rate. We can assume, therefore, that the effect of distribution times, if any, is similar for al stabilities. Moreover, a distribution of 25% in transformation time would be below our experimental uncertainty in the evaluation of ΔT and would not affect our conclusions.

5.3 VFT-like unified description

Figure 48 portrays data of both relaxation and transformation times for vapour deposited glasses of indomethacin and toluene grown at different temperatures, in equilibrium with the liquid. The data corresponds to glasses measured at various heating rates in the range comprised between 0.0167 K/s and $2 \cdot 10^4$ K/s. We also show data corresponding to liquid-cooled Au-based bulk metallic glasses aged to equilibrium at 373 and 383 K (data extracted from ref.[100]). For each of these materials, we also show the relaxation times of the respective supercooled liquids.

In order to describe the experimental data of Figure 48 we propose an empirical generalisation of the VFT equation 5 aimed at describing the dynamics of supercooled liquids and glasses with different thermal stability:

$$\tau_g = \tau_{g0} e^{\frac{\xi(T_f')T_0}{(T-T_0)}} \quad (24)$$

where all the parameters have an analogous meaning as in equation 5. In this case, however, D has been substituted by a linear function of the limiting fictive temperature of the glass, $\xi(T_f',) = AT_f' + B$. By definition, in a supercooled liquid $T_f' = T$ at all temperatures. We use equation 24 to simultaneously fit all the experimental data, where the only non-shared parameter is T_f'. All the parameters are allowed to adjust, except the limiting fictive temperature of the conventional glass cooled at -0.0167 K/s, which is fixed to T_f'= 315 K. We initially assume that relaxation and transformation time are equivalent[98]. Table 1 shows the values obtained for the fitting parameters. The resulting values of T_f' yielded by the simultaneous fitting of all glasses and the supercooled liquid are in reasonable agreement with the measured enthalpic limiting fictive temperature of each glass, as seen in Table 3.

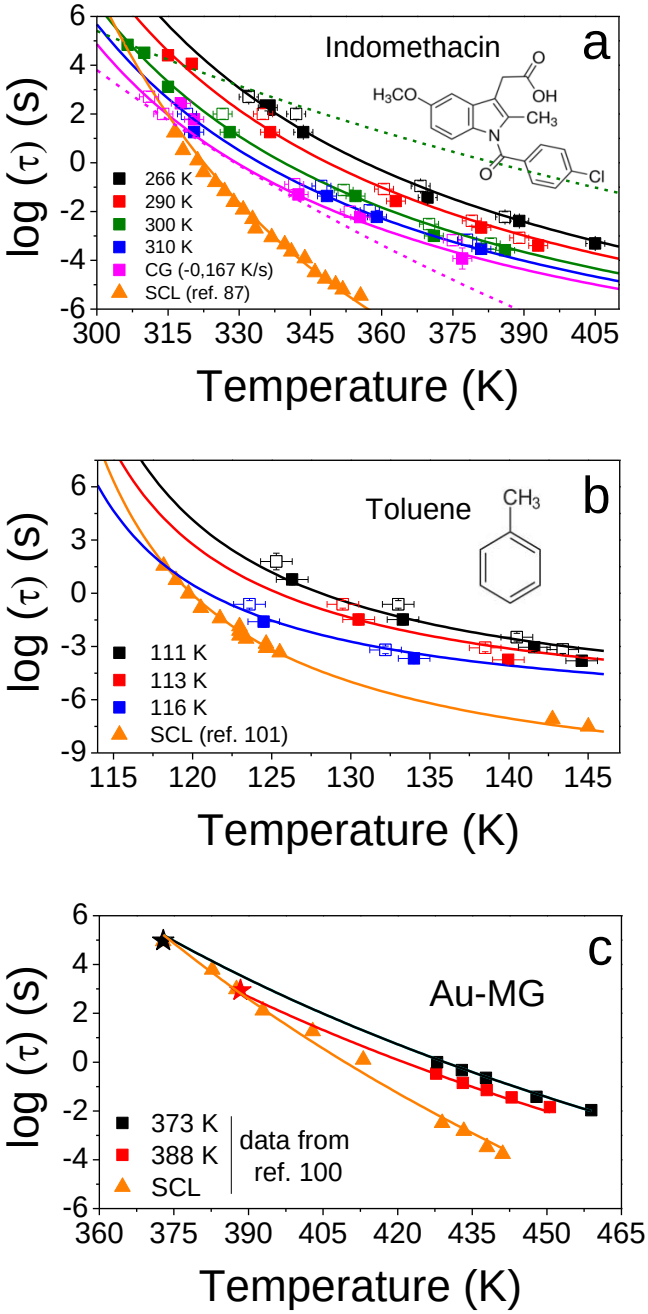

Figure 48. Relaxation times (open symbols) and transformation times (filled symbols) derived from calorimetry experiments for three materials, (a) IMC, (b) toluene and (c) Au-based bulk metallic glass (BMG) from ref.[100]. The data correspond to glasses with different stabilities and to the alpha relaxation times of their respective supercooled liquids (triangles). The temperatures in the legend correspond to deposition temperatures for IMC and toluene and to the aging temperature for the Au-based BMG. The conventional glass (CG) has been obtained by cooling the liquid at 0.167 K/s. The stars in (c) are estimated points assuming that the transformation time of the glass equals the equilibrium relaxation time at T_f'. The solid lines correspond to the best fit of the experimental points using equation 24. The fit parameters are presented in Table 1. The green dotted line in (a) corresponds to the glass relaxation time of a glass with T_f' = 304 K calculated with the Adam-Gibbs-Vogel (AGV) equation[31]. The pink dashed line in the same graph corresponds to an arbitrary Arrhenius curve, showing that the experimental data clearly exhibit super-Arrhenius behaviour.

The pink dashed line in Figure 48a clearly shows that, in an extended temperature range, the temperature dependence of the glass relaxation time deviates from the Arrhenius predictions of most of the considered models at lower temperatures[32]. We also note that, in the probed temperature range, our experimental results clearly differ from those predicted by the Adam-Gibbs-Vogel (AGV) equation (green dashed line in Figure 48a) which has been often satisfactorily applied in a short temperature range around the conventional T_g[31].

Considering that both glass and liquid can be satisfactorily described by our proposed model, there must be an equivalence between the parameters of the VFT and those that appear in equation 24. Introducing that $T_f = T$ for the supercooled liquid in equation 24, we can find a correspondence between equation 5 and equation 24,

$$\tau_{g0} e^{\frac{\xi(T) T_0}{(T-T_0)}} = \tau_0 e^{\frac{D T_0}{(T-T_0)}} \tag{25}$$

Taking natural logarithms and isolating, $\xi(T)$, we obtain that,

$$\xi(T) = -\frac{1}{T_0} \ln\left(\frac{\tau_{0g}}{\tau_0}\right) T + \left(D + \ln\left(\frac{\tau_{0g}}{\tau_0}\right)\right) \tag{26}$$

Assuming that $\xi = AT_f + B$, we see that,

$$A = -\frac{1}{T_0} \ln\left(\frac{\tau_{0g}}{\tau_0}\right) \tag{27}$$

$$B = \left(D + \ln\left(\frac{\tau_{0g}}{\tau_0}\right)\right) \tag{28}$$

From where we obtain that:

$$D = AT_0 + B \tag{29}$$

$$\tau_0 = \tau_{0g} e^{AT_0} \tag{30}$$

The calculated values of D and τ_0 using equations 29 and 30, shown in table 1, are fairly similar to those obtained from a VFT fit[87,100,101]. We want to remark that we have obtained these two parameters from a simultaneous fitting of glass and liquid relaxation time data.

In the VFT equation, the parameter D is related to the fragility of the liquid. From the definition of the fragility index[12,27], m, and equation 5, we can obtain the following equation:

$$m = \frac{1}{\ln 10} \frac{\left(\frac{DT_0}{T_g}\right)}{\left(1-\frac{T_0}{T_g}\right)^2} \tag{31}$$

T_g is typically considered as the temperature at which the relaxation time of the system equals 100 seconds. From equation 31, substituting $\tau_\alpha(T_g)$ by 100 s and isolating T_g, we obtain the following relation between m and D,

$$m = \frac{\ln\left(\frac{100}{\tau_0}\right)}{\ln 10}\left(\frac{\ln\left(\frac{100}{\tau_0}\right)}{D} + 1\right) \quad (32)$$

Evaluation of m using the parameters listed in Table 1 yields m = 54 for the Au-based bulk, metallic liquid in fair agreement to the value measured by Wang et al., m = 49[100]. To do the calculation we have considered T_g = 395 K, the temperature at which $\tau_\alpha = 100$ s [100]. The obtained fragility value for IMC is m=89, similar to m=83, measured by Wojnarowska et al.[87] using dielectric spectroscopy. In the case of toluene, we obtain a fragility of m = 131. Kudlik et al.[102] reported a fragility parameter for toluene of m = 122. While from the VFT expression reported by Hatase et al.[101], m = 130.

Table 1. Parameters obtained by simultaneous fitting of the relaxation times for glasses with different stability and for the supercooled liquid using equation 24. τ_0 and D have been calculated using equation 30 and 29 respectively.

	T_0 (K)	A (K^{-1})	B	τ_{g0} (s)	τ_0 (s)	D
Indomethacin	230.54	-0.106	44.93	2.69e-12	8.9e-23	20.55
Toluene	105.19	-0.108	15.3	5.5e-8	7.08e-13	3.94
Au-BMG	129.45	-0.222	203.45	3.98e-23	1.82e-35	174.75

To further corroborate that transformation and relaxation time data can be safely considered as equivalent magnitudes, at least in the experimental conditions of this work, we plot in Figure 49, in separated graphs, data corresponding to transformation and relaxation times of liquid and glassy IMC. We fit the experimental data from each of the graphs using equation 24. The obtained fitting parameters (see Table 2) are similar in the two fits, and are also similar to those obtained from the joint fit of Figure 48. Furthermore, the values of T_f' obtained from the fitting of the two sets of data are similar (Table 3). Given the similitude among the time values obtained following the different methods, we conclude that we can indistinctly use both measures to gauge the dynamics of the liquid and glassy states.

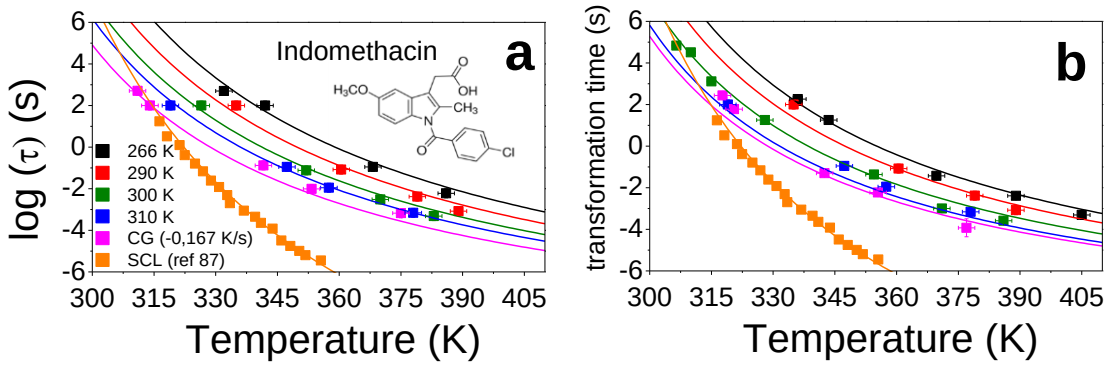

Figure 49. Comparison between the fitting of relaxation and transformation times using equation 24. Relaxation (a) and transformation (b) times of IMC glasses with different stability measured at different heating rates and structural relaxation time of supercooled IMC liquid from ref.[87]. The legend indicates the deposition temperature of the glass. The conventional glass (CG) has been obtained by cooling the liquid at 0.167 K/s. The fit parameters are shown in table 2 and 3.

It is relatively well established that molecular packing anisotropy is a common characteristic of many vapour-deposited glasses[47,48,50]. As seen in the previous chapter, the transformation of a vapour deposited glass into the SCL proceeds via a heterogeneous mechanism starting at surfaces/interfaces and the growth front velocity does not uniquely depend on the enthalpy content of the glass. In the previous Chapter, we concluded that the heterogeneous transformation of vapour-deposited thin film glasses of IMC could be divided into two families depending on the value of their birefringence, Δn. Glasses with large birefringence ($> |0.02|$) exhibit much larger growth front velocities compared to glasses with small birefringence ($< |0.02|$). Therefore, it is worth questioning whether anisotropy or molecular packing play any role in the homogeneous transformation of the glass into the supercooled liquid. The influence of molecular anisotropy may cast doubts on the use of equation 24 to simultaneously fit the liquid and glassy state, since this equation is a function of the enthalpy state of the glass, expressed through its limiting fictive temperature. Based on previous data[42], the glasses analysed here have $\Delta n \approx 0$, except those grown at 266 K with a low $\Delta n \approx 0.02$. We assume here that the dynamics of the system during the bulk transformation is affected by the same parameters that affect the front transformation. Therefore, the simultaneous fit of the various glasses and the liquid state, has been successful because those glasses behave as nearly isotropic from the point of view of the transformation into the SCL. In fact, attempts to include in Figure 48 IMC glasses which have been vapour deposited at lower temperatures (T_{dep} < 250 K) and have larger negative values of birefringence ($\Delta n < -0.02$) were not successful.

Interestingly, glasses of two very different families, molecular and metallic, can be adjusted using equation 24. The liquid-cooled Au-based metallic glasses measured in ref.[100] and shown in Figure 48c were aged for long times and equilibrated at two temperatures: 373 and 383 K, before being scanned up at fast heating rates using a Flash DSC. It is worth pointing out that beta relaxations are typically important in metallic glasses[8], and, in fact, according to ref.[100], short time aging of the Au-based glasses produced a simultaneous decrease of both T_{on} and T_f', in clear contradiction with equation 24. However, at the longer aging times needed for equilibration, the alpha relaxation time dominates over the beta relaxation and a decrease of T_f' is accompanied by an increase of T_{on}. It is however early to draw more general statements on the suitability of the proposed model for metallic glasses due to the scarcity of data in the high temperature regime. The popularisation of fast scanning methods will allow, in the years to come, testing the validity of VFT-type equations, such as equation 24, on a much larger range of materials. On the other hand, we are aware that a single fictive temperature value may not provide a unique description of the state of the glass[33,90]. However, our analysis suggests that a single enthalpic T_f' offers a reasonable description of the dynamics of the glass in the medium-to-high temperature regime. We assume that the behaviour observed here may be specific to glasses with a sufficiently narrow spatial distribution of inhomogeneities to allow for a single T_f' description of the glass. In more general cases, when this condition is not satisfied, the use of a non-Gaussian distribution of fictive temperatures into equation 24 may provide a better description of the glassy state.

Table 2. Fitting values using equation 24. τ refers to relaxation times calculated from $\tau_1\beta_1 = \tau_2\beta_2$ assuming τ_1 = 100 s for β_1 = 0.167 K/s, t_{trans} refers to transformation times. $\tau + t_{trans}$ refers to the fitting using all data. The data from the last line has been already shown in table 1.

Indomethacin		T_0 (K)	A (K^{-1})	B	τ_{g0} (s)	τ_0 (s)	D
Fitted data	τ	228.59	-0.107	45.62	1.91e-12	5.75e-23	21.16
	t_{trans}	229.86	-0.105	44.8	2.57e-12	1.07e-22	20.66
	$\tau + t_{trans}$	230.54	-0.106	44.93	2.69e-12	8.9e-23	20.55

Table 3. Values of limiting fictive temperature for IMC glasses resulting from the various fittings using equation 24 and equation 35 (see section 5.5) compared to nominal values, $T'_{f,\,nominal}$, obtained by integration of the heat capacity curves.

Indomethacin						
T_{dep} (K)			**266**	**290**	**300**	**310**
T_f' fit (K) (using eq. 24)	**Fitted data**	**τ**	284.5±1.5	293.3±1.2	303.7±1	309.3±1.2
		t_{trans}	284.9±1.4	293.6±1.5	303.9±1	309.4±1.1
		$\tau + t_{trans}$	285.2±1.4	293.8±1.4	304±1	309.6±1.1
T_f' fit (K) (using eq. 35)			285.4±1.1	292.5±1.1	301.4±1.1	307.8±1.4
$T'_{f,\,nominal}$ (K)			279±2.5	289±2.5	301±2.5	311.5±2.5
Toluene						
T_{dep} (K)			**111**	**113**	**116**	
T_f' fit (K)		**$\tau + t_{trans}$**	107.2±1.3	111.4±1.1	118.3±0.8	
$T'_{f,\,nominal}$ (K)			111±2.5	113±2.5	116±2.5	

5.3.1 Generalized strength factor

In light of the present analysis, we interpret ξ as a generalised strength factor, in analogy to the strength factor of liquids, D. In Figure 50 we represent equation 24 for IMC glasses with different stabilities, as a function of T_g/T. In analogy to Angell plots, where liquids of different kinetic fragility are represented[27], we observe that glasses with different stabilities behave, in this representation, as liquids with different fragilities. In the case of liquids, the larger the value of D, the lower the kinetic fragility and the softer the slope at $T_g/T = 1$. In the case of glasses, the more stable the glass, the larger the value of ξ and, therefore, the softer the slope. The generalised strength factor can be considered, therefore, as an extension of the strength factor D, where a dependence on the thermodynamic stability of the system has been included. Indeed, given the analogy between the expression for D in equation 29 and that of ξ, we can identify D as the strength factor of a glass with $T_f' = T_0$. Under this framework, when using D as the strength factor of an equilibrated liquid, one is considering the generalised strength factor of the most stable possible glass of that system, i.e. the ideal glass, under the assumption that $T_0 \simeq T_K$[27]. In this context, the significance of the fragility index of a liquid, m, closely related to D, gets linked to a particular thermodynamic state of the system and goes further from the conventional relationship between relaxation time and temperature at T_g. Moreover, the linear relationship between ξ and T_f' may be

indicative of a linear relationship between thermodynamic and kinetic fragilities[103]. In this sense, equation 24 represents a unified formalism to describe the relaxation behaviour of amorphous systems, whether in equilibrium or not. This finding is in close analogy to claims from previous reports where they measured the non-ergodicity factor in glasses by means of inelastic X-ray scattering (IXS) and found a certain correlation with the fragility of the liquid[44,104].

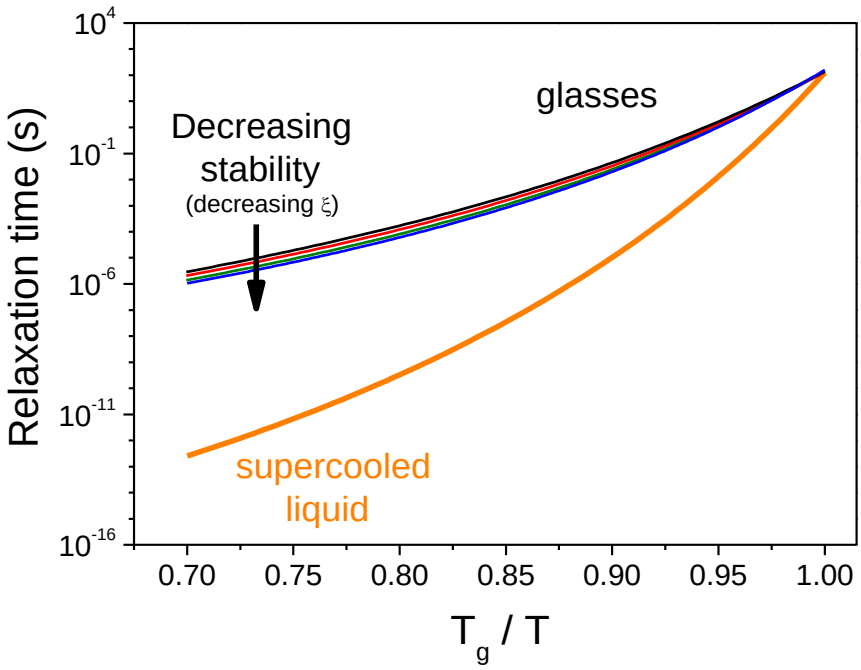

Figure 50: Comparison of the relaxation times of IMC glasses of different stabilities with the supercooled liquid in an Angell's type plot. Relaxation time of IMC glasses with different stabilities and IMC supercooled liquid as a function of the inverse of temperature multiplied by T_g, according to equation 24. T_g is considered as the temperature at which the relaxation time equals 100 s (analogously to what is commonly represented in an Angell's plot). The represented lines correspond to equation 24, using the obtained fit parameters (Table 1).

5.4 Arrhenius to super-Arrhenius transition

We argue that the generalization of the relaxation behaviour of disordered systems can also be extended to lower temperature ranges. If an Arrhenius relationship governs the dependence of glass relaxation time with temperature at lower temperatures, there must be a crossover point below which the glass relaxation time deviates from the observed super-Arrhenius behaviour shown in Figure 48. In fact, the transformation times of ultrastable IMC glasses into the supercooled liquid evaluated by Kearns et al. from isothermal measurements close to T_g[43] deviate

from equation 24, as shown by the up triangle symbols in Figure 51. Considering the alpha relaxation time of IMC at low temperatures reported by Pogna et al.[44], we realize, as represented in Figure 51, that: i) the experimental points can be fitted using the Mauro-Yue-Ellison-Gupta-Allan (MYEGA) model[105] in this low temperature range, and ii) there is a generalization of this MYEGA expression that can fit both liquid and glass relaxation time, analogously to what we have reported regarding the higher temperature range experimentally explored in this work,

$$\tau'_g = \tau'_{g0} e^{\frac{\xi' E_A}{RT} e^{C/T}} \quad (33)$$

where τ'_{g0} and C are constants, R is the universal constant of gases, E_A is an activation energy and $\xi' = A' + B'T_f'$ is the generalized fragility. As in the case of equation 24, all the parameters but T_f' are common for all glasses and the supercooled liquid.

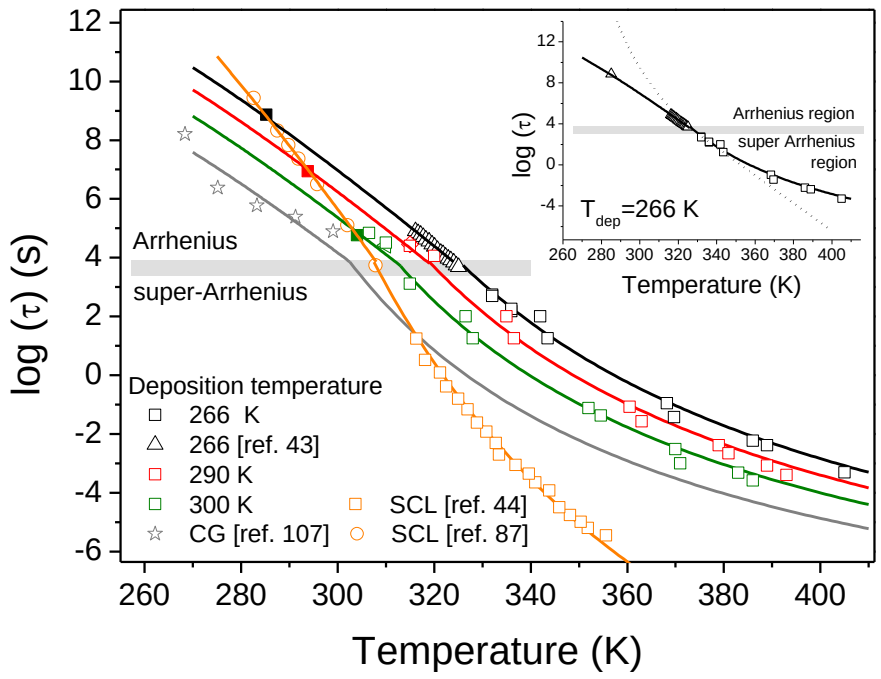

Figure 51. Relaxation time of IMC glasses with different stability and SCL as a function of temperature. Solid symbols lying on the SCL line (orange) are imposed under the consideration that, at each T_f', liquid and glass have the same relaxation time. The meaning of the rest of the symbols and colours is explained in the caption of figure 48a. The lines correspond to the simultaneous fitting of all represented points using equation 24 for the Arrhenius region and equation 33 for the super-Arrhenius region. The horizontal grey line broadly represents the relaxation time value at which the kinetic transition from Arrhenius to super-Arrhenius takes place. Data corresponding to the conventional glass are obtained from ref.[107]. In the inset, we remark the divergence of both regimes at the indicated value of tau.

Roland[106] pointed out that molecular liquids and polymers presented a series of dynamic "transitions" at certain fixed values of the relaxation time, regardless of the temperature. Here, in the light of the results presented in Figure 51, we note that the invariance can be extended to glassy systems, meaning that both glasses with different thermodynamic stability and the equilibrium supercooled liquid transit from one regime to another at comparable values of the relaxation time regardless of the temperature. This transition broadly occurs at relaxation times of about 10^2-10^4 s, independently of the stability. This fact reinforces the idea that the liquid and glass state can be understood under the same theoretical framework.

5.5 Superposition of relaxation times

Based on the density scaling relationships reported for supercooled liquids at variable temperature and pressure[94,96,108], we study the density scaling relationships of relaxation times of liquid and glasses with different thermal stability. In order to this study, we need to incorporate the effect of stability on the density of the glass. In the case of the supercooled liquid, $\rho(T)$ is only function of the thermodynamic temperature. The density of the conventional IMC glass at ambient conditions is 1.31 g/cm^3 [45]. As ambient conditions, we consider atmospheric pressure and a temperature of 293 K. The densities of indomethacin glasses with different stabilities are calculated as explained in Figure 52 from the density variations measured at 293 K reported by Dalal et al.[42]. The variation of density with temperature has been calculated from the reported thermal expansion coefficients, $\alpha_{UG} = 1.39 \cdot 10^{-4}\ K^{-1}$, $\alpha_{CG}(T_g = 309\ K) = 1.33 \cdot 10^{-4}\ K^{-1}$ and $\alpha_{SCL} = 5.69 \cdot 10^{-4}\ K^{-1}$ [42],

$$\rho(T, T_f) = \frac{\rho_0(T_f', T_{ref})}{1+\alpha_T(T_f')(T-T_{ref})} \quad (34)$$

where $\rho_0(T_f', T_{ref})$ is a reference value of density for a glass with T_f' or a liquid, measured at T_{ref} and $\alpha_T(T_f')$ is the thermal expansion coefficient of the same system.

For intermediate stabilities, a linear interpolation between the expansion coefficient value of ultrastable and conventional glasses has been performed. The density and expansion coefficients corresponding to the nominal T_f' of the samples used in this experiment are shown in Table 4. The reference density of supercooled IMC has been chosen to be equal to the density of the conventional glass, T_f' = 315 K, at T_{ref} = 315 K.

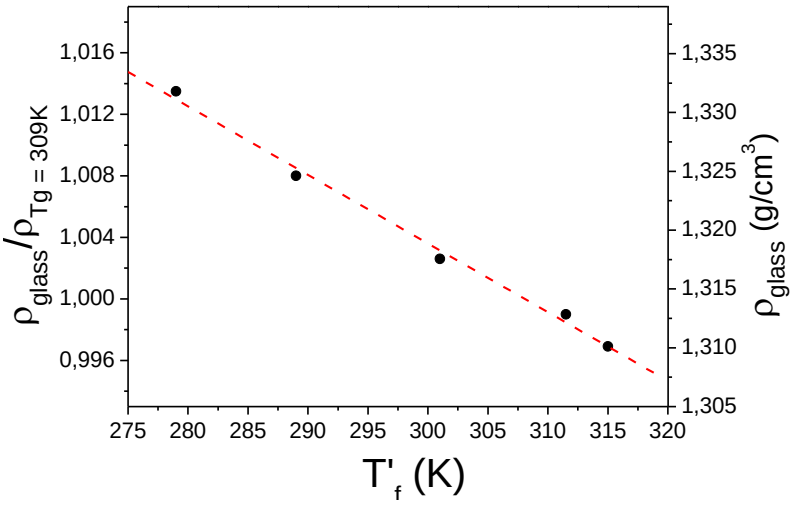

Figure 52. Density of IMC glasses with different stabilities measured at 293 K (extracted from ref.[42]). In the left axis, data is represented with respect to the density of a glass cooled at 1 K/min (T_f' = 309 K), as shown in reference [42]. Right axis has been stablished after the consideration that the density is 1.31 g/cm^3 for T_f' = 315 K (conventional glass). We assume a linear relation between the density of the glass and its limiting fictive temperature.

Table 4. Values of density and thermal expansion coefficients used for each glass and for the supercooled liquid in equation 34 to construct Figure 52.

$T'_{f,nominal}(K)$	ρ_0 $\left(\frac{g}{cm^3}\right)$ at 293 K	$\alpha_T(K^{-1})$ x 10^{-4}
279	1.332	1.39
289	1.325	1.374
301	1.318	1.354
311.5	1.313	1.33
315 (SC -10 K/min)	1.31	1.32
SCL	1.307 (at 315 K)	5.69

In Figure 53 we represent our relaxation data as a function of $1000\rho(T,T_f')^{\gamma}/T$, where $\rho(T,T_f')$ is the density of the system calculated as a function of the thermodynamic and the limiting fictive temperature. The value of the exponent gamma is set to $\gamma = 9.5$. We note the reasonable superposition of all the represented data, which includes both IMC glasses with different stabilities and the supercooled liquid.

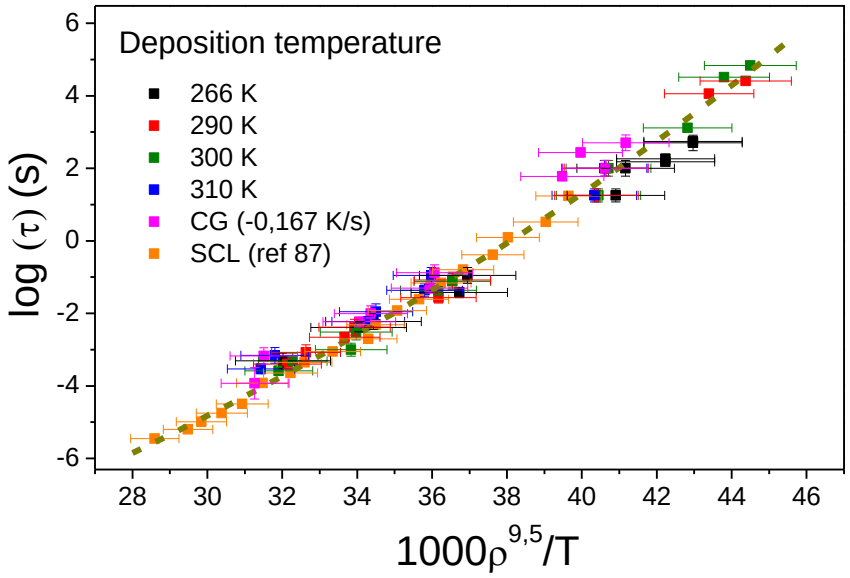

Figure 53. Scaling relationship of the relaxation time of glasses of IMC with different stability and of the supercooled liquid as a function of $1000\rho(T,T_f')^{\gamma}/T$. The best superposition of the data is obtained with $\gamma = 9.5$.

Different values of conventional IMC glass density at ambient conditions have been reported[109]. However, it should be noted that while the choice of a different reference value of density shifts the data towards lower or higher values of Tv^{γ}, it does not appreciably change the scaling factor. Typical values of γ for a variety of materials range from $3<\gamma<9$ [108], so our value lies at the upper limit. Unfortunately, there are no reports of Pressure-Volume-Temperature measurements in indomethacin that would allow the comparison of our exponent to other data.

The observed superposition of relaxation times indicates that, analogously to the behaviour of liquids at different pressure and temperature, there must be an expression that relates relaxation time with the product Tv^{γ}. Casalini et al. derived an expression, $\tau_{\alpha}(T,\rho) = F(Tv^{\gamma})$, considering that the relaxation time of supercooled liquids is governed by the entropy of the system, S_c, as the Adam-Gibbs model proposes, but using a generalised equation for S_c that takes into account the influence of both temperature and also pressure (or, equivalently, changes in specific volume)[95]. In particular,

$$\tau(T,v) = \tau_0 \exp\left(\frac{C}{Tv^{\gamma_G}}\right)^{\phi} \qquad (35)$$

where τ_0 and ϕ are constants and $C = \ln\left(\frac{100}{\tau_0}\right)^{\frac{1}{\phi}} T_g v_g^{\gamma_G}$, with T_g the conventional value of glass transition temperature for IMC and v_g the specific volume of a conventional glass at this

temperature. This expression correctly fits experimental data of the relaxation time of supercooled liquids at different temperatures and pressures[95]. As in the case of the scaling relation, in order to apply this model to glasses with different stability, we substitute the effect of pressure on specific volume by that of glass stability and express v as $v(T, T_f')$. The experimental data shown in Figure 48 have been simultaneously fitted using equation 35, setting free the parameters τ_0, ϕ, γ_G and the values of T_f'. The results are plotted in Figure 54. The best fit is obtained by considering $\tau_0 = 7.59 \cdot 10^{-14}$ s, $C = 168.58\ K \cdot cm^3/g$, $\phi = 1.96$, and $\gamma_G = 9.1$. The values of the limiting fictive temperature extracted from the fit are in fair agreement with the nominal values (see Table 3). We have also obtained very similar values for the exponents γ and γ_G. Although the identification of the scaling exponent γ with γ_G is not trivial, they are often considered to be equivalent[96]. Specifically, the scaling parameter can be identified with the Grüneisen parameter and it is connected to other properties, such as expansion coefficient or heat capacity[95]. The possibility to infer γ from measurements at ambient pressure, in the liquid and glassy states, is promising.

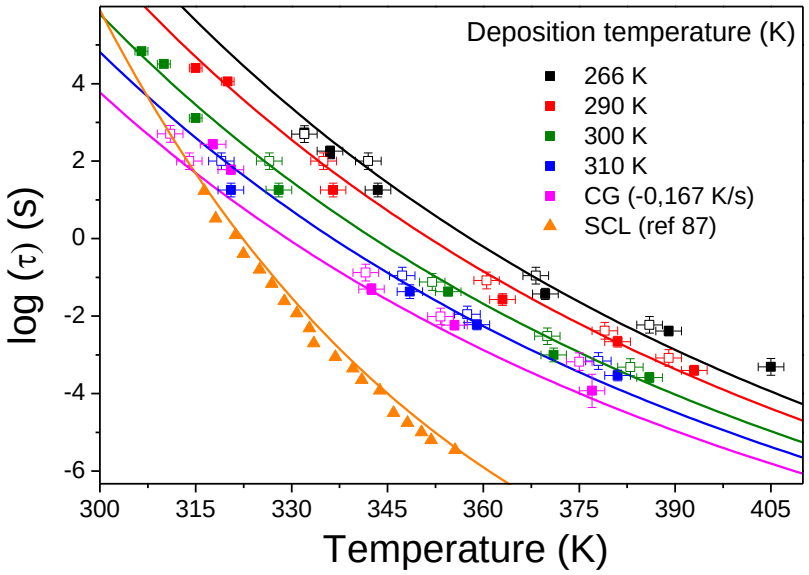

Figure 54. Scaling relationship of the relaxation time of glasses of IMC with different stability and of the supercooled liquid as a function of temperature. The meaning of the different symbols and colours is explained in the caption of figure 48a. The continuous lines are the best fit of the experimental points using equation 35 and $\rho(T, T_f')$. The parameters τ_0, ϕ and γ_G are allowed to adjust freely.

These findings support the idea that the dynamical behaviour of liquids and glasses can be explained and analysed under the same theoretical framework. Surprisingly, even the most stable glass, grown at $T_{dep} = 266\ K$, where hydrogen bonding between molecules may be more abundant[110], is reasonably well fitted by equation 35, although some deviation is present at high temperatures.

The fact that IMC glasses and liquids obey similar density scaling relations points out that there must be two relevant parameters controlling the dynamics of both the liquid and the glassy state: temperature and density. The correlation between density and limiting fictive temperature in IMC glasses was already shown in the previous chapter. Therefore, it is not surprising that both methods, one using temperature and the limiting fictive temperature as the main variables for the VTF-like description of the relaxation times and the other using temperature and density (volume), provide comparable results in terms of a unifying perspective of a glass and its supercooled liquid.

5.6 Chapter summary

While large amounts of experimental data support the theories that describe liquids, results concerning the dynamics of glasses are scarce due to experimental difficulties. Using ultrafast scanning calorimetry, we expand the accessible timescales to much shorter values than previously achieved. We use relaxation data from glasses of different stability and from the supercooled liquid to propose a common description for both states. Our data shows that the relaxation time of glasses follows a super-Arrhenius behaviour in the explored temperature range. Surprisingly, both liquid and glassy states can be described by a common VFT-like expression that solely depends on thermodynamic and limiting fictive temperature. The fragility index calculated from the fitting of the experimental data using the proposed unifying model is in fair agreement with reported data for three different systems. Our observations are also compatible with the observed Arrhenius behaviour of glasses at low-temperature. Indeed, if supercooled liquids show an Arrhenius to super-Arrhenius transition at low temperatures, as has been recently claimed[44,111], a joint description of the relaxation dynamics of liquids and glasses would imply that this transition is also present in glasses.

We also show that the dynamics of IMC glasses obey density scaling laws which were derived for the liquid state, suggesting that the dynamics of glasses and liquids can be described by the same two factors, i.e. temperature and density. However, while changes in liquid density are

experimentally regulated by changes in temperature and pressure, density of glasses can be regulated by temperature and thermodynamic stability.

These findings provide a new framework that permits the understanding of both liquids and glasses from a joint perspective and could pave the way to a clearer connection between thermodynamic and dynamic parameters of a given system.

We note that all glasses considered in this chapter have nearly random molecular orientation, i.e. $\Delta n \approx 0$. As we saw in the previous chapter, molecular orientation plays a role in the dynamics of the glass and, therefore, the limiting fictive temperature does not univocally determine the behaviour of the glass. However, we also see that, under the light of the presented results, the limiting fictive temperature can be apparently used to correctly describe the dynamics of a glass with random molecular orientation.

6. EFFECT OF PRESSURE ON ULTRASTABLE GLASSES

6.1 Chapter introduction

While the properties of the glass transition temperature have been deeply studied as a function of temperature by calorimetry in many different glasses, the pressure dependence of the calorimetric glass transition is a subject relatively little explored[108]. The main reason can be attributed to experimental difficulties, in relation to applying high pressures in calorimetric experiments. On the contrary, dielectric or Pressure-Volume-Temperature measurements are more abundant and permit to broadly infer several tendencies with respect to molecular interactions[87,112]. For instance, it has been found that glasses with strong molecular interaction of hydrogen bonding type, systematically show lower values of dT_g/dP compared to glasses dominated by van der Waals forces[108,113–115]. Another universal feature of glasses is that over a sufficiently large pressure range the pressure dependence of T_g is non-linear, i.e. the effect of pressure on temperature weakens when pressure increases and can be adjusted with the empirical Andersson-Andersson equation[116],

$$T_g = \kappa_1 \left(1 + \frac{\kappa_2}{\kappa_3} P\right)^{1/\kappa_2} \tag{36}$$

In parallel, Davies and Jones derived, based on the Ehrenfest equations, two expressions for dT/dP in the liquid state evaluated at T_g[117]. The following expression has been found to describe a large range of materials[115]:

$$\left.\frac{dT}{dP}\right|_{T_g} = \frac{T_g \cdot v \cdot \Delta\alpha}{\Delta C_P} = \frac{T_g \cdot v \cdot (\alpha_{liq} - \alpha_{glass})}{(C_{Pliq} - C_{Pglass})} \tag{37}$$

where Δk and $\Delta\alpha$ refer respectively to the difference in isothermal compressibility and isobaric expansivity at T_g, between the liquid and its corresponding glass, v is the molar volume and ΔC_p the differential heat capacity evaluated at T_g.

In the previous chapter, we developed an empirical model that could simultaneously describe the relaxation time of the liquid and of glasses of different stability. The model was built with data taken at ambient pressure and therefore only depends on temperature and density. What would be the effect of pressure? Can we explain the new data measured as a function of pressure introducing a density dependence on pressure? We present in this chapter measurements of the glass transition as a function of pressure together with an extension of our previous empirical model that aims to describe the relaxation dynamics of the system as a function of temperature and pressure by considering the dependence of density on these variables.

6.2 Evolution of the onset of devitrification as a function of pressure

High pressure measurements of the glass-to-liquid transformation were carried out at the Group of Characterization of Materials (GCM) of the Universitat Politècnica de Catalunya (UPC). The high-pressure calorimetric signal was recorded in a home-made Differential Thermal Analyser (DTA) setup[59], explained in detail in chapter 3. Two sets of indomethacin samples, 20-40 μm thick ultrastable glasses with T_f' = 280 K, and conventional glasses with T_f' = 315 K, were temperature-scanned at pressures ranging up to 300 MPa. Conventional glasses were obtained by cooling the liquid at 2-10 K/min. The calorimetric curves obtained at different pressures, for both ultrastable and conventional glasses, are shown in Figure 55. It is apparent for both glasses how the onset of devitrification shifts to higher temperatures as pressure increases.

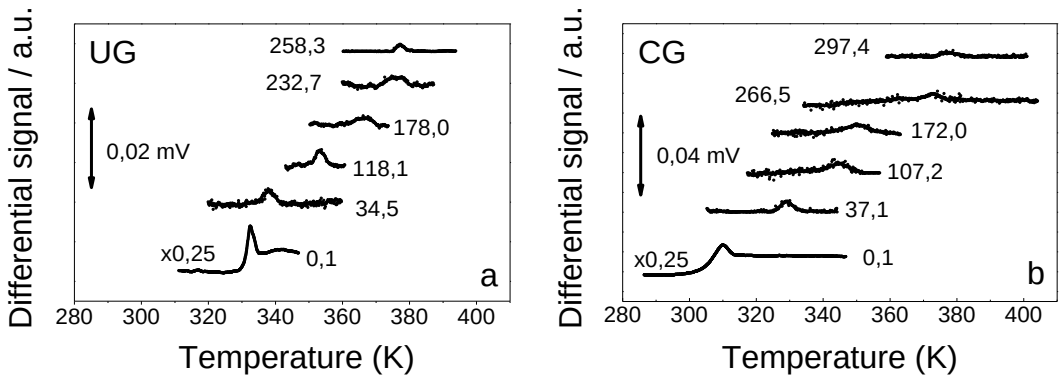

Figure 55. Differential DTA signal as a function of temperature for different pressures, measured at 2 K/min. a) Ultrastable IMC glass grown from the vapour phase at a substrate temperature of 0.85T_g. b) Conventional glass formed by cooling the liquid at 2 K/min. The curves have been shifted for clarity.

Besides possible pressure effects, the shape and the smaller overshoot of the DTA signal at the glass transition for pressures above 0.1 MPa are due to the lack of sensitivity of the HP-DTA setup, precluding a proper evaluation of the limiting fictive temperature as a function of pressure. We will, therefore, concentrate the analysis on the evolution of the onset of devitrification, T_{on}, as a function of pressure for both types of glasses. The extracted T_{on} data is shown in Figure 56. As observed in many other substances, mainly polymers, dT_g/dP is mostly linear up to a certain pressure and from this point, the slope becomes much softer[108,118]. This effect was already predicted by DiMarzio from entropic considerations on the glass transition[119]. However, as noted by Angell et al., this change of regime could also originate from the dissimilar pressure dependence of the difference in isobaric expansion coefficient, $\Delta\alpha$, and heat capacity, ΔC_P[118], which would yield a non-linearity of dT_g/dP (equation 37). The T_{on} vs. pressure data has been

fitted using equation 36 (dashed lines). $(dT_{on}/dP)_{Patm}$ evaluated at P=0.1MPa yields a value of 280 ± 22 K/GPa, in relatively good agreement with previous experimental data by Wojnarowska et al. using dielectric spectroscopy[87] that measured 254 K/GPa (black circles in Figure 56). This value suggests that van der Waals interactions dominate over hydrogen bonding, as typically found in polymers and other van der Waals glass-formers[108,115]. The slope of the ultrastable glass at P=0.1 MPa is 201 ± 24 K/GPa, approximately 30% lower than the value obtained for conventional IMC glass. This may be an indication of the existence of a higher degree of strong intermolecular interactions, such as hydrogen bonds, compared to conventional IMC, a tendency already reported in other works[110,120].

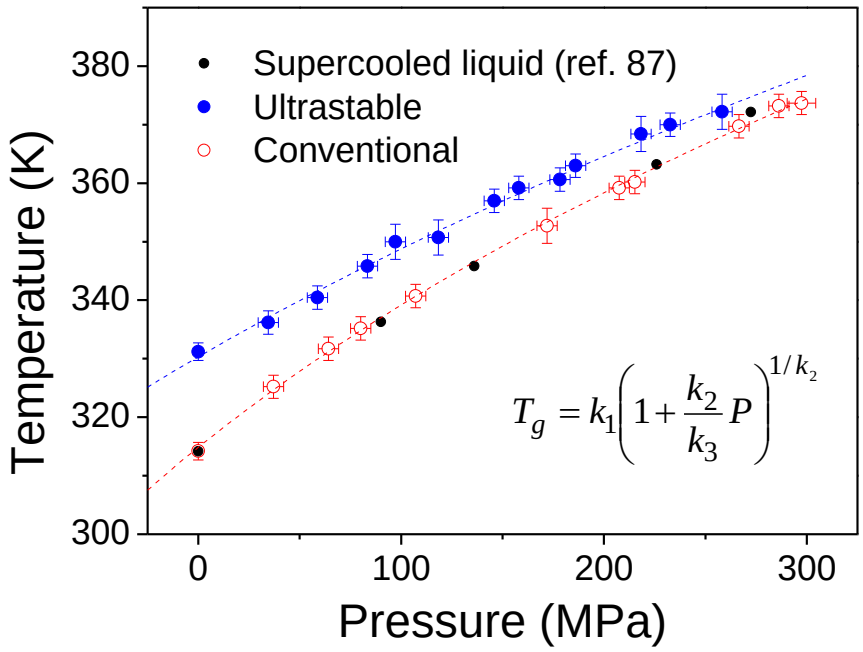

Figure 56. Onset of devitrification temperature versus pressure for IMC ultrastable (blue) and conventional (red) glasses, obtained from the calorimetric data shown in Figure 55. The experimental data have been fitted using equation 36 (dashed lines). _The parameters are k_1=314.85, k_2=4.68 and k_3=1124 for the conventional glass and k_1=330.31, k_2=4.012 and k_3=1637 for the ultrastable glass.

The experimental value of $(dT_{on}/dP)_{Patm}$ for the conventional glass agrees remarkably well (within 3%) with the one calculated from equation 37 using available data from literature for glass and liquid specific volumes, thermal expansion coefficients and heat capacity jump (Table 5). However, the agreement is unsatisfactory in the case of the ultrastable glass, whose experimental dT_{on}/dP value deviates about 25% from the predicted using equation 37.

Table 5. Experimental data and parameters used to test the validity of the Davies-Jones relation, equation 37.

Parameter	UG	CG
T_{on} [K] at P=0.1 MPa	332	311
T_f' [K] at P=0.1 MPa	282	312
$\Delta\alpha$ [K^{-1}]	$4.30 \cdot 10^{-4}$ [42]	$4.36 \cdot 10^{-4}$ [42]
ΔC_P [J/molK]	150.74 (at 332K) 167.37 (at 282K)	138.23
v_m [cm^3/mol]	269.62[42]	273.12[42]
$(dT_{on}/dP)^{experimental}$ [K/GPa]	201	280 254[87]
$(dT_{on}/dP)_{extrapol\ 300\ MPa}$ [K/GPa]	133	148
$(dT_g/dP)_{calculated}$ [K/GPa]	255	271

Equation 37, derived from the Ehrenfest equation that is valid for a second-order phase transition, describes the temperature variation of the supercooled liquid with pressure to maintain the system at equilibrium. This expression is evaluated at the glass transition temperature. It is reasonable to ask whether this equation should remain valid using the onset of the devitrification temperature measured on heating, T_{on}, instead of T_g on cooling, as considered in equation 37. For the conventional glass this difference is relatively small since cooling/heating is done at comparable rates, which means $T_{on} \approx T_g \approx T'_f$. However, ultrastable glasses are somehow equivalent to glasses cooled at extremely low cooling rates leading to $T_{on} > T_g$ and, therefore, at the heating rates imposed in the presented measurements, the system is clearly far from thermodynamic equilibrium.

Interestingly, extrapolation of the Andersson-Andersson function (equation 36) to higher pressures seems to yield a completely different scenario where both UG and CG data converge, exhibiting the same T_{on} and Ton vs. P dependence. The dynamics and the thermodynamic state of vapour-deposited ultrastable glasses are clearly different with respect to conventional glasses, cooled from the liquid. The different onset of the calorimetric glass transition temperature and the different value of the limiting fictive temperature at P=0.1 MPa for UG and CG can be related to the change of the energy barriers between meta-basins and their different energy position in the energy landscape respectively. At ambient pressure the difference in onset of devitrification is 20 K, while at higher pressures the onset of devitrification seems to coincide for both UG and CG. At this pressure both glasses transform into the SCL at the same temperature. Since the relaxation time of the system equals 100 s at the transformation temperature, $T_{on,CG} = T_{on,UG}$ implicitly means

that they share a common relaxation time at that temperature. This is a dramatic change, since at ambient pressure and temperature the variation in relaxation times for both glasses was 4-5 orders of magnitude, as seen in Chapter 5.

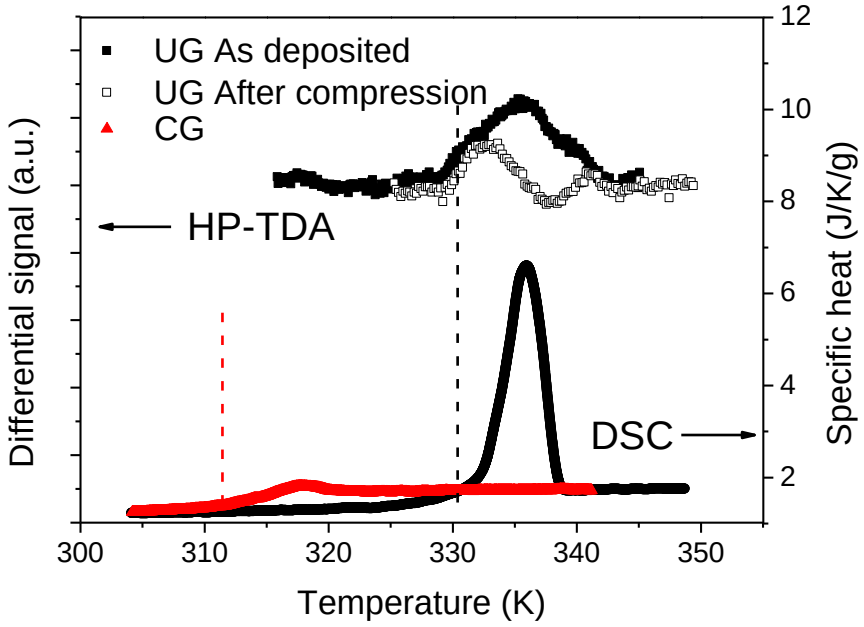

Figure 57. Upper curves: HP-DTA curves, showing the differences between an ultrastable IMC glass submitted to 300 MPa (black open symbols) and another without any pressure treatment (black solid symbols), both of them measured at ambient pressure and at 2 K/min. Differences in the shape of the after-compression signal could be attributed to technical reasons. Lower curves: DSC scans from a conventional IMC glass, cooled from the liquid at 2-10 K/min (red curve) and from an ultrastable glass (black curve), both measured at ambient pressure.

Unfortunately, the experimental setup does not permit an accurate evaluation of the limiting fictive temperature at high pressures and therefore precludes the finding of a direct relation between T_f' and pressure. However, we can use previous high pressure experiments on conventional glasses to infer a plausible relation between our T_{on} data and glass stability as a function of pressure. Most of the prior measurements at high pressure have only access to dynamic properties of the system and the resulting information is not directly connected to the thermodynamics of the glass itself. We tentatively assume that a change of pressure, in the limited range explored in this work, should not have a considerable effect on the stability of the glass. However, to test whether a pressure change leads to irreversible changes in the structure of the glass we carried out an additional experiment. The methodology consisted on exposing a UG glass to a pressure of 300 MPa at room temperature. We then returned the glass to ambient pressure to subsequently perform a temperature scan. Figure 57 shows the calorimetric curves for a pressurized and an unperturbed glass measured at ambient pressure in the pressure-DTA setup.

As has been mentioned before, the sensitivity of this setup is rather limited and the shape and area of the transition peaks are not reproducible. Furthermore, the effects of pressure on the container crucible may yield variations in some features of the transition peak. However, the onset of the transition is indeed accurate and, as can be seen in the figure, both glasses show the same onset. Moreover, when comparing these two curves to measurements performed in a DSC (lower curves) on a UG glass, we can see how the onset of the transition is exactly the same. This is by no means obvious since, according to the values of compressibility reported in the literature[45], a pressure of 300 MPa should change the volume of the glass by ~4%.

6.3 Glass relaxation time as a function of pressure

In chapter 5, we concluded that the relaxation times of glasses with different stability, as well as the supercooled liquid, can be jointly described by an expression that depends on the temperature and density of the system (equation 35). The proposed model was applied to data obtained at ambient pressure, as were all the relations used for the parameters of the model, such as the dependence of density on temperature. We suggest that the same model can be applied to the data presented in this chapter by introducing in the equations the density dependence on pressure.

According to the Murnaghan equation of state[121], the bulk modulus of a system, K_T, can be expressed as a linear function of pressure,

$$K_T = K_0 + K_1 P \tag{38}$$

where K_0 is the bulk modulus at ambient pressure and K_1 describes the variation of K_T with pressure. The dependence of K_T on temperature is typically small and is considered as a small perturbation at very high pressures[122]. Since the pressure values imposed in this work are relatively low, we will consider the bulk modulus to be constant in relation to temperature changes. Integrating the expression for the isothermal bulk modulus, $K_T = -V\left(\frac{dP}{dV}\right)_T$, and using eq. 38, the specific volume of a system can be expressed as a function of pressure. The density, inverse of the specific volume, takes the following form,

$$\rho(P) = \rho_0 \left(1 + P\left(\frac{K_1}{K_0}\right)\right)^{\frac{1}{K_1}} \tag{39}$$

In chapter 5 we only considered the effect of temperature in the calculation of density (equation 34). Introducing the effect of pressure given by 39, we obtain

$$\rho(T,P) = \frac{\rho_0\left(1+P\left(\frac{K_1}{K_0}\right)\right)^{\frac{1}{K_1}}}{1+\alpha(T-T_{ref})} \quad (40)$$

The variation of the thermal expansion coefficient with pressure is related to the variation of the bulk modulus with temperature as $\left(\frac{d\alpha}{dP}\right)_T = \frac{1}{K_T^2}\left(\frac{dK_T}{dT}\right)_P$. Since the dependence of K_T with temperature is small compared to K_T, we consider $\left(\frac{d\alpha}{dP}\right)_T$ to be negligible. We also note that we have considered no dependence of the thermal expansion coefficient of temperature.

We show in figure 58 reported values from Paluch et al. of relaxation time for IMC supercooled liquid taken at different temperatures and pressures[87]. We use these data to infer the values of K_0 and K_1 for the supercooled liquid by fitting the curves using equation 35 and 40.

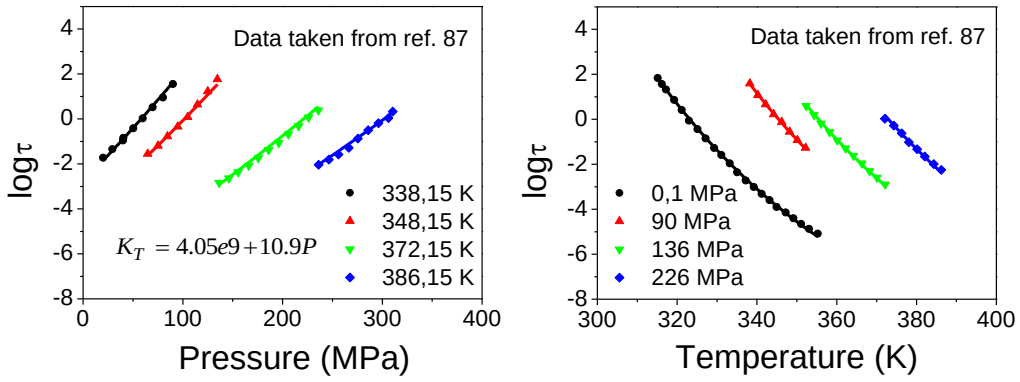

Figure 58. Relaxation time of supercooled IMC liquid extracted from ref[87] at a) different temperatures and b) different pressures. Data are fitted using equation 35 (chapter 5) introducing the dependency of density on pressure described by equation 40. All parameters appearing in equation 35 are taken from section 5.5. Only the bulk modulus has been allowed to adjust, yielding $K_T = 4.05e9 + 10.9P$.

The fit of the data yields a value of $K_T = 4.05e9 + 10.9P$ for the bulk modulus of IMC supercooled liquid. In order to infer the value of $K_T(P)$ for glasses of different stability we use the adiabatic bulk modulus reported by Ediger et al. at ambient pressure[45]. The adiabatic bulk modulus and the isothermal bulk modulus can be related by $K_S = K_T(1 + \gamma_G \alpha_P T)$[122], where α_P is the thermal expansion coefficient and γ_G is the Grunesein parameter. For the present analysis, we use the value of gamma obtained after fitting our relaxation data using equation 35, as shown in section 5.5, $\gamma_G = 9.1$, what yields the values of $K_{0,CG} = 5.84e9$ Pa and $K_{0,UG} = 6.58e9$ Pa for the bulk modulus of CG and UG at atmospheric pressure respectively. As we commented in the previous Chapter, the exact identification of the Grüneisen parameter with a particular set of thermodynamic parameters is still under discussion[96]. However, there is considerable agreement

with the idea that this parameter and the scaling factor, found to be 9.5 from the data shown in Chapter 5, are approximately coincident. Since these data have been measured at ambient pressure, no information regarding K_1 can be derived. We will consider, as a preliminary tentative scenario, that K_1 remains unaltered after vitrification and, therefore, glasses and liquid have the same K_1 value. By introducing the dependence of density on pressure in equation 35, we can infer the relaxation time of glasses as a function of temperature and pressure, $\tau_g(T, P)$, as will be shown at the end of the chapter. The temperature at which $\tau = 100$ s is considered as the onset of devitrification. We have plotted these temperatures in Figure 59a for the conventional and ultrastable IMC glass for different values of pressure. We find that, under the assumption of invariant K_1, the onset of devitrification of conventional and ultrastable glasses do not seem to converge at high pressures, contrary to our experimental results. Therefore, it seems fair to think that i) the bulk modulus of glass and liquid respond differently to pressure changes and ii) that this response depends on the stability of the glass. Considering the inferred values of K_0, we speculate that the value of K_1 follows the same tendency. Assuming $K_{1,CG} = 32$ and $K_{1,UG} = 90$, we can satisfactorily describe the evolution of the onset of devitrification with pressure for different glasses, using equations 35 and 40, as can be seen in Figure 59b.

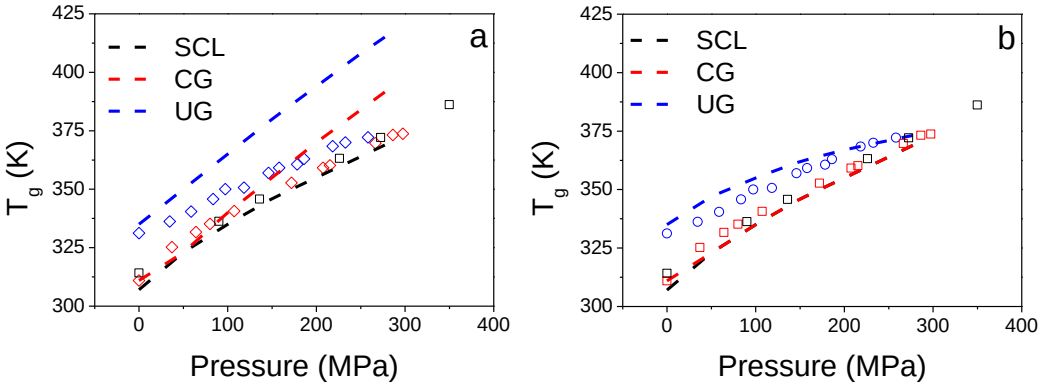

Figure 59. Comparison between experimental data of T_g as a function of pressure for UG and CG (open symbols) and values predicted using equation 35 (dashed lines), taking a) K_1 constant $K_1 = 10.9$ and b) system-dependent value of K_1, $K_{1,CG} = 32$, $K_{1,UG} = 90$, $K_{1,SCL} = 10.9$. The values of K_0 used in the two plots are $K_{0,SCL} = 4.05e9$ Pa, from the fitting shown in Figure 58, and $K_{0,CG} = 5.84e9$ Pa and $K_{0,UG} = 6.58e9$ Pa, from the expression $K_S = K_T(1 + \gamma\alpha_P T)$.

Under the framework developed in the previous chapter, the experimental data shown in Figure 56 would depict a scenario in which relaxation dynamics of glasses with very different stabilities, as can be a glass produced cooling at 10 K/min and another one aged for millions of years, have equivalent relaxation dynamics at sufficiently high pressures. A representation of this scenario is

given in Figure 60. In other words, high pressure would make, from an experimental point of view, different glasses practically undistinguishable.

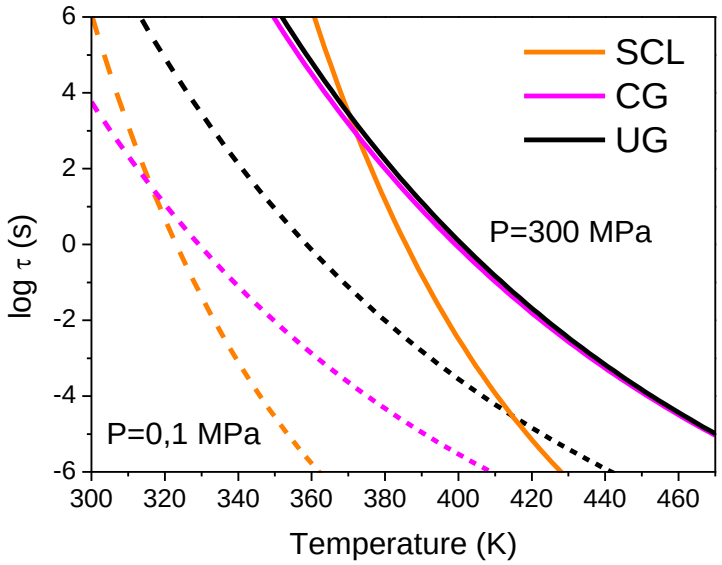

Figure 60. Scheme of the relaxation time of IMC SCL, CG and UG at ambient pressure (dashed lines) and at 300 MPa (solid lines) under the assumptions explained in the text. At 300 MPa, the difference between glasses of very different stability has practically vanished.

Although more data is necessary in order to identify the specific dependence of density with pressure, the analysis developed here permits us to tentatively extend the unified relaxation time model to include the influence of pressure. According to the model described by equation 35, $\tau(T,v) = \tau_0 \exp\left(\frac{C}{Tv^{\gamma_G}}\right)^{\phi}$, the relaxation time of glasses of different stability would converge at very high temperatures towards a value given by τ_{0g}. The analysis presented in this chapter, would indicate that, in an analogue manner, the relaxation time of glasses of different stability will converge in the high pressure limit.

6.4 Chapter summary

We have analysed the pressure dependence of the glass-to-liquid transformation in two glasses of indomethacin that have extremely different values of limiting fictive temperature, ΔT_f' = 30 K. The two glasses show a different dependence of the glass transition temperature on pressure when evaluated close to atmospheric pressure. This variation could be related to the differences in packing and molecular binding of the two glasses. Interestingly, extrapolation to very high pressures, would show that both glasses share the same onset temperature and the same $(dT_{on}/dP)_{Patm}$. Preliminary results show an invariance of the onset temperature of ultrastable

glasses before and after submitting the sample to high pressure, an indication that pressure would not affect the stability of the glass.

We extend the joint description of relaxation dynamics of glasses and liquids, including a particular pressure dependence of the glass and liquid density induced by the bulk modulus of the system, $K_T = K_0 + K_1 P$, where K_0 is the isothermal bulk modulus at ambient pressure and $K_1 = \frac{dK_T}{dP}$. Under this assumption, we find that the measured experimental data can be satisfactorily described considering a system-dependent value of K_1, i.e. different glasses and liquids have different values of K_1. While further experiments are required to corroborate this assumption, its verification would imply that i) we can extend our relaxation time generalization, at least qualitatively, to variations of pressure by assuming a particular dependence of density on pressure and ii) the bulk modulus of glasses with different stability and the liquid would be differently affected by pressure.

According to the unified description of glass dynamics, the relaxation time of glasses at high pressure converge towards a unique value, in analogy to the effect of temperature on glasses with different stability, that converge to a unique value of relaxation time, τ_{0g} at high temperatures.

7. INFLUENCE OF STABILITY ON CRYSTALLIZATION AND WATER ABSORPTION

Part of this Chapter appears published in The Journal of Non-Crystalline Solids, 407 (2015), 256-261.

7.1 Chapter introduction

Organic molecular glasses are of special interest for the pharmaceutical industry, since the particular morphology of the glass, halfway between the liquid and the crystal, shows a remarkable enhanced bioavailability[5] and solubility with respect to the crystalline counterpart[6,123]. However, the limited stability of the amorphous compounds hinders widespread commercialization. The amorphous state has higher energy than the crystalline state and the glass may undergo crystallization during processing, storage and use of the product. The resistance against crystallization is a critical aspect to be explored in stable glasses, since, from an industrial point of view, crystallization may be considered the major drawback in the commercial use of glassy systems in general. For instance, the development and approval of new pharmaceutical products are seriously compromised if glasses undergo crystallization during the periods of use, handling or storage. Some materials, such as Celecoxib, an anti-inflammatory drug widely used as a pharmaceutical product, is known for its poor ability to form a glass and its high tendency towards crystallization[6], and different methods to diminish this effect are continuously under investigation[6,57,124,125]. As commented in previous chapters, physical vapour deposition of organic molecules permits the production of glasses with remarkable properties when compared to the conventional glass[37,39,49]. The successful preparation of ultrastable glasses of celecoxib with an associated decrease of the growth rate of the crystalline phase would signify an important advance for the pharmaceutical industry and could be the basis of a new generation of pharmaceutical drugs.

From a thermodynamic point of view, the crystal is the most stable phase, what explains the inherent tendency of a glass to crystallize. Moreover, certain conditions can promote crystallization in the glass, being the presence of water one of these triggering agents[126,127]. The enhanced molecular mobility due to the presence of water molecules in the glass is believed to be the responsible for the increase in crystallization rate[120,128]. Also, the plasticizer effect of absorbed water induces an earlier transformation into the supercooled liquid, several degrees below the

glass transition of the equivalent anhydrous glass[120]. Indomethacin, even being a hydrophobic compound in its crystalline phase[129], is strongly affected by water absorption in its glassy form. Zografi et al. reported, for IMC conventional glasses, the diminution on the glass transition after water absorption[120]. They found that, as a rough estimation, the onset of the transformation shifted 10 K towards lower values per 1% water concentration in weight. Besides, water absorption depends on the properties of the glass. Ediger and co-workers have shown that ultrastable glasses of indomethacin absorb considerably less water and that the amount of absorbed water clearly depends on the stability of the glass[110]. It has been suggested that the strong hydrogen bonds in ultrastable IMC glasses prevented water molecules to strongly attach to the material. Unfortunately, the same mechanism that increases the resistance of stable IMC towards water absorption, may decrease its solubility in water. The study of the effect of stability on water may help to understand the mechanism responsible for stability degradation and crystallization-inducement effect and find a compromise between water absorption and solubility.

7.2 Ultrastability and crystallization of a poor glass-former compound

7.2.1 Thermal and structural characterization

7.2.1.1 Kinetic and thermodynamic stability

Indomethacin is a good glass former that has been extensively studied by the glass and pharmaceutic community. On the contrary, other compounds, such as Celecoxib (CXIB), crystallize easily, precluding the formation and conservation of the glassy phase. In order to test the capability of CXIB to produce vapour deposited stable glasses, we prepare 1-2 µm thick samples at substrate temperatures ranging from $0.65T_g$ to $0.92T_g$, where T_g corresponds to the glass transition temperature of the conventional glass, $T_{g,CXIB}$ = 326 K.

Figure 62 shows how limiting fictive and onset temperature depend on the deposition temperature. As expected, glasses of CXIB grown at temperatures between 0.8 and $0.9T_g$ have a maximum T_{on} and a minimum T_f', and therefore the highest kinetic and thermodynamic stability. A difference in the transformation mechanism between the stabilities would not alter this result, since, as we saw in Chapter 4, the limiting fictive temperature is independent of the transformation mechanism and the analysed samples are thick enough to transform, predominantly, through a homogeneous mechanism.

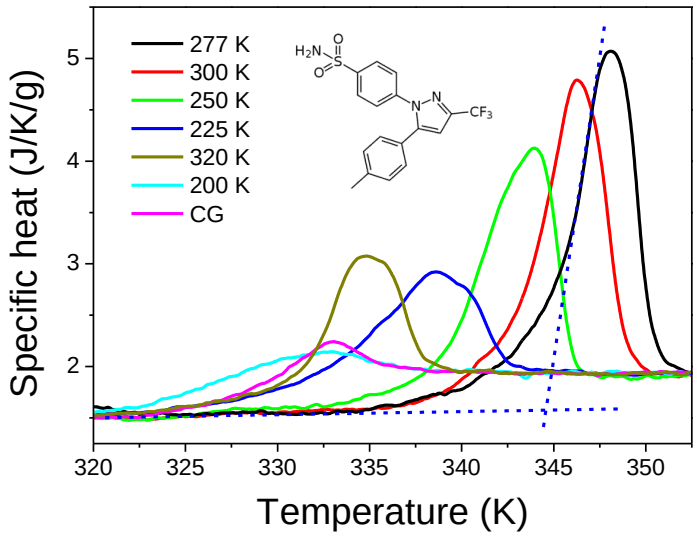

Figure 61. Specific heat curves of glasses of CXIB deposited at different deposition temperatures (see legend), measured by DSC. The dashed lines indicate the onset temperature of the corresponding glass transition. The conventional glass (CG) has been prepared by cooling the liquid at 10 K/min. All measurements have been performed at a heating rate of 10 K/min.

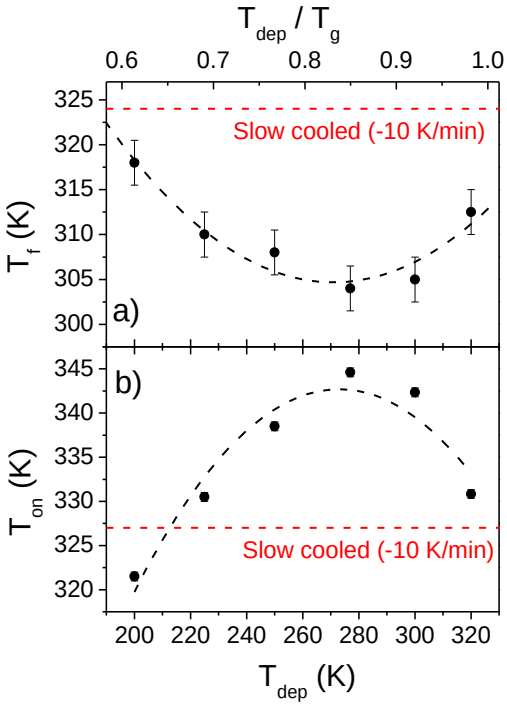

Figure 62. (a) Limiting fictive temperatures and (b) onset temperature values for glasses of CXIB grown at different substrate temperatures. Deposition temperature is also expressed relative to the conventional glass transition of CXIB, T_g=326 K. Clearly, there is a minimum in T_f' and a maximum in T_{on} in glasses grown around 0.85Tg, indicating a maximum in both kinetic and thermodynamic stability. Dashed lines are a guide to the eye.

In order to obtain glasses with such kinetic and thermodynamic stability it would be necessary to submit the conventional glass to very long aging times or to cool down the liquid at very slow cooling rates. While the first option is not feasible in the laboratory time scale, the second option would not produce a glass but a crystal, since the necessary cooling rates are in general much lower than the critical cooling rate, Q_r. From DSC measurements we have estimated for CXIB a Q_r around 0.5–1 K/min, when cooling the sample from the melting temperature. A calculation of the equivalent cooling rate associated to a certain limiting fictive temperature can be carried out by extrapolating the Arrhenius relation between the scaled cooling rate Q/Q_s and the limiting fictive temperature T_f'/T'_{fS}[130]. Figure 63 shows the normalized fictive temperatures of bulk glasses obtained experimentally by cooling the liquid at different rates. For the normalization, the fictive temperature of the conventional glass (Q_s = −10 K/min) has been used. The equivalent cooling rates of the glassy films are obtained from the extrapolation of the Arrhenius fit of the experimental data on the basis of their limiting fictive temperature. For the most stable glass (deposited at $0.85T_g$ with T_f' = 305 K), the equivalent cooling rate is of the order of 10^{-4} K/min, four orders of magnitude lower than the critical cooling rate for crystallization. Moreover, from the slope and the intersection of the plot of figure 63 one can determine the thermodynamic fragility of the material as stated by Wang et al.[131]. The fitting of the experimental data yields a thermodynamic fragility of m = 76 for CXIB. This value is in between the ones predicted by thermal methods by Gupta et al.[57] (m = 67) and Kaushal and Bansal (m = 83.3)[132].

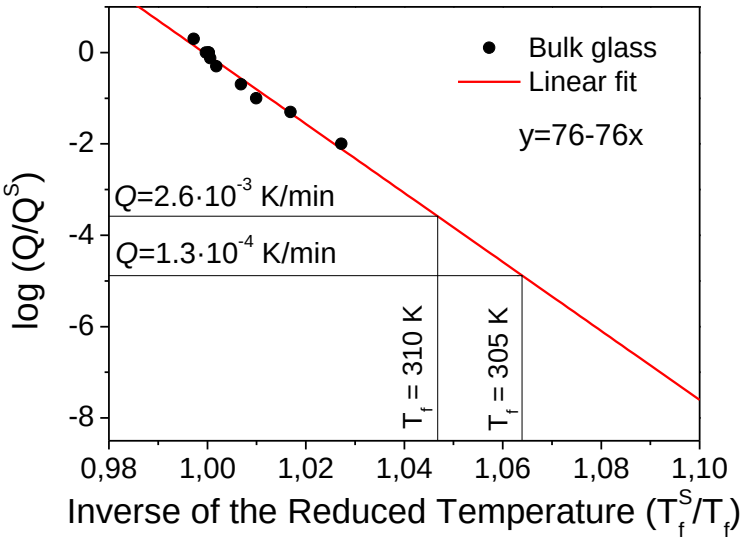

Figure 63. Scaled Arrhenius plot of cooling rate as a function of the limiting fictive temperature. Experimental data have been obtained from bulk samples cooled from the liquid at the corresponding heating rates. The slope and the intersection of the linear fit provides the fragility of the material.

7.2.1.2 Structural anisotropy

Another feature of ultrastable glasses is the exhibition of certain molecular anisotropy. Molecular anisotropy has been previously observed in other organic ultrastable thin film glasses such as IMC or TNB[47,48,50]. In fact, anisotropic packing arrangements are common in thin films grown from the vapour and have been identified also in other vapour-deposited organic thin films employed in OLED technology[49,133]. This anisotropic peak appears as a consequence of an extra periodicity in the molecular arrangement of the glass and is a clear feature of ultrastable vapour deposited glasses, since it has not been typically observed in conventional glasses. Synchrotron radiation provides the opportunity to analyse the structure of thin-film glasses due to the high sensibility of the technique. Also, the fast dynamics of glass transformation requires the use of very short integration times during the measurement. On the other hand, 2D x-ray detectors are convenient to analyse anisotropic structures along a particular molecular axis. We have measured 40 μm thick films of CXIB glasses deposited at 0.85Tg by wide-angle x-ray scattering (WAXS) at ALBA synchrotron light source facility in grazing incidence geometry using a 2D detector (Figure 64a). The recorded 2D diffraction patterns together with an angular integration for the vapour deposited glass and for the same sample after being transformed and cooled back at 10 K/min are shown in Figure 64 b-d. While the differences in the main peak at q = 1.3 $Å^{-1}$, characteristic of organic amorphous systems, can be attributed to instrumental uncertainties, the intensity of the low-q peak at q = 0.35 $Å^{-1}$ is clearly more pronounced in the vapour deposited film and clearly indicated the ultrastable character of the sample. The intensity variations in the low-angle ring of the 2D spectra of Figure 64b illustrate the existence of molecular anisotropy in the vapour deposited ultrastable glass, while a continuous full ring can be distinguished in the conventional glass (Figure 64c).

We have followed the evolution of the low-q peak during the transformation of the stable glass into supercooled liquid at three different annealing temperatures (330 K, 335 K, 338 K). By integrating the WAXS profiles, as shown in Figure 64d, we calculate the excess scattering of the low-q peak taking the conventional glass low-q peak as reference, according to Dawson et al.[47]:

$$\Delta I(T;q=0.4Å^{-1}) = \frac{\int_{0.25}^{0.5} I(T;q)dq - \int_{0.25}^{0.5} I(CG;q)dq}{\int_{0.25}^{0.5} I(CG;q)dq} \quad (41)$$

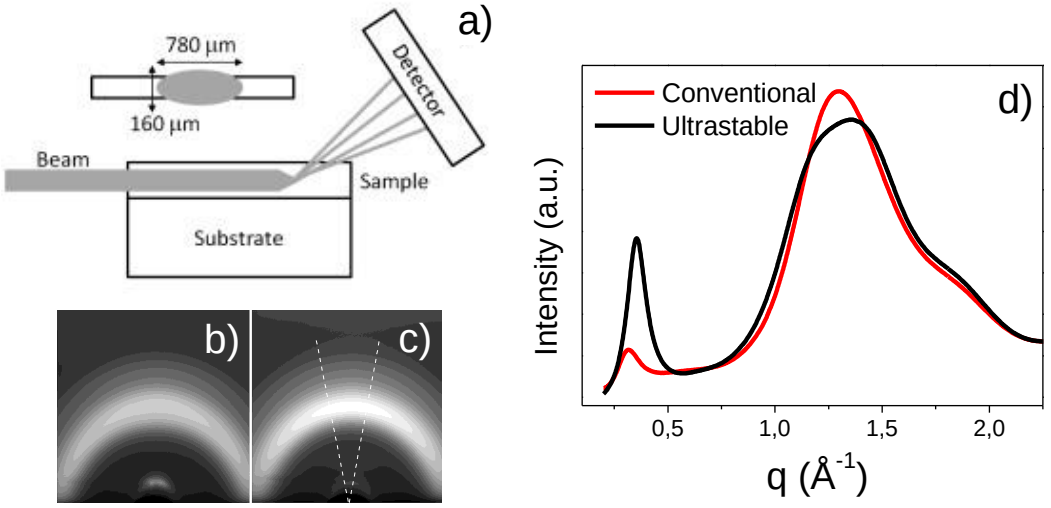

Figure 64. X-ray diffraction scans of 40 um thick ultrastable and conventional CXIB glasses. a) sketch of the experimental setup, b) and c) 2D X-ray diffraction pattern from the vapour deposited glass and the conventional glass, respectively. In the case of the ultrastable sample a more intense and non-homogenous low-q ring is observed, corresponding to the anisotropic arrangement. d) q-scan obtained from integration of the indicated region in the 2D plots and from for both glasses. The highest low-q peak corresponds to the low-q ring in the 2D spectra, while the main broad peak is a typical feature of amorphous systems, which indicates a large dispersion of inter molecular distances.

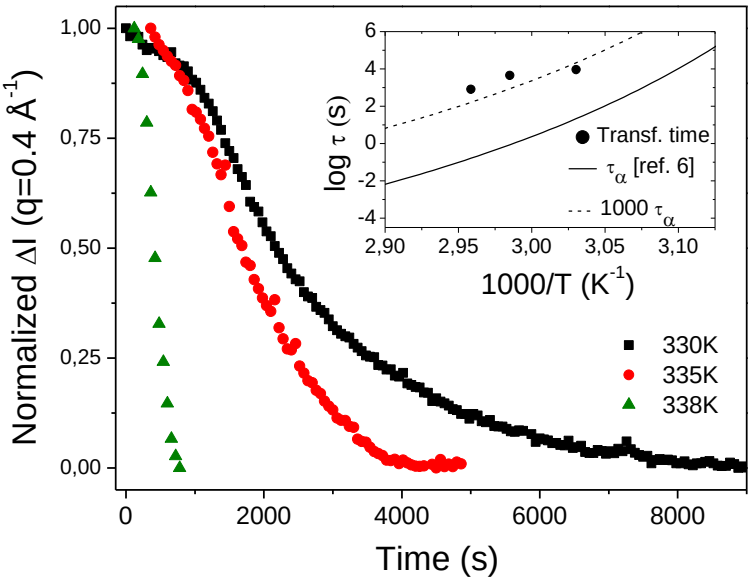

Figure 65. Evolution of the intensity of the low-q peak observed in the diffraction pattern of ultrastable CXIB glasses during isotherms at different temperatures. The time elapsed from the beginning of the measurement until the low-q peak has completely disappeared is considered as the transformation time of the glass at that particular temperature. In the inset, the measured transformation times are plotted and compared to the alpha structural relaxation time of the corresponding equilibrium liquid.

In Figure 65 we compare the time evolution of the low-q peak for three annealing temperatures (330, 335 and 338 K). The final transformation times are shown in the inset of Figure 65 and compared with the Vogel–Fulcher–Tamman (VFT) relation for the alpha relaxation time of CXIB[6]. The time required to anneal away the anisotropic peak is more than 3 orders of magnitude longer compared to the structural relaxation time of the supercooled liquid, similar to our previous results from IMC (see chapter 5) and to previous findings for other molecules[100,134–136].

7.2.2 Crystallization dynamics

Crystallization is a key issue in the use of molecular organic glasses for pharmaceutical drugs. In the case of celecoxib, for instance, the glass presents a strong tendency to crystallize in different polymorphs[125]. It is reasonable then to check if ultrastable glasses show differentiated crystallization behaviour with respect to the conventional glass. As a first approach to answer this question, here we propose to follow the surface crystallization of glasses of CXIB of different stabilities using optical microscopy during an isothermal treatment at 318 K (T_g-8 K) and 60% relative humidity. Three different batches of highly stable glasses deposited at $T_{dep} = 0.85T_g$ at a growth rate of 0.2 nm/s have been studied. For a direct comparison with the crystallization of the conventional glass, one sample of each batch was heated above the glass transition temperature and cooled down at 10 K/min. The results are summarized in Figure 66. Only one type of crystal on the surface of the glasses has been identified (Figure 66a). X-ray diffraction patterns of deposited films after crystallization show the presence of phases II and III, independently of the deposition conditions. Interestingly, thinner films show a pre-eminence of phase III. One possibility is that the type of crystals observed on the surface could mainly correspond to phase III. These results would also indicate that some crystallization may take place in the bulk of the films, either forming phase II crystals, or a mixture of II and III.

From the optical microscopy picture, there is apparently some preferential directions for crystal growth. In fact, from our observations in the AFM image on a surface crystal (Figure 67), the crystals appear to grow following straight lines, which are few micrometres thick and between tens and a hundred nanometers in height, taking as zero reference the surface of the glass. Yu et al. showed how surface crystals in IMC grow at the expense of the molecules from the surface and, as a result, crystals grow fast in height[137]. We see, however, that the obtained crystals consume the surrounding molecules during growth and leave trenches of the same depth than the height of the crystals along the growth direction, although this observation may be accentuated by the PID recovery of the AFM tapping mode.

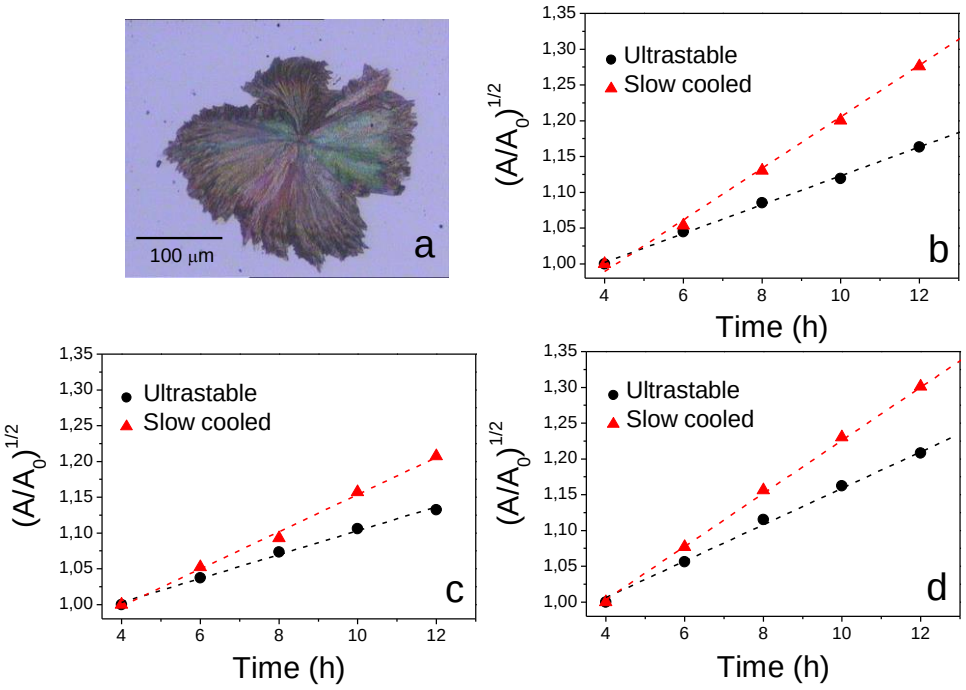

Figure 66. Evolution of the crystal grown on the surface of ultrastable and conventional glasses of CXIB. a) Optical microscopy image of a surface crystal after 10 hours at 318 K and 60% of relative humidity. b), c) and d) Square root of the area, normalized to the initial area of a crystal as a function of time for three different batches of samples. The slow cooled glasses have been obtained by heating an as-deposited ultrastable glass above its glass transition temperature and cooling it down at 10 K/min. The same crystalline phase appeared on all samples, independently on the batch or the production method.

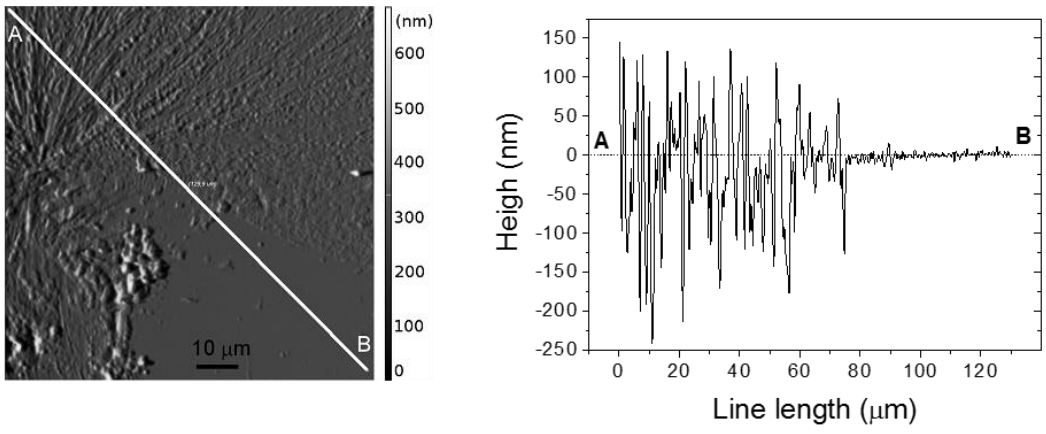

Figure 67. AFM image of a surface crystal on top of an ultrastable glass film (top image). The height profile corresponding to the line AB is shown at the bottom image. The flat region, which corresponds to the glass surface, has been shifted to zero for a better reading.

Since the growth of the crystals is not isotropic, the evolution of the area of the crystal as a function of time is not a reliable estimate of the absolute value of their linear growth rate. In an attempt to quantify the growth rate, we normalise the area of the crystals by their initial area before taking the square root. In this way, we remove the dependence on the initial shape of the crystal, obtaining a relative growth rate. This value is further used to compare the growth rate for every batch of samples. Figures 66b-d show the evolution of the square root of the normalized area as a function of temperature. Clearly, the crystals grow slower on the surface of the ultrastable glass than on the conventional glass, although, depending on the sample batch, the rates are slightly different. We perform a rough evaluation of the linear growth rate by assuming that crystals are circular and the growth is isotropic. Within this approximation, we obtain an average value of 0.14 ± 001 nm/s for the UG and 0.19 ± 0.04 nm/s for the conventional glass. These values are comparable to the rate obtained for γ-IMC surface crystals[138], which is around 0.4 nm/s at a temperature 8 K below T_g. It should be emphasized that, while the absolute value of crystal growth is slightly sample-dependent, the relative slowing down of the lateral surface crystal growth of the ultrastable glass compared to the conventional glasses is a very reliable quantity, of the order of 30%. If surface mobility dominates crystal growth it is reasonable to ask why the observed results seem to be at odds with previous data by Brian et al.[31]. In fact, these authors have shown that molecular mobility at the free surface is independent of the stability of the bulk, at least for aged molecular glasses with a decrease up to 15 K in their limiting fictive temperature. In contrast, the presented data evidence a slight variation in crystal growth rate depending on the stability of the glass. Two interpretations are at hand: i) the measured variation of crystal growth rate, i.e. surface diffusion, is not very significant and it is within the uncertainty of previous measurements and/or ii) surface smoothing and crystal growth occurs through slightly different mechanisms. In fact, these findings may be compatible with both scenarios. Concerning the first possibility, the diffusion data from Brian et al. (figure 5 in ref.[31]) scatters from $1.86 \cdot 10^{-15}$ to $5.37 \cdot 10^{-16}$ m^2/s for glasses with the same stability, revealing that the statistical scattering from sample to sample is higher than the 30% variation observed in this work. This could explain why this effect had not been clearly observed yet. With respect to the second possibility, we note that surface smoothing is driven by the mobility of the top molecular layer, while crystal growth may be influenced by molecules located several molecular diameters deep into the glass. In this case, surface diffusion can be estimated from existing theories in which surface relaxation times depend on the alpha relaxation time of the glass. These models consider that the surface layer is formed by several molecular diameters in thickness. Therefore, surface mobility is stability-dependent and can be several nanometers thick. It is also true that the predicted variation of the near surface relaxation time in those models is much higher than the one observed in this work.

7.3 Water absorption in vapour deposited glasses

In the particular case of indomethacin, even being a hydrophobic compound in its crystalline phase[129], its glass is strongly affected by water absorption, as has been shown in previous studies[110,120]. In order to study the absorption of water as a function of exposure time and glass stability, we deposit thick films (1.5 µm) of IMC at different substrate temperatures in order to get glasses of different stabilities. We study glasses with T_f' = 280, 290, 300 and 305 K. A first set of samples have been deposited on the membrane based nanocalorimeter and have been analysed using a proportional-integrator-differential (PID) heating rate control, which guarantees a constant heating rate of 10 K/min, without breaking the vacuum, i.e. prior to exposing the samples to ambient moisture. Although this method does not provide reliable information about the area of the glass transition peaks, we can measure the onset temperature of the transition (as shown in the insets of figure 8). A second set of samples have been deposited on aluminium foil and have been exposed to ambient moisture (60% relative humidity) for a given time (t = 0.5, 2, 4 and 21 hours). We have followed the glass transition by means of conventional DSC. These measurements are summarized in Figure 68.

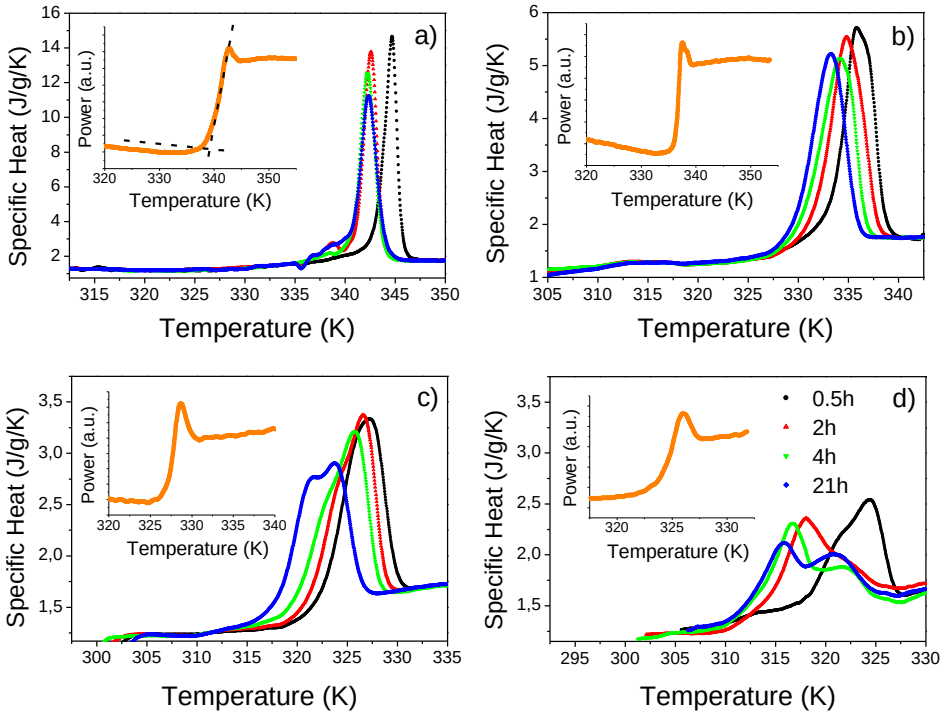

Figure 68. Specific heat as a function of temperature for samples grown at different substrate temperatures, T_{dep}, measured by DSC at 10 K/min: a) T_{dep} = 266K, b) T_{dep} = 290K, c) T_{dep} = 300K and d) T_{dep} = 305K. Each colour corresponds to a different exposure time: t = 0.5 hours (black), t = 2 hours (red), t = 4 hours (green) and t = 21 hours (blue). The insets show the power curve obtained by the PID in-situ measurement of the equivalent as-deposited sample.

Several features can be appreciated from the graphs represented in Figure 68. One of them is the presence, in some cases, of a double peak during the transformation, which appears more obvious for the largest exposure times. We also see from Figure 68 a clear shift of the onset temperature towards lower values as exposure time increases, indicating a decrease of the kinetic stability. In order to have a clearer picture of this phenomenon, we plot the onset temperature of the transformation as a function of the deposition temperature for each of these samples, from t = 0 (corresponding to the in-situ measurement) to t = 21 hours of exposure, as seen in Figure 69. In the cases where two peaks appear, the onset temperature shown in the graph refers to the peak at lower temperature.

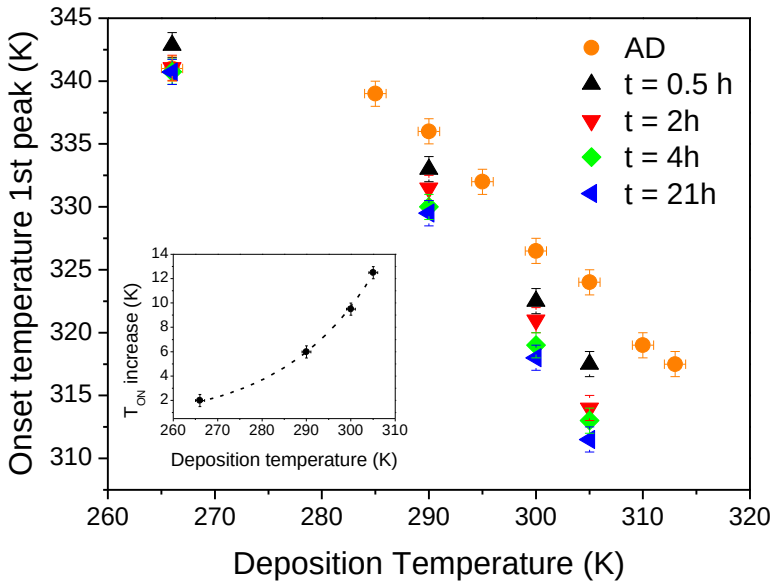

Figure 69. Onset temperature of the first peak of the glass transition as a function of deposition temperature, for different exposure times. The orange circles correspond to the in-situ measurement (PID). Longer exposure times give rise to lower onset temperatures. The inset shows the relationship between the increase in the onset temperature after 21 h of exposure as a function of deposition temperature. The dashed line in the inset is a guide for the eye.

It is interesting to note how samples deposited at higher temperatures, and hence with lower thermodynamic stability, undergo a stronger change in onset temperature with exposure time, implying a higher decrease on their kinetic stability. The most interesting case corresponds to ultrastable glasses, which seem to be practically unaffected after exposition to ambient moisture. In the inset of Figure 69 we represent the temperature shift of the onset of the first glass transition peak after 21 h of exposure as a function of the limiting fictive temperature, clearly showing the dependence of water absorption in stability.

The presence of a double peak during the transformation of the less stable glasses observed in Figure 68 indicates that the glass transforms into the liquid via two separated processes. Using equation 20 from Chapter 4 and assuming that the enthalpy excess per unit volume is the same for both processes, we can extract from the calorimetric trace the information concerning the transformation rate of the glass. We subsequently de-convolute the transformation rate signal in two Gaussian peaks in order to study of the evolution of the two processes separately (Figure 70).

From the de-convoluted Gaussian peaks shown in 70, we can analyse the evolution of each process in the various glasses. Figure 71 plots the evolution as a function of exposure time of the onset of the two Gaussian peaks obtained from the fitting. Although some information about the area of the peaks could be extracted, the difficulties to separate the effects of water absorption and aging on the area of the peak preclude the analysis of these data.

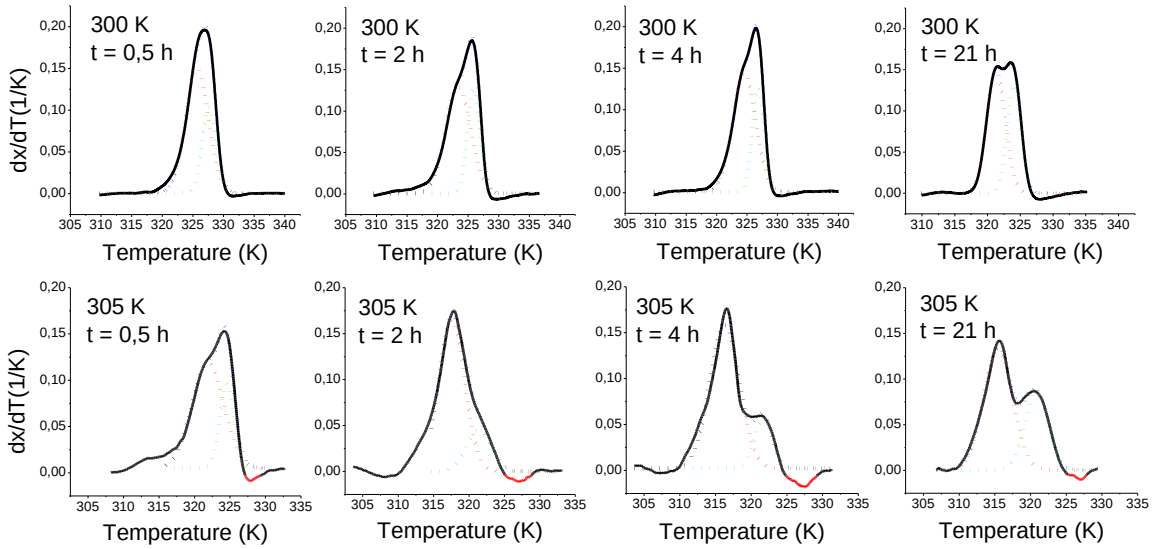

Figure 70. Deconvolution of transformation rates obtained using equation 20, for glasses deposited at T_{dep} = 300 K and T_{dep} = 305 K after different times of ambient exposure, using a general Gaussian function. From this fit, information concerning the evolution of the two different glass transition peaks can be obtained.

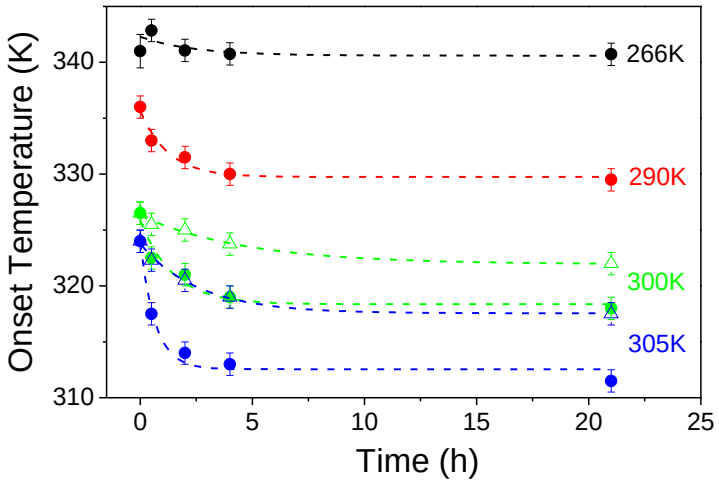

Figure 71. Onset temperature of the devitrification peaks of the measured samples, shown in Figure 70 (solid symbols: first peak; empty symbols: second peak). The dashed lines are guides to the eye. The temperatures indicate the deposition temperature of each sample.

We observe the same tendency for all the samples: as the exposure time increases, the onset of the transformation shifts towards lower temperatures. After a few hours, a saturation point is apparently reached in the case of the first peak (solid symbols). The second peak (open symbols), although evolves much slower, does not seem to have achieved the saturation point. Another difference is the total shift of the two peaks, when distinguishable. The first peak moves towards lower temperatures than the second one. In the case that the two transitions could correspond to different sub-regions in the glass, we could speculate that the first peak observed in the analysed curves corresponds to the regions where water is strongly attached to the carboxylic groups, hence strongly reducing the interaction between IMC molecules and promoting a fast mobility. The second peak would correspond, therefore, to regions where water is only slightly attached to IMC molecules. In the second case, although some interaction between water and IMC would remain, the mobility would seem affected in the same degree as the first case. In most stable samples, there are fewer available carboxyl groups[109,120,139] and most of the water goes to less polar sites into the molecule, avoiding the appearance of a double peak transformation.

Zografi et al. reported, for IMC conventional glasses, the diminution on the glass transition after water absorption[120]. They found that, as a rough estimation, the onset of the transformation shifted 10 K towards lower values per 1% water concentration in weight. From these measurements and considering that saturation has been almost reached after 21 hours of exposure, we find, in the case of the ultrastable glass (T_f' = 280 K), that the absorbed amount of water could be around 0.2% in weight. For T_f' = 290 K, 0.6%, for T_f' = 300 K, 0.95% and for the glass with T_f' = 305 K, 1.25%. These values are consistent with the ones reported by Ediger et al. for the stable and

conventional (and annealed) glasses[110]. In particular, the agreement with the stable sample (T_f' = 280 K in this case) is quite satisfactory (0.2% in the studied case, 0.16% in theirs). In the case of the less stable sample, here we report, according to the Zografi approximation, a 1.25% of water content, while Ediger reports 0.88%. Apart from the possible inaccuracy of the applied relationship between onset shift and absorbed water, the difference may arise from the fact that the described processes have been performed at an ambient relative humidity of around 60%, while Ediger and co-workers report a RH of 50%.

From the measured heat capacity, we can determine if the absorption of water takes place through all the volume of the glass or if it is just a surface effect. Zografi and co-workers showed that water was absorbed into the bulk of the conventional indomethacin glass, while in the case of the crystal, water molecules were adsorbed onto its surface[120]. Ediger and co-workers underlined three experimental observations to indicate that also in the case of ultrastable glasses the water was absorbed into the bulk instead of being adsorbed onto the surface of the glass[110]. Here, we measure the specific heat of samples of glassy indomethacin with the same thermal stability (deposition temperature) but different thickness. We find that all the curves fairly overlap into a single one, irrespective of their thickness (Figure 72), which indicates that the sample absorbs water homogeneously throughout the whole sample and the transformation is, therefore, proportional to the mass.

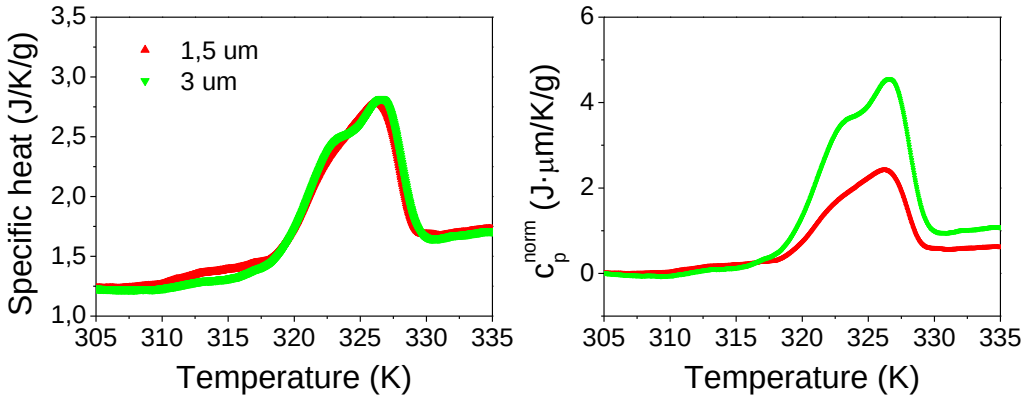

Figure 72. Heat capacity curves of IMC glasses with different thickness deposited at 300 K. a) normalized by the mass of the sample and b) normalized by the area, according to equation 21 in Chapter 4.

7.4 Chapter summary

The industrial and commercial application of glasses is often hindered by some drawbacks inherent to the nature of glasses. One of these major problems is the natural tendency of glasses towards crystallization. On the other hand, water absorption in glasses may enhance crystallization and should be avoided. Ultrastable glasses could represent one major opportunity to overcome these drawbacks.

We have been able to prepare glasses of celecoxib, a poor glass-former with a particularly high tendency to crystallize. By vapour deposition, glasses with very high stability can be produced, with an onset of devitrification tens of kelvin above the ordinary value, similar to what we found for Indomethacin. WAXS images show the existence of a certain short range periodicity, not present in conventional glasses, that vanishes during the transformation to the liquid state. We have observed that crystallites that spontaneously grow at the surface of ultrastable celecoxib grow in the lateral direction around 30% slower than on the surface of the conventional glass.

On the other hand, stability reduces the amount of moisture that the glass can absorb, as observed through the shift of the devitrification onset of indomethacin. Water molecules could be absorbed in particular zones of the glass structure, originating two transformation peaks. In the case of the most stable glasses, one of these two regions would not be accessible. Also, we conclude than water molecules are incorporated into the bulk of the glass rather than on the surface, as has been previously observed for crystalline indomethacin.

8. SUMMARY

Vapour deposition has emerged as a very powerful tool to produce glasses of unprecedented stability. Moreover, by tuning the deposition conditions, one can tailor the properties of the deposited glass. On the other hand, fast-scanning nanocalorimetry has proven to be an extremely useful technique to evaluate different characteristics of the mechanisms behind the glass transition at temperatures much above the typically explored low temperature range. In this thesis, we have presented a detailed study of different aspects of the glass transition on vapour deposited organic glasses by combining a variety of calorimetric techniques, from conventional to fast-scanning calorimetry, including high pressure-thermal analysis.

Glasses of indomethacin and celecoxib have been deposited by means of vapour deposition at a wide range of deposition temperatures. We see that the thermodynamic and kinetic stability of these glasses depend on the deposition temperature. At substrate temperatures around $0.85T_g$, the maximum stability is reached. Glasses grown above $0.85T_g$ are in equilibrium with the liquid and have a limiting fictive temperature equal to the deposition temperature. In opposition, glasses grown at lower temperature are not in equilibrium during the deposition.

Ultrastable glasses produced from the vapour phase exhibit a different transformation mechanism with respect to glasses obtained by cooling the liquid. While the latter transform via a homogeneous process that takes place throughout the volume of the sample, more stable glasses start the transformation via a heterogeneous process. This heterogeneous mechanism consists on a parallel transformation front that starts at the surface or interfaces and propagates into the bulk. We have developed an ad-hoc surface normalization procedure that permits the identification of the transformation mechanism and the evaluation of the growth front velocity. We have seen that the front velocity can be expressed as a function of the relaxation time of the liquid, $v_{gr} = C\tau^{-0.79}$, where C depends on the deposition conditions of the sample and is not temperature dependent. We have found that this expression holds for a very large temperature range, from T_g+10 K up to T_g+75 K. The dynamics of the supercooled liquid that constitutes the transformed front determines the dependence of transformation rate on temperature, which is consistent with recent theories on the glass transition. Although there is a noticeable influence of deposition conditions on front velocity, its effect is much weaker than the influence of temperature. Deposition conditions determine the stability of the glass, measured through its limiting fictive temperature. However, we have seen that limiting fictive temperature does not univocally determine the front velocity. Molecular orientation, also determined by deposition conditions, could play a role in the transformation rate. In particular, glasses with strong birefringence, present faster front velocities.

Eventually, once the front has started to advance, the homogeneous transformation is triggered. We define the cross-over length as the distance that the front has advanced before the homogeneous process starts. The size of this cross-over length depends on the deposition conditions. The transformation in films thicker than the cross-over length is clearly dominated by the homogeneous process. In order to study how stability influences this type of transformation in an extended temperature range, we have deposited thick glassy films at different deposition temperatures and we have analysed them by nanocalorimetry. From the onset of devitrication and the width of the transformation peaks we infer the relaxation time of the glass. We have seen that the evolution of relaxation time as a function of temperature follows a super-Arrhenius dependence, similar to the VFT expression for the equilibrium alpha relaxation time of the supercooled liquid. This expression, however, satisfactorily describes the dynamics of supercooled liquid and glasses of different stability simultaneously. The stability of the different glasses is represented in this expression by their limiting fictive temperature, while in the supercooled liquid, fictive temperature is defined as the actual temperature of the system. This unified view of glasses and liquids may help understating the connection between the dynamic and thermodynamic characteristics of a glass. Indeed, we have shown that glasses of different stability follow density scaling relationships that were conceived to describe uniquely equilibrium liquid states. In that sense, the dynamics of liquid and glasses are influenced, in the same manner, by temperature and density uniquely.

In order to incorporate the effect of pressure to the proposed unified model, we have measured the variation of the onset temperature of devitrification of glasses with very different stability as a function of hydrostatic pressure. We have found that the devitrification temperature tends to a unique T_{on} value, regardless of the stability of the glass, depicting a scenario in which both ultrastable and conventional glasses transform into the liquid at very similar temperatures.

Being crystallization a major drawback for the extended use of glasses in the pharmaceutical industry, it is reasonable to wonder if ultrastability would somehow have a significant impact. In order to tackle this issue, we have measured the growth rate of surface crystals on ultrastable and conventional glasses of celecoxib, a widely extended and poor glass former pharmaceutical compound. We have seen that crystals grow a 30% slower on top of ultrastable glasses. The lower mobility of the ultrastable glass could be among the reasons for this difference. We have also analysed the influence of stability on water absorption. Water may change the kinetic stability of the glass inducing crystallization, among other undesired effects. We show that the amount of absorbed water depends on the stability of the glass, reaching an almost negligible value in the case of ultrastable glasses. The improved packing and reduction of accessible hydrogen bonds in this type of glasses could explain this behaviour.

REFERENCES

1. So much more to know... *Science* **309,** 78–102 (2005).
2. Langer, J. The mysterious glass transition. *Phys. Today* **60,** 8–9 (2007).
3. Roos, Y. H. Glass transition temperature and its relevance in food processing. *Annu. Rev. Food Sci. Technol.* **1,** 469–96 (2010).
4. Qiao, J. C. & Pelletier, J. M. Dynamic Mechanical Relaxation in Bulk Metallic Glasses: A Review. *J. Mater. Sci. Technol.* **30,** 523–545 (2014).
5. Yu, L. Amorphous pharmaceutical solids: preparation, characterization and stabilization. *Adv. Drug Deliv. Rev.* **48,** 27–42 (2001).
6. Grzybowska, K. & Paluch, M. Molecular dynamics and physical stability of amorphous anti-inflammatory drug: celecoxib. *J. Phys. Chem. B* **114,** 12792–801 (2010).
7. Foundation, E. S. Materials Science and Engineering Expert Committee (MatSEEC) Metallurgy Europe – A Renaissance Programme for 2012-2022. (2012).
8. Yu, H. Bin, Wang, W. H., Bai, H. Y. & Samwer, K. The β-relaxation in metallic glasses. *Natl. Sci. Rev.* **1 ,** 429–461 (2014).
9. Wang, W. H. Bulk Metallic Glasses with Functional Physical Properties. *Adv. Mater.* **21,** 4524–4544 (2009).
10. Forrest, S. R. & Thompson, M. E. Introduction: Organic Electronics and Optoelectronics. *Chem. Rev.* **107,** 923–925 (2007).
11. Shirota, Y. Photo- and electroactive amorphous molecular materials—molecular design, syntheses, reactions, properties, and applications. *J. Mater. Chem.* **15,** 75–93 (2005).
12. Cavagna, A. Supercooled liquids for pedestrians. *Phys. Rep.* **476,** 51–124 (2009).
13. Debenedetti, P. G. & Stillinger, F. H. Supercooled liquids and the glass transition. *Nature* **410,** 259–67 (2001).
14. Langer, J. S. Theories of glass formation and the glass transition. *Rep. Prog. Phys.* **77,** 042501 (2014).
15. Santen, L. & Krauth, W. Absence of thermodynamic phase transition in a model glass former. *Nature* **405,** 550–1 (2000).
16. Torquato, S. Glass transition. Hard knock for thermodynamics. *Nature* **405,** 521, 523

(2000).

17. Gibbs, J. H. & DiMarzio, E. A. Nature of the Glass Transition and the Glassy State. *J. Chem. Phys.* **28,** 373 (1958).

18. Angell, C. A., Ngai, K. L., McKenna, G. B., McMillan, P. F. & Martin, S. W. Relaxation in glassforming liquids and amorphous solids. *J. Appl. Phys.* **88,** 3113 (2000).

19. Lunkenheimer, P. & Loidl, A. Dielectric spectroscopy of glass-forming materials: α-relaxation and excess wing. *Chem. Phys.* **284,** 205–219 (2002).

20. Kob, W. *The Mode-Coupling Theory of the Glass Transition*. **676,** (American Chemical Society, 1997).

21. Giordano, V. M. & Ruta, B. Unveiling the structural arrangements responsible for the atomic dynamics in metallic glasses during physical aging. *Nat. Commun.* **7,** 10344 (2016).

22. Cangialosi, D., Boucher, V. M., Alegría, A. & Colmenero, J. Direct evidence of two equilibration mechanisms in glassy polymers. *Phys. Rev. Lett.* **111,** 095701 (2013).

23. Raza, Z., Alling, B. & Abrikosov, I. A. Computer simulations of glasses: the potential energy landscape. *J. Phys. Condens. Matter* **27,** 293201 (2015).

24. Johari, G. P. & Aji, D. P. B. Time-dependent paths, fictive temperatures and residual entropy of glass. *Philos. Mag.* **90,** 4377–4392 (2010).

25. Stillinger, F. H. & Debenedetti, P. G. Glass Transition Thermodynamics and Kinetics. *Annu. Rev. Condens. Matter Phys.* **4,** 263–285 (2013).

26. Ediger, M. D., Angell, C. A. & Nagel, S. R. Supercooled Liquids and Glasses. *J. Phys. Chem.* **100,** 13200–13212 (1996).

27. Angell, C. A. Entropy and fragility in supercooling liquids. *J. Res. Natl. Inst. Stand. Technol.* **102,** 171 (1997).

28. Kauzmann, W. The Nature of the Glassy State and the Behavior of Liquids at Low Temperatures. *Chem. Rev.* **43,** 219–256 (1948).

29. Tanaka, H. Possible resolution of the Kauzmann paradox in supercooled liquids. *Phys. Rev. E. Stat. Nonlin. Soft Matter Phys.* **68,** 011505 (2003).

30. Tanaka, H. Relation between Thermodynamics and Kinetics of Glass-Forming Liquids. *Phys. Rev. Lett.* **90,** 055701 (2003).

31. Brian, C. W., Zhu, L. & Yu, L. Effect of bulk aging on surface diffusion of glasses. *J. Chem. Phys.* **140,** 054509 (2014).

32. Johari, G. P. & Shanker, R. M. On determining the relaxation time of glass and amorphous pharmaceuticals' stability from thermodynamic data. *Thermochim. Acta* **511,** 89–95 (2010).

33. Mauro, J. C., Loucks, R. J. & Gupta, P. K. Fictive Temperature and the Glassy State. *J. Am. Ceram. Soc.* **92,** 75–86 (2009).

34. Tool, A. Q. & Eicitlin, C. G. Variations caused in the heating curves of glass by heat treatment. *J. Am. Ceram. Soc.* **14,** 276–308 (1931).

35. GARDON, R. & NARAYANASWAMY, O. S. Stress and Volume Relaxation in Annealing Flat Glass. *J. Am. Ceram. Soc.* **53,** 380–385 (1970).

36. Moynihan, C. T. *et al.* Structural relaxation in vitreous materials. *Ann. N. Y. Acad. Sci.* **279,** 15–35 (1976).

37. Swallen, S. F. *et al.* Organic glasses with exceptional thermodynamic and kinetic stability. *Science* **315,** 353–6 (2007).

38. Zhu, L. *et al.* Surface self-diffusion of organic glasses. *Phys. Rev. Lett.* **117,** 256103 (2013).

39. Kearns, K. L. *et al.* Hiking down the Energy Landscape: Progress Toward the Kauzmann Temperature via Vapor Deposition. *J. Phys. Chem. B* **112,** 4934–4942 (2008).

40. Leon-Gutierrez, E., Garcia, G., Lopeandia, A. F., Clavaguera-Mora, M. T. & Rodríguez-Viejo, J. Size Effects and Extraordinary Stability of Ultrathin Vapor Deposited Glassy Films of Toluene. *J. Phys. Chem. Lett.* **1,** 341–345 (2010).

41. Berthier, L. & Ediger, M. D. Facets of glass physics. *Phys. Today* **69,** 40–46 (2016).

42. Dalal, S. S., Fakhraai, Z. & Ediger, M. D. High-throughput ellipsometric characterization of vapor-deposited indomethacin glasses. *J. Phys. Chem. B* **117,** 15415–25 (2013).

43. Kearns, K. K. L., Ediger, M. D. M., Huth, H. & Schick, C. One micrometer length scale controls kinetic stability of low-energy glasses. *J. Phys. Chem. Lett.* **1,** 388–392 (2009).

44. Pogna, E. A. A. *et al.* Probing equilibrium glass flow up to exapoise viscosities. *Proc. Natl. Acad. Sci. U. S. A.* **112,** 2331–6 (2015).

45. Kearns, K. L., Still, T., Fytas, G. & Ediger, M. D. High-modulus organic glasses prepared by physical vapor deposition. *Adv. Mater.* **22,** 39–42 (2010).

46. Fakhraai, Z., Still, T., Fytas, G. & Ediger, M. D. Structural variations of an organic glassformer vapor-deposited onto a temperature gradient stage. *J. Phys. …* **2,** 423–427 (2011).

47. Dawson, K., Zhu, L., Yu, L. & Ediger, M. Anisotropic structure and transformation kinetics of vapor-deposited indomethacin glasses. *J. Phys. Chem. B* **115,** 455–463 (2010).

48. Dawson, K. *et al.* Molecular packing in highly stable glasses of vapor-deposited tris-naphthylbenzene isomers. *J. Chem. Phys.* **136,** 094505 (2012).

49. Dalal, S. S., Walters, D. M., Lyubimov, I., de Pablo, J. J. & Ediger, M. D. Tunable molecular orientation and elevated thermal stability of vapor-deposited organic semiconductors. *Proc. Natl. Acad. Sci.* **112,** 201421042 (2015).

50. Gujral, A., O'Hara, K. A., Toney, M. F., Chabinyc, M. L. & Ediger, M. D. Structural Characterization of Vapor-Deposited Glasses of an Organic Hole Transport Material with X-ray Scattering. *Chem. Mater.* **27,** 3341–3348 (2015).

51. Chen, Z., Sepúlveda, a, Ediger, M. D. & Richert, R. Dynamics of glass-forming liquids. XVI. Observation of ultrastable glass transformation via dielectric spectroscopy. *J. Chem. Phys.* **138,** 12A519 (2013).

52. Sepúlveda, a, Swallen, S. F., Kopff, L. a, McMahon, R. J. & Ediger, M. D. Stable glasses of indomethacin and α,α,β-tris-naphthylbenzene transform into ordinary supercooled liquids. *J. Chem. Phys.* **137,** 204508 (2012).

53. Pérez-Castañeda, T., Rodríguez-Tinoco, C., Rodríguez-Viejo, J. & Ramos, M. a. Suppression of tunneling two-level systems in ultrastable glasses of indomethacin. *Proc. Natl. Acad. Sci. U. S. A.* 1–6 (2014). doi:10.1073/pnas.1405545111

54. Sepúlveda Márquez, A. Nanocalorimetric studies of several kinetic phenomena over a wide range of heating rates. at <http://www.tdx.cat/handle/10803/32132>

55. Dalal, S. S., Sepúlveda, A., Pribil, G. K., Fakhraai, Z. & Ediger, M. D. Density and birefringence of a highly stable α,α,β-trisnaphthylbenzene glass. *J. Chem. Phys.* **136,** 204501 (2012).

56. Shamblin, S. & Tang, X. Characterization of the time scales of molecular motion in pharmaceutically important glasses. *J. Phys. Chem. B* **103,** 4113–4121 (1999).

57. Gupta, P., Chawla, G. & Bansal, A. K. Physical stability and solubility advantage from amorphous celecoxib: the role of thermodynamic quantities and molecular mobility. *Mol. Pharm.* **1,** 406–13 (2004).

58. Würflinger, A. Differential thermal analysis under high pressure IV: Low-temperature DTA of solid-solid and solid-liquid transitions of several hydrocarbons up to 3 kbar. *Berichte der Bunsengesellschaft für Phys. Chemie* **79,** 1195–1201 (1975).

59. Mañosa, L. *et al.* Giant solid-state barocaloric effect in the Ni-Mn-In magnetic shape-

memory alloy. *Nat. Mater.* **9,** 478–81 (2010).

60. Zhang, M., Efremov, M. Y., Olson, E. a., Zhang, Z. S. & Allen, L. H. Real-time heat capacity measurement during thin-film deposition by scanning nanocalorimetry. *Appl. Phys. Lett.* **81,** 3801 (2002).

61. Denlinger, D. W. *et al.* Thin film microcalorimeter for heat capacity measurements from 1.5 to 800 K. *Rev. Sci. Instrum.* **65,** 946–959 (1994).

62. Lai, S., Ramanath, G., Allen, L., Infante, P. & Ma, Z. High speed (104° C/s) scanning microcalorimetry with monolayer sensitivity (J/m2). *Appl. Phys. Lett.* **67,** 1229–1231 (1995).

63. A.G. Worthing. Atomic Heats of Tungsten and of Carbon at Incandescent Temperatures. *Phys. Rev.* **12,** 199 (1918).

64. Fernández Lopeandía, A. Development of Membrane-based Calorimeters to Measure Phase Transitions at the Nanoscale. (2009). at <http://www.tdx.cat/handle/10803/3405>

65. Molina Ruiz, M. Nanocalorimetric studies of size effects in magnetic oxides and formation kinetics in silicides. at <http://www.tdx.cat/handle/10803/298057>

66. León-Gutierrez, E. *et al.* In situ nanocalorimetry of thin glassy organic films. *J. Chem. Phys.* **129,** 181101 (2008).

67. Leon-Gutierrez, E., Sepúlveda, A., Garcia, G., Clavaguera-Mora, M. T. & Rodríguez-Viejo, J. Stability of thin film glasses of toluene and ethylbenzene formed by vapor deposition: an in situ nanocalorimetric study. *Phys. Chem. Chem. Phys.* **12,** 14693–8 (2010).

68. Capaccioli, S., Ngai, K. L., Paluch, M. & Prevosto, D. Mechanism of fast surface self-diffusion of an organic glass. *Phys. Rev. E* **86,** 051503 (2012).

69. Power, G. & Vij, J. K. Johari-Goldstein relaxation and crystallization of sorbitol to ordered and disordered phases. *J. Chem. Phys.* **120,** 5455–62 (2004).

70. Kearns, K. L., Swallen, S. F., Ediger, M. D., Wu, T. & Yu, L. Influence of substrate temperature on the stability of glasses prepared by vapor deposition. *J. Chem. Phys.* **127,** 154702 (2007).

71. Pérez-Castañeda, T., Jiménez-Riobóo, R. J. & Ramos, M. A. Two-Level Systems and Boson Peak Remain Stable in 110-Million-Year-Old Amber Glass. *Phys. Rev. Lett.* **112,** 165901 (2014).

72. Walters, D. M., Richert, R. & Ediger, M. D. Thermal stability of vapor-deposited stable glasses of an organic semiconductor. *J. Chem. Phys.* **142,** 134504 (2015).

73. Whitaker, K. & Scifo, D. Highly stable glasses of cis-decalin and cis/trans-decalin mixtures. *J. ...* **117,** 12724–33 (2013).

74. Zhu, L. & Yu, L. Generality of forming stable organic glasses by vapor deposition. *Chem. Phys. Lett.* **499,** 62–65 (2010).

75. Guo, Y. *et al.* Ultrastable nanostructured polymer glasses. *Nat. Mater.* **11,** 337–43 (2012).

76. Aji, D. P. B. *et al.* Ultrastrong and Ultrastable Metallic Glass. 1–24 (2013).

77. Yu, H.-B., Luo, Y. & Samwer, K. Ultrastable metallic glass. *Adv. Mater.* **25,** 5904–8 (2013).

78. Lubchenko, V. & Wolynes, P. G. Theory of structural glasses and supercooled liquids. *Annu. Rev. Phys. Chem.* **58,** 235–66 (2007).

79. Swallen, S. F., Windsor, K., McMahon, R. J., Ediger, M. D. & Mates, T. E. Transformation of stable glasses into supercooled liquids: growth fronts and anomalously fast liquid diffusion. *J. Phys. Chem. B* **114,** 2635–43 (2010).

80. Dalal, S. S. & Ediger, M. D. Influence of substrate temperature on the transformation front velocities that determine thermal stability of vapor-deposited glasses. *J. Phys. Chem. B* **119,** 3875–82 (2015).

81. Wolynes, P. G. Spatiotemporal structures in aging and rejuvenating glasses. *Proc. Natl. Acad. Sci. U. S. A.* **106,** 1353–8 (2009).

82. Léonard, S. & Harrowell, P. Macroscopic facilitation of glassy relaxation kinetics: ultrastable glass films with frontlike thermal response. *J. Chem. Phys.* **133,** 244502 (2010).

83. Wisitsorasak, A. & Wolynes, P. P. G. Fluctuating Mobility Generation and Transport in Glasses. *Phys. Rev. E* **88,** 3–6 (2013).

84. Hocky, G. M., Berthier, L. & Reichman, D. R. Equilibrium ultrastable glasses produced by random pinning. *J. Chem. Phys.* **141,** 224503 (2014).

85. MOYNIHAN, C. T., EASTEAL, A. J., BOLT, M. A. & TUCKER, J. Dependence of the Fictive Temperature of Glass on Cooling Rate. *J. Am. Ceram. Soc.* **59,** 12–16 (1976).

86. Gao, S. & Simon, S. L. Measurement of the limiting fictive temperature over five decades of cooling and heating rates. *Thermochim. Acta* **603,** 123–127 (2015).

87. Wojnarowska, Z. *et al.* Broadband dielectric relaxation study at ambient and elevated pressure of molecular dynamics of pharmaceutical: indomethacin. *J. Phys. Chem. B* **113,** 12536–45 (2009).

88. Haji-Akbari, A. & Debenedetti, P. G. The Effect of Substrate on Thermodynamic and

Kinetic Anisotropies in Atomic Thin Films. *J. Chem. Phys.* **141,** 17 (2014).

89. Stevenson, J. D. & Wolynes, P. G. On the surface of glasses. *J. Chem. Phys.* **129,** 234514 (2008).

90. Ritland, H. N. Limitations of the Fictive Temperature Concept. *J. Am. Ceram. Soc.* **39,** 403–406 (1956).

91. Adam, G. & Gibbs, J. H. On the Temperature Dependence of Cooperative Relaxation Properties in Glass-Forming Liquids. *J. Chem. Phys.* **43,** 139 (1965).

92. Lopeandía, A. F., Rodríguez-Viejo, J., Chacón, M., Clavaguera-Mora, M. T. & Muñoz, F. J. Heat transfer in symmetric U-shaped microreactors for thin film calorimetry. *J. Micromechanics Microengineering* **16,** 965–971 (2006).

93. Richert, R., Lunkenheimer, P., Kastner, S. & Loidl, A. On the derivation of equilibrium relaxation times from aging experiments. *J. Phys. Chem. B* **117,** 12689–94 (2013).

94. Dyre, J. C. Hidden scale invariance in condensed matter. *J. Phys. Chem. B* **118,** 10007–24 (2014).

95. Casalini, R., Mohanty, U. & Roland, C. M. Thermodynamic interpretation of the scaling of the dynamics of supercooled liquids. *J. Chem. Phys.* **125,** 014505 (2006).

96. Roland, C. M., Feldman, J. L. & Casalini, R. Scaling of the local dynamics and the intermolecular potential. *J. Non. Cryst. Solids* **352,** 4895–4899 (2006).

97. Johari, G. P. Comment on 'glass transition in pure and doped amorphous solid water: an ultrafast microcalorimetry study'. *J. Chem. Phys.* **127,** 157101 (2007).

98. Busch, R., Bakke, E. & Johnson, W. L. Viscosity of the supercooled liquid and relaxation at the glass transition of the Zr46.75Ti8.25Cu7.5Ni10Be27.5 bulk metallic glass forming alloy. *Acta Mater.* **46,** 4725–4732 (1998).

99. Tylinski, M. *et al.* Vapor-deposited glasses of methyl-m-toluate: How uniform is stable glass transformation? *J. Chem. Phys.* **143,** 244509 (2015).

100. Wang, J. Q., Shen, Y., Perepezko, J. H. & Ediger, M. D. Increasing the kinetic stability of bulk metallic glasses. *Acta Mater.* **104,** 25–32 (2016).

101. Hatase, M., Hanaya, M., Hikima, T. & Oguni, M. Discovery of homogeneous-nucleation-based crystallization in simple glass-forming liquid of toluene below its glass-transition temperature. *J. Non. Cryst. Solids* **307-310,** 257–263 (2002).

102. Kudlik, A., Tschirwitz, C., Benkhof, S., Blochowicz, T. & Rössler, E. Slow secondary relaxation process in supercooled liquids. *Europhys. Lett.* **40,** 649–654 (1997).

103. Martinez, L. M. & Angell, C. A. A thermodynamic connection to the fragility of glass-forming liquids. *Nature* **410,** 663–7 (2001).

104. Scopigno, T., Ruocco, G., Sette, F. & Monaco, G. Is the fragility of a liquid embedded in the properties of its glass? *Science* **302,** 849–52 (2003).

105. Martinez-Garcia, J. C., Rzoska, S. J., Drozd-Rzoska, A. & Martinez-Garcia, J. A universal description of ultraslow glass dynamics. *Nat. Commun.* **4,** 1823 (2013).

106. Roland, C. M. Characteristic relaxation times and their invariance to thermodynamic conditions. *Soft Matter* **4,** 2316 (2008).

107. Crowley, K. J. & Zografi, G. The use of thermal methods for predicting glass-former fragility. *Thermochim. Acta* **380,** 79–93 (2001).

108. Roland, C. M., Hensel-Bielowka, S., Paluch, M. & Casalini, R. Supercooled dynamics of glass-forming liquids and polymers under hydrostatic pressure. *Reports Prog. Phys.* **68,** 1405–1478 (2005).

109. Yoshioka, M., Hancock, B. C. & Zografi, G. Crystallization of indomethacin from the amorphous state below and above its glass transition temperature. *J. Pharm. Sci.* **83,** 1700–1705 (1994).

110. Dawson, K. J., Kearns, K. L., Ediger, M. D., Sacchetti, M. J. & Zografi, G. D. Highly stable indomethacin glasses resist uptake of water vapor. *J. Phys. Chem. B* **113,** 2422–7 (2009).

111. Zhao, J., Simon, S. L. & McKenna, G. B. Using 20-million-year-old amber to test the super-Arrhenius behaviour of glass-forming systems. *Nat. Commun.* **4,** 1783 (2013).

112. Paluch, M. *et al.* General rules prospected for the liquid fragility in various material groups and different thermodynamic conditions. *J. Chem. Phys.* **141,** 134507 (2014).

113. Zhang, S. H., Casalini, R., Runt, J. & Roland, C. M. Pressure Effects on the Segmental Dynamics of Hydrogen-Bonded Polymer Blends. *Macromolecules* **36,** 9917–9923 (2003).

114. Pawlus, S., Paluch, M., Ziolo, J. & Roland, C. M. On the pressure dependence of the fragility of glycerol. *J. Phys. Condens. Matter* **21,** 332101 (2009).

115. Koperwas, K., Grzybowski, A., Tripathy, S. N., Masiewicz, E. & Paluch, M. Thermodynamic consequences of the kinetic nature of the glass transition. *Sci. Rep.* **5,** 17782 (2015).

116. Andersson, S. P. & Andersson, O. Relaxation Studies of Poly(propylene glycol) under High Pressure. *Macromolecules* **31,** 2999–3006 (1998).

117. Davies, R. O. & Jones, G. O. Thermodynamic and kinetic properties of glasses. *Adv. Phys.* **2,** 370–410 (1953).

118. Atake, T. & Angell, C. A. Pressure dependence of the glass transition temperature in molecular liquids and plastic crystals. *J. Phys. Chem.* **83,** 3218–3223 (1979).

119. DiMarzio, E. A., Gibbs, J. H., Fleming, P. D. & Sanchez, I. C. Effects of Pressure on the Equilibrium Properties of Glass-Forming Polymers. *Macromolecules* **9,** 763–771 (1976).

120. Andronis, V., Yoshioka, M. & Zografi, G. Effects of sorbed water on the crystallization of indomethacin from the amorphous state. *J. Pharm. Sci.* **86,** 346–51 (1997).

121. Murnaghan, F. D. The Compressibility of Media under Extreme Pressures. *Proc. Natl. Acad. Sci.* **30,** 244–247 (1944).

122. Anderson, D. L. Theory of the Earth. (1989). at <http://authors.library.caltech.edu/25018/18/TOE17.pdf>

123. Simonelli, A. P., Mehta, S. C. & Higuchi, W. I. Dissolution Rates of High Energy Sulfathiazole-Povidone Coprecipitates II: Characterization of Form of Drug Controlling Its Dissolution Rate via Solubility Studies. *J. Pharm. Sci.* **65,** 355–361 (1976).

124. Grzybowska, K. *et al.* Enhancement of amorphous celecoxib stability by mixing it with octaacetylmaltose: the molecular dynamics study. *Mol. Pharm.* **9,** 894–904 (2012).

125. Lu, G. W., Hawley, M., Smith, M., Geiger, B. M. & Pfund, W. Characterization of a novel polymorphic form of celecoxib. *J. Pharm. Sci.* **95,** 305–17 (2006).

126. Makower, B. & Dye, W. B. Sugar Crystallization, Equilibrium Moisture Content and Crystallization of Amorphous Sucrose and Glucose. *J. Agric. Food Chem.* **4,** 72–77 (1956).

127. IMAIZUMI, H., NAMBU, N. & NAGAI, T. Stability and several physical properties of amorphous and crystalline forms of indomethacin. *Chem. Pharm. Bull. (Tokyo).* **28,** 2565–2569 (1980).

128. Andronis, V. & Zografi, G. The molecular mobility of supercooled amorphous indomethacin as a function of temperature and relative humidity. *Pharm. Res.* **15,** 835–42 (1998).

129. Xu, Q., Tanaka, Y. & Czernuszka, J. T. Encapsulation and release of a hydrophobic drug from hydroxyapatite coated liposomes. *Biomaterials* **28,** 2687–94 (2007).

130. Liu, Y. H., Fujita, T., Aji, D. P. B., Matsuura, M. & Chen, M. W. Structural origins of Johari-Goldstein relaxation in a metallic glass. *Nat. …* **5,** 3238 (2014).

131. Wang, L. L.-M., Velikov, V. & Angell, C. a. C. Direct determination of kinetic fragility indices of glassforming liquids by differential scanning calorimetry: Kinetic versus thermodynamic fragilities. *J. Chem. Phys.* **117,** 10184 (2002).

132. Kaushal, A. & Bansal, A. Thermodynamic behavior of glassy state of structurally related compounds. *Eur. J. Pharm. …* **69,** 1067–76 (2008).

133. Yokoyama, D., Sakaguchi, A., Suzuki, M. & Adachi, C. Horizontal molecular orientation in vacuum-deposited organic amorphous films of hole and electron transport materials. *Appl. Phys. …* **93,** 173302 (2008).

134. Whitaker, K. R., Tylinski, M., Ahrenberg, M., Schick, C. & Ediger, M. D. Kinetic stability and heat capacity of vapor-deposited glasses of o-terphenyl. *J. Chem. Phys.* **143,** 084511 (2015).

135. Sepúlveda, A., Leon-Gutierrez, E., Gonzalez-Silveira, M., Clavaguera-Mora, M. T. & Rodríguez-Viejo, J. Anomalous Transformation of Vapor-Deposited Highly Stable Glasses of Toluene into Mixed Glassy States by Annealing Above Tg. *J. Phys. Chem. Lett.* **3,** 919–23 (2012).

136. Sepúlveda, A., Tylinski, M., Guiseppi-Elie, A., Richert, R. & Ediger, M. D. Role of fragility in the formation of highly stable organic glasses. *Phys. Rev. Lett.* **113,** 045901 (2014).

137. Sun, Y., Zhu, L., Kearns, K. L., Ediger, M. D. & Yu, L. Glasses crystallize rapidly at free surfaces by growing crystals upward. *Proc. Natl. Acad. Sci. U. S. A.* **108,** 5990–5 (2011).

138. Sun, Y. *et al.* Stability of amorphous pharmaceutical solids: crystal growth mechanisms and effect of polymer additives. *AAPS J.* **14,** 380–8 (2012).

139. Taylor, L. S. & Zografi, G. Spectroscopic Characterization of Interactions Between PVP and Indomethacin in Amorphous Molecular Dispersions. *Pharm. Res.* **14,** 1691–1698